Hydrodynamic interaction between cylinders at moderate Reynolds numbers

by

ANUPAM BISWAS

B.Tech Indian Institute of Technology Kharagpur, INDIA, 2009

A THESIS SUBMITTED IN PARTIAL FULFILLMENT OF THE REQUIREMENTS FOR THE DEGREE OF

MASTER OF APPLIED SCIENCE

in

THE FACULTY OF GRADUATE STUDIES

(Mechanical Engineering)

THE UNIVERSITY OF BRITISH COLUMBIA
(Vancouver)

July, 2013

Abstract

The hydrodynamic interaction between two cylinders perpendicular to the freestream, in a tandem arrangement[1] was studied for moderate Reynolds numbers ($1 \leq Re \leq 40$). The influence of multiple geometric variables was considered: separation distances between the cylinders, ellipticity of the cylinders, the cylinder aspect ratio, and the angular inclination between the cylinders.

In the first part of this study, a numerical investigation of the two-dimensional steady flow past cylinders was carried out. The characteristic length, D, in all simulations was taken to be twice the major axis of the cylinder cross-section, (i.e. equal to the diameter for cylinders of circular cross-section). The two-dimensional flow was studied for separations up to $50D$. Four different ellipticities were studied. The drags experienced by front and rear cylinders were compared with that experienced by a single cylinder of the same cross-section.

The second part of the study consisted of the steady three-dimensional flow analysis for parallel cylinders in tandem for separations ranging from $2D$ to $20D$ and cylinder lengths up to $20D$.

In the third part of this thesis, a steady flow analysis was done for two circular cylinders in tandem with lengths equal to $5D$ but with the cylinder axes in different orientations relative to the plane normal to the flow. This angular separation between the cylinders produces a hydrodynamic moment, which is dependent on the geometry and the flow Reynolds number.

The fourth and final part of this work is the study of the unsteady three-dimensional flow that would result from the hydrodynamic moment discussed in relation to the third part of the thesis.

The thesis closes with some remarks on the implications of these findings to papermaking and recommendations for future work.

[1] For the purposes of this thesis, two cylinders are defined to be in tandem if the vector joining the centroids of the cylinders is co-linear with the freestream velocity vector.

Preface

The authors of chapter 2 are Anupam Biswas and Sheldon Green. Dr. Green identified the need to understand the effect of separation between fibers and cross-sectional deformations on hydrodynamic interaction between fibers, in moderate Reynolds number flows. I, after preliminary simulations to determine the domain size, carried out numerical simulations of flows over two cylinders in tandem arrangements, in Ansys Fluent software. Subsequent to the two-dimensional study, Dr. Green identified the need for understanding the effect of finite fiber-lengths. So in addition to other geometrical parameters, I carried out numerical simulations for different values of the ratio of fiber-length to fiber-diameter. I wrote the manuscript with revisions and suggestions from Dr. Green.

The authors of chapter 3 are Anupam Biswas and Sheldon Green. Dr. Green identified the need to understand the rotational torques that fibers may experience at close distances due to non-parallel alignments. I carried out numerical simulations for a range of all possible alignments between two cylinders in a tandem arrangement. I prepared the manuscript with revisions and suggestions from Dr. Green.

The authors of chapter 4 are Anupam Biswas and Sheldon Green. Dr. Green identified the need to verify the results obtained in chapter 3 by an unsteady flow study. I carried out simulations of flows at extreme ends of the moderate Reynolds number regime. I also carried out post-processing of the data to study the transient effects of low and high initial angular differences between front and rear cylinders. As the previous chapters, I prepared the manuscript with revisions and suggestions from Dr. Green.

Table of Contents

List of Tables

List of Figures

List of Symbols

D Cylinder diameter [m]

L Cylinder length [m]

S Separation distance between front and rear cylinders [m]

a Major axis length of cylinder cross-section [m]

b Minor axis length of cylinder cross-section [m]

Re Reynolds number based on cylinder diameter, $Re = \rho UD/\mu$

AR Aspect ratio, $AR = L/D$

SeR Separation ratio, $SeR = S/D$

E Ellipticity, $E = 1 - b/a$

ρ Fluid density [$kg.m^{-3}$]

μ Fluid dynamic viscosity [Pa.s]

U Inlet velocity [$m.s^{-1}$]

W_y Width in y-direction [m]

W_z Width in z-direction [m]

L_u Upstream length [m]

L_d Downstream length [m]

Θ_z Angle made with positive direction of x-axis, seen from positive z-axis [degree]

Θ_{xf} Angle made with positive direction of y-axis, seen from positive x-axis for front cylinder [degree]

Θ_{xr} Angle made with positive direction of y-axis, seen from positive x-axis for rear cylinder [degree]

Θ_d Angular difference for front and rear cylinders, seen from positive x-axis, $\Theta_d = \Theta_{xf} - \Theta_{xr}$ [degree]

C_D Drag coefficient, C_D = Drag force/($0.5\rho U^2D$) in two-dimensions

C_M Moment coefficient, C_M = Moment/($0.5\rho U^2LD^2$)

τ Moment [N.m]

I Moment of inertia [$N.m^2$]

Glossary

Separation ratio – This is defined as the distance between centres of two cylinders in tandem arrangement divided by twice the major axis of elliptical cross-section of cylinder.

Aspect ratio – This is defined as the length of cylinder divided by twice the major axis of elliptical cross-section of cylinder.

Ellipticity – This is a measure of the compression from a circle to an ellipse and is defined as the ratio of minor axis to major axis subtracted from unity.

Angular separation – This is defined as the projected angle between axes of two cylinders in tandem arrangement when seen from the downstream direction, measured from front to rear cylinder.

Tandem arrangement – It is defined to be an arrangement in the vector joining the centroids of the cylinders is co-linear with the freestream velocity vector.

Front cylinder – It is defined as the cylinder which is relatively positioned in the upstream direction.

Rear cylinder – It is defined as the cylinder which is relatively positioned in the downstream direction.

Acknowledgements

I extend my sincere gratitude to my supervisor Dr. Sheldon Green who provided continuous guidance during my research. I thank him for providing critical insight into the research problems and for allowing me the choice of methodology and mode of investigation. I thank him for all the support throughout this project. In its entirety, it was for me a highly valuable academic experience working with him.

I sincerely thank Ali Vakil for his indispensable support, suggestions and discussions during the project.

I would like to thank Arash Olyaei, Fatih Damat and Pouyan Jahangiri for their huge support, mentorship and the much needed academic discourses during the project.

I would like to thank George Soong for his continuous assistance in labs and office and other members of Pulp and Paper Centre for all the social and recreational activities that helped to maintain a positive and rejuvenating atmosphere.

I would like to thank the Natural Science and Engineering Research Council of Canada (NSERC) and AstenJohnson Inc. for their financial support of this project.

Finally, I would like to thank all the members of my research group for their continued comments and suggestions and their friendship throughout the project.

Chapter 1 – Introduction

Studies of fluid flow over different geometries of practical concern have long been of interest. In many applications like papermaking, it is of interest to understand the motion of fibers in the flow. For example, the properties and microstructure of fiber-reinforced composites is highly dependent on orientation and entanglement of fibers, which are controlled by the flow in conventional flow molding techniques [1]. Yamamoto et al [1] also suggest that fiber motions in pulp suspensions are intricate depending on parameters like fiber-length, aspect ratio, fiber stiffness and volume fraction. In pulp suspensions, usually the density of these fibers is not very different from that of water but they may be present in different lengths and diameters. In addition to that, the fibers being hollow are collapsible and flexible. These factors make the detailed numerical and theoretical analyses of fiber motions intricate. Also, as the fibers are flexible, as the concentration of fibers is increased, it shows an increase in fiber-fiber entanglement and flocculation which is undesirable in the paper-manufacturing process. Extra effort is applied in order to deflocculate the fibers.

Theories derived for Stokes flows have been extensively used to validate later analyses to understand fiber motions in suspensions [2] [3]. There have been several approaches to understand the nature of particle dynamics in pulp suspensions. Stockie and Green [4] have suggested an application of immersed boundary method to compute hydrodynamic coupling between flexible fiber and incompressible fluid. They showed a difference in the angles of fibre alignment and shear direction in a horizontal shear flow. Zhu and Peskin also used immersed boundary method to compute drag forces experienced by flexible fiber in two-dimensional viscous flow [5]. Lattice Boltzmann methods (LBM) have also been employed in order to delve deeper into the physics of hydrodynamic interactions involved in fiber suspensions. By using a ball-and-socket fibre model with a chain of contacting cylindrical segments, Qi [6] demonstrated the motion of flexible fibers for low particle Reynolds numbers. Viscoelastic fiber models have also been suggested [7] [8].

An understanding of fiber-fiber interaction before deposition on the forming fabric is of importance in order to have a deeper insight into the paper-forming process. Before deposition, the speed of water may be of the order of 0.5 m/s. The differential velocity between a fiber and the surrounding water may be much lower, as fiber Stokes numbers are, in many parts of a papermachine, quite low. As water density and dynamic viscosity are 1000 kg/m^3 and 0.001 Pa.s respectively, and a typical fiber diameter may be 20 μm, the Reynolds number based on fiber diameter is about 10.

There exists a huge body of work about flow around circular cylinders. Zdravkovich [9] provides a thorough review and detailed information on different flow phenomena associated with flow around cylinders. A linear relation is found to exist between the wake-length and Reynolds number in the range $4.4<Re<40$ ($L_w/D = 0.05Re$). It also talks about the widening of the streamlines and reaching a maximum at a distance from the cylinder centre. With rising *Re*, the maximum widening decreases and the location of this gets further away from the cylinder centre.

Extensive numerical, theoretical and experimental studies have been carried out for flow around cylinders and ellipses. Fornberg [10] obtained numerical solutions for flows around circular cylinders up to $Re = 300$. Numerical studies involving the effects of blockage were also studied by Sen *et al.* [11]. Flows around elliptical cross-sections have also received special interest as due to two axes of symmetry, ellipses may be set an angle to the free stream. Numerical investigation of moderate Reynolds number ($6<Re<40$) flow around ellipses for different orientations has been carried out by Dennis and Young [12]. Unsteady simulations in the range $30<\mathrm{Re}<200$ have been carried out by varying the ratio of minor axis to major axis and the vortex shedding phenomenon has been studied in detail [13]. Stokes flow analysis has also been carried out for an ellipse in a channel flow [14]. Imai [15] has shown a general method to solve Oseen's equations for low *Re* flow around elliptical geometries and computed lift and drag coefficients for different angles to free stream. Tomotika and Aoi [16] have carried out theoretical analyses to formulate drag forces acting on a cylinder in flows with $Re<4$. A flat plate and a circle are special cases of an ellipse, depending on the ratio of minor axis to major axis. Tomotika and Aoi [17] carried out theoretical analyses to determine the drag coefficients for these shapes. Experimental studies were carried out to visualize flow around cylinders for $0.1<Re<2000$ [18]. Flow visualization studies for different geometrical configurations, including spheres and cylinders in tandem and side-by-side arrangement were carried out [19]. Khayat and Cox [20] obtained expressions for lift, drag and moment forces acting on a long slender body in a uniform flow, with an analytical approach.

Flow around two bluff bodies may be much different from that around isolated bodies. For example, if one body is in tandem arrangement with another, then the one which is shielded may, at some situations, experience negative drag and may experience greater drag than the unshielded cylinder at very high Reynolds numbers [21]. In the moderate Reynolds number range ($1<Re<40$), when two cylinders are in side-by-side arrangement, asymmetric streamlines are present around the cylinders with drag coefficient being much smaller than an isolated cylinder and lift coefficient having a sigmoidal behavior with separation between the cylinders, as shown by Vakil and Green

[22]. Experimental work for flows at as high as Re = 2.5 × 10^4 have been carried for cylinders in side-by-side arrangement [23]. Lee and Wang [24] carried out numerical studies (Re<160) for two cylinders in a flow mainly to study the vortex shedding phenomena, with line connecting the cylinders being of different lengths and at different angles to free stream. Numerical studies to determine the flow behavior for cylinders in tandem and side-by-side arrangements, especially phenomena related to shedding of vortices in 100<Re<200 were carried out by Meneghini *et al.* [25]. Numerical simulations to study the interaction between two spherical bubbles was also carried out for Re<200 which showed some difference in experimental and numerical results [26]. Zdravkovich and Pridden [27] have carried out wake interference studies for cylinders in side-by-side and tandem arrangements and have defined the term, interference drag coefficient, which is the difference between the drag force experienced in the vicinity of another cylinder and the isolated cylinder. They state that interference drag coefficient for the upstream cylinder is almost zero at zero separation between the cyliners, reaches a minimum at some distance and then again goes to zero for separations greater than 3.5D.

Numerical and experimental studies for flows through an array of ellipses have also been carried out [28] [29].

In flow casting applications, fiber rotations are of great interest. Vakil and Green carried out a numerical investigation to determine the hydrodynamics moments acting on a cylinder of finite length with its axis at different angles with respect to the free stream [30].

In this work, steady state solutions were obtained for moderate Re(1<Re<40) two-dimensional flow over cylinders with ellipticities 0, 0.3, 0.5 and 0.7 and separation ratios ranging from 1D- 50D. This was followed by a three-dimensional moderate Re flow analysis over parallel cylinders in a tandem arrangement with separations up to 20D and fiber-lengths from 2D to 20D. This study was carried out only for ellipticities 0 and 0.7. Subsequent to the study of parallel cylinders, some simulations were carried out for cylinders (with L = 5D) in a tandem arrangement with different angular orientations of their axes in respective planes normal to freestream vector. This was done in order to determine the hydrodynamics torques produced due to different orientations of cylinders in proximity. The study was carried out for separations of 2D, 3D and 5D. The final part of the work consists of unsteady flow analysis for two cases. The first case is a study of rotation of a cylinder (with L = 5D) which has its axis initially inclined at 45 degrees to the freestream vector. The second case involves two cylinders (L = 5D) in a tandem arrangement (separation of 2D), with initial angles

of separation of 5 and 85 degrees. The unsteady flow simulations were carried out at Re = 1 and Re = 40.

Chapter 2 – Hydrodynamic interaction of parallel cylinders in tandem arrangement

2.1 Introduction

A study of two-dimensional flow over the cylinders was carried out as they always serve as a benchmark for comparison with the more realistic case of three dimensional cylinders. Also, since increasing the length has an asymptotic variation of drag and lift coefficients, the results obtained from two-dimensional studies, in some cases, may be used for very long cylinders without having to simulate the flow for these very long fibers.

2.2 Geometry and meshing

For 2D flows, the geometrical parameters are the separation ratio (s/D), ellipticity (1 - b/a) and in the case of 3D flows, aspect ratio (L/D) is an additional parameter. In some of the 3D simulations, the angular position of cylinder with respect to the direction of flow (Θ_z) and difference in angular position for two cylinders in a plane normal to flow direction are other geometrical parameters.

Figure 1 shows a schematic diagram for the flow domain. It, besides giving information about the geometry of flow domain and the objects of interest, also shows the boundary conditions at different surfaces. The left and right vertical boundaries have velocity-inlet and pressure-outlet boundary conditions. It is important at this point to mention that these simulation studies were of external flows and it was only the region about the cylinders which were of interest. Hence the top and bottom boundaries, not being bounding solid walls, had to be placed at distances that did not lead to inaccuracies in solution and secondly, did not make the flow domain large enough to increase the computation time drastically. The latter constraint is less serious for 2D flows and hence the total width (W_y) was kept 500D. The upstream length (L_u) was 250D and the downstream length (L_d) was 500D.

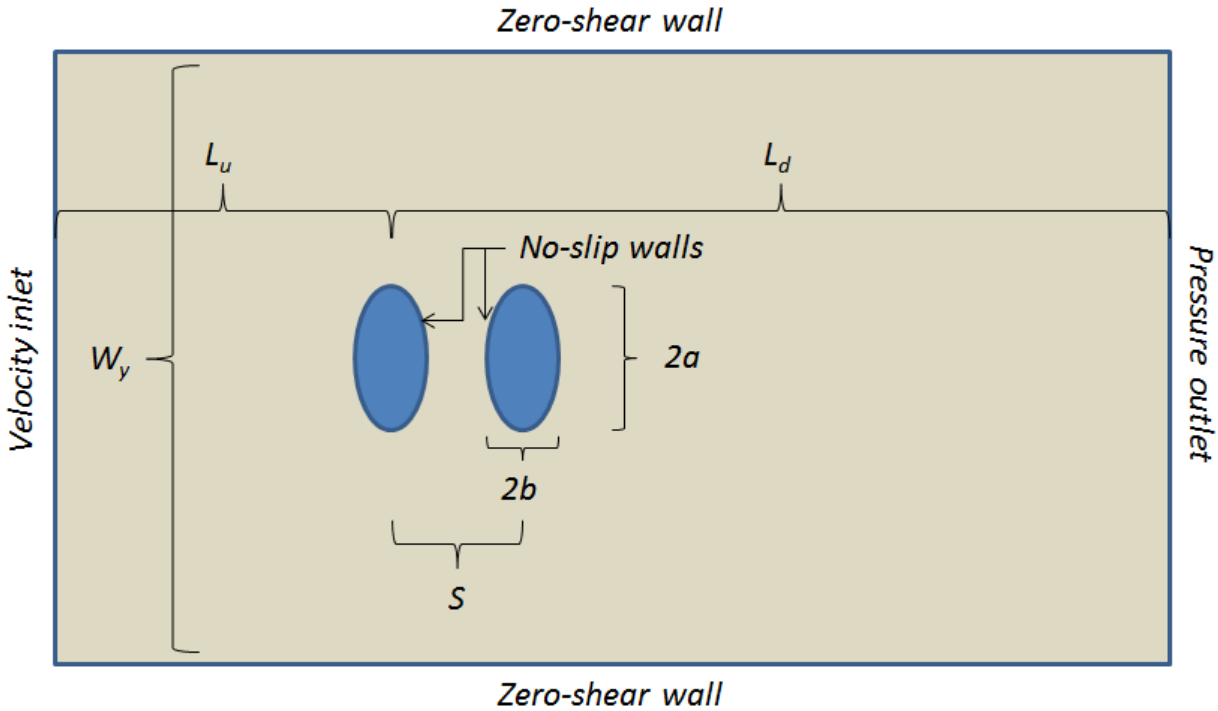

Figure 1: Schematic diagram of flow domain with geometrical details

The geometries for all cases were prepared using GAMBIT. Figure 2 shows the meshed flow domain. The flow domain has mixed meshing and Figure 3 shows a small rectangular region containing the cylinders has unstructured meshing and all the other regions have structured meshing. A detailed view near the cylinders is shown in Figure 4. Boundary layer meshing was done around the cylinder surfaces.

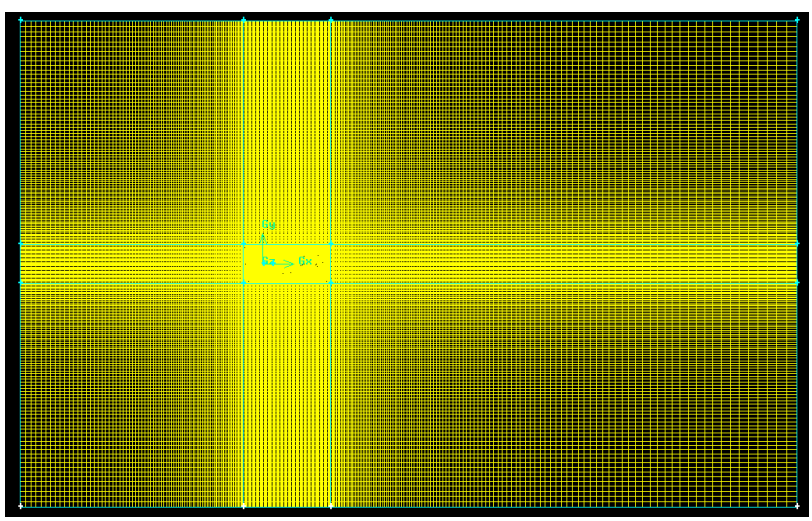

Figure 2: Mesh of the entire flow domain

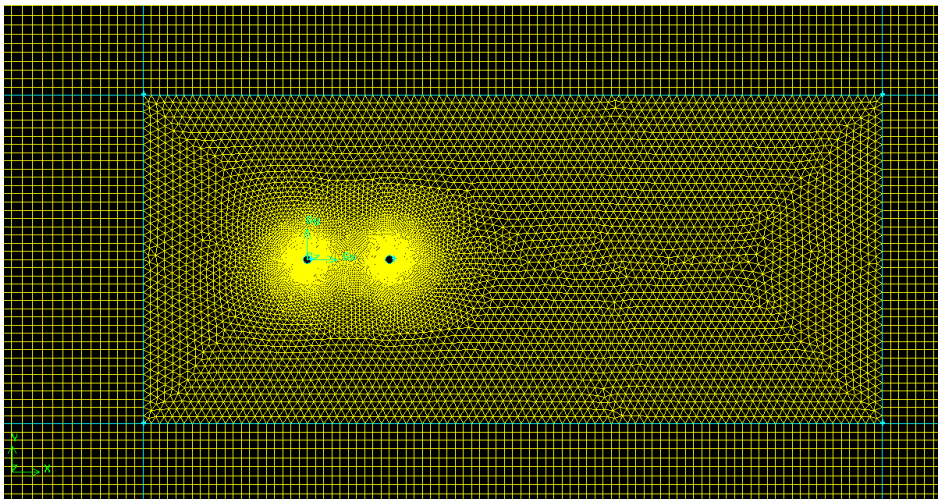

Figure 3: Close view of mesh showing unstructured and structured mesh regions

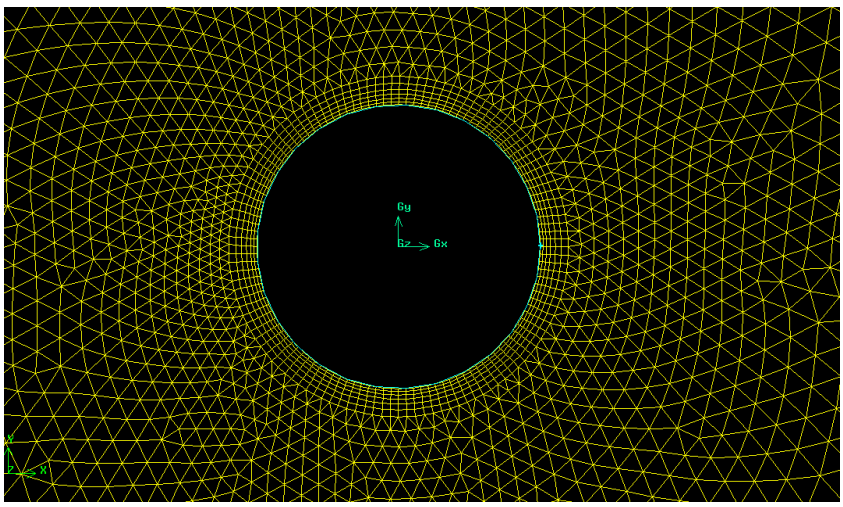

Figure 4: Boundary layer mesh around the cylinder

The flow domain geometry for 3D steady flows, in which the cylinders are always parallel to each other and only vary in separation between their centroids (S) in the x-direction, has been shown in Figure 5. In this geometry, L_u was 200D, L_d was 310D, W_y was 240D and W_z was 50D. The geometry was partitioned in 9 different regions in order to carry out a mixed meshing. A close view of the central region as shown in Figure 6 shows the cylinders in tandem arrangement. Similar to the 2D case, the central region in the 3D geometry, which consists of the cylinders, has unstructured meshing whereas the surrounding 8 regions have structured meshing.

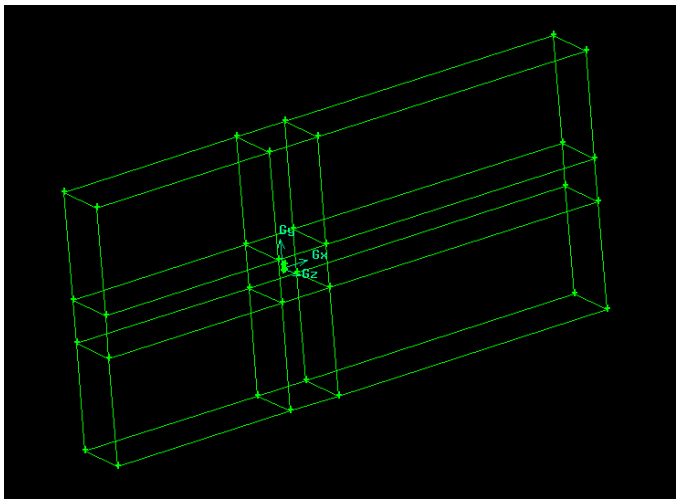

Figure 5: Domain partition for meshing of 3D flow region with parallel cylinders

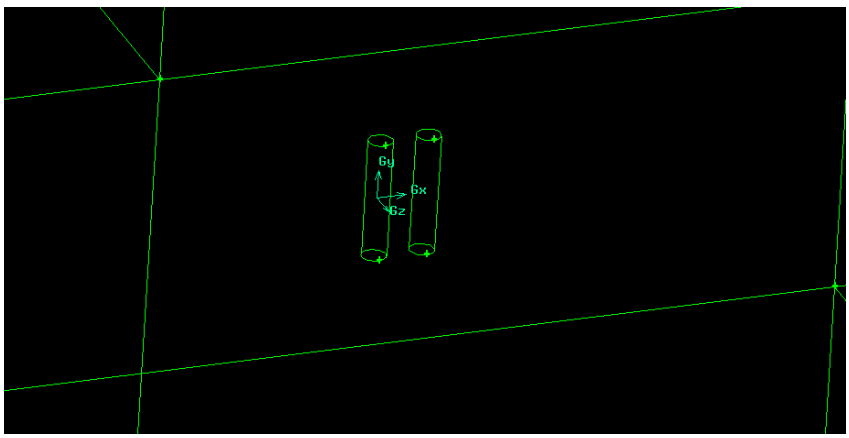

Figure 6: A close view of the two parallel cylinders in the central block of the partitioned region

2.3 Domain-size and mesh independence

For the two-dimensional flow simulations, the domain size was kept the same as in [22]. At blockage ratio D/W = 0.01, the effect of lateral boundaries on characteristic flow parameters may be said to be insignificant [11]. $W = 200D$, $L_u = 50D$ and $L_d = 100D$ were used in [11]. In this work $W = 500D$ (blockage ratio of 0.002), $L_u = 250D$ and $L_d = 500D$. After the simulations, the domain-size dependence was re-verified by plotting pressure and velocity magnitude in x, y and z-directions through the origin. Figure 7 and Figure 8 show that the domain size chosen is large enough as spatial variation is zero at the extremes. Spatial distance, pressure and velocity have been made non-dimensional by divisions by cylinder diameter D, ρU^2 and U respectively.

A number of simulations were also done with smaller domain-sizes and the result has been tabulated below. A maximum error of around 9% was noticed when the domain-size was $W = 50D$, $L_d = 250D$ and $L_u = 125D$. All these simulations were carried out for convergence tolerance of 1.0e-9.

Case	W/D	L_d/D	L_u/D	C_d (front)	C_d (rear)	% error C_d (front)	%error C_d (rear)
1	250	250	125	7.1561	4.066079	0.945693	0.940608
2	150	250	125	7.228703	4.10206	1.96985	1.833831
3	50	250	125	7.718279	4.365205	8.875935	8.36643
4	250	150	125	7.155144	4.065487	0.932218	0.925903
5	250	100	125	7.153336	4.064361	0.906708	0.897971
6	250	250	75	7.219471	4.094626	1.839625	1.649279
7	250	250	50	7.318497	4.1397	3.236505	2.768247
8	500	500	250	7.089059	4.028189	0	0

Table 1 : Domain size test for two-dimensional flows

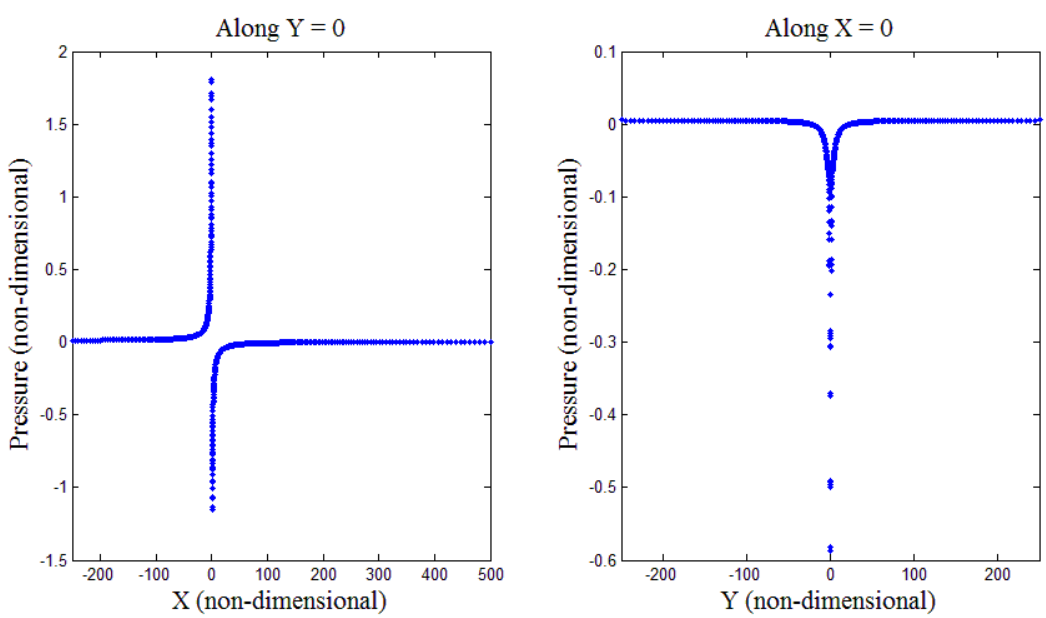

Figure 7: Pressure distribution in X and Y directions (two-dimensional flow)

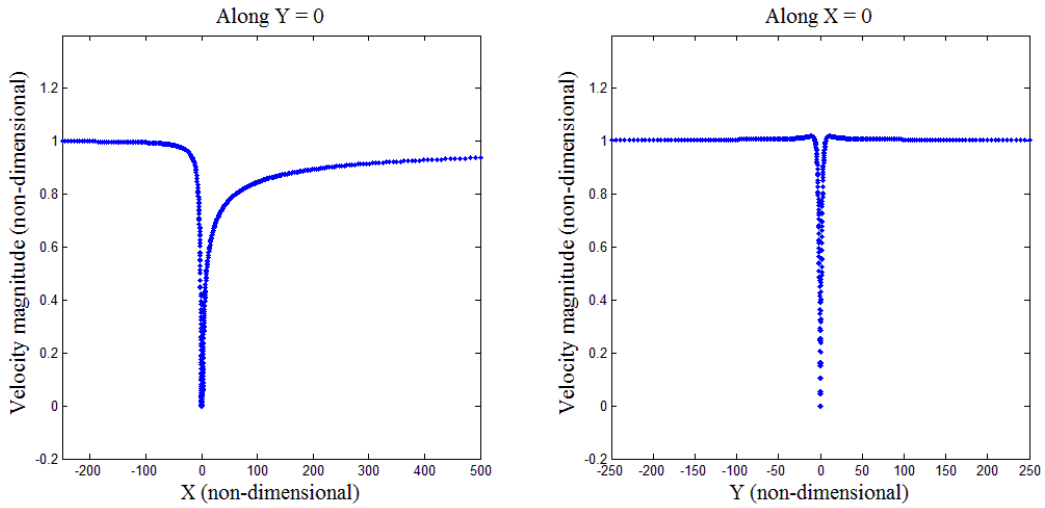

Figure 8: Velocity magnitude distribution along X and Y directions (two-dimensional flow)

A few simulations were carried out with the chosen domain size but with varying mesh elemnt sizes. The case of *Re* = 1, *SeR* = 1 and *E* = 0.7 was chosen as the test case. Figure 9 below shows the result for the mesh independence test. It was seen that increasing the mesh element size from around 29200 to 228000 resulted in 1.87% and 0.12% difference in drag coefficients of front and rear cylinders respectively. Hence a mesh element size of around 78500 was chosen for all other simulations.

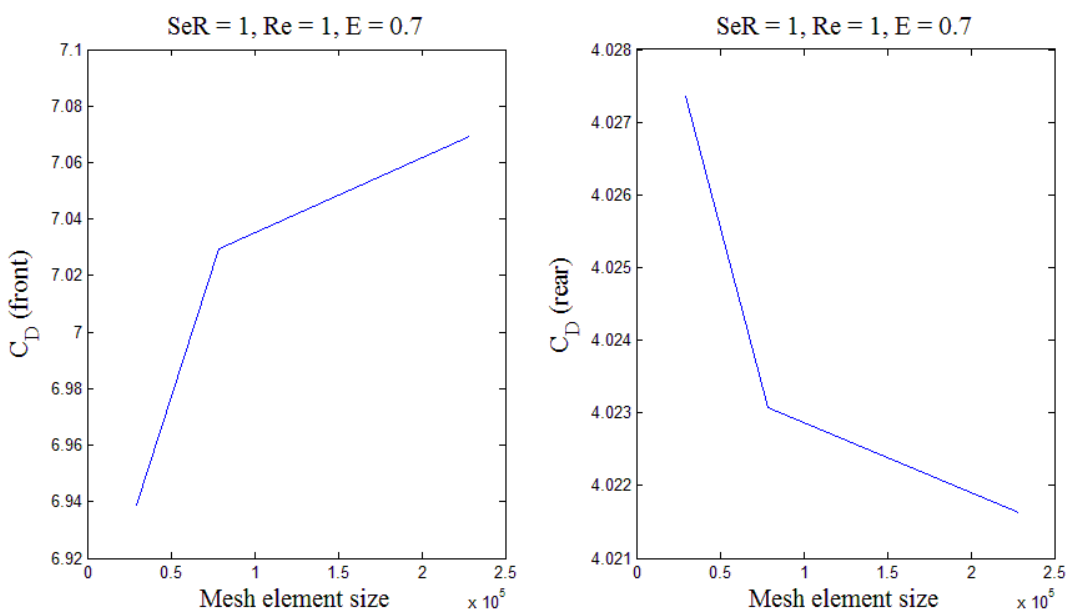

Figure 9: Mesh independence test for two-dimensional flows

As three-dimensional simulations take much more time than two-dimensional ones, it was required to reduce the size of the domain to reduce computational time without leading to substantial inaccuracies in the solution. As the cylinder axes were in the Y-direction, the shortening of the domain was applied in the Z-direction. In [30], the upstream length L_u was $10L$ and downstream length L_d was $15L$, the width W was $12L$ and depth was $50D$. In this work, the diameter was kept the same in all cases but the length was changed according the aspect ratio. If the same pattern as in [30] was to be followed, the largest domain would be for the one with the greatest aspect ratio, that is, 20. This mesh was prepared and used for all cases. The solutions were checked and Figure 10 and Figure 11 show that the spatial variation of pressure and velocity-magnitude near the domain-extremes are very close to zero.

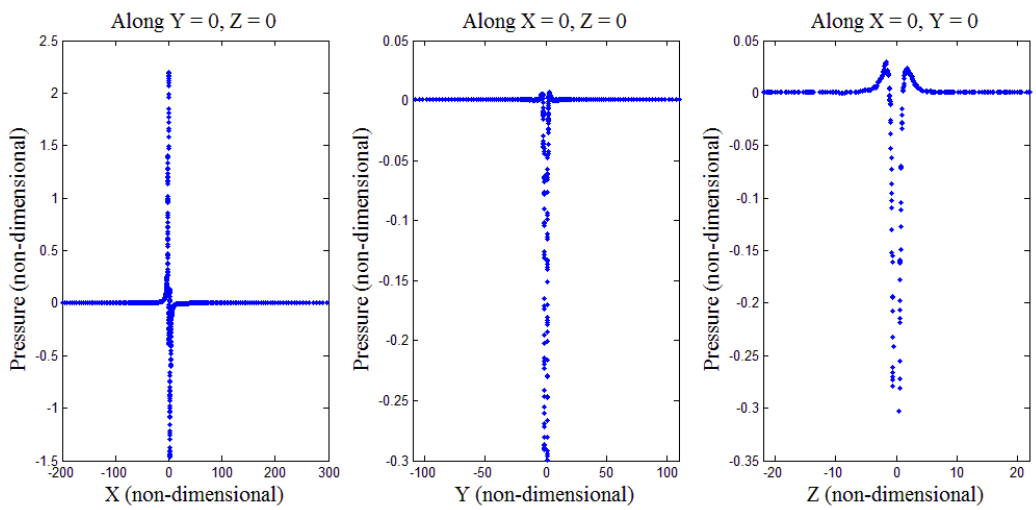

Figure 10: Pressure distribution in X, Y and Z directions (three-dimensional flow)

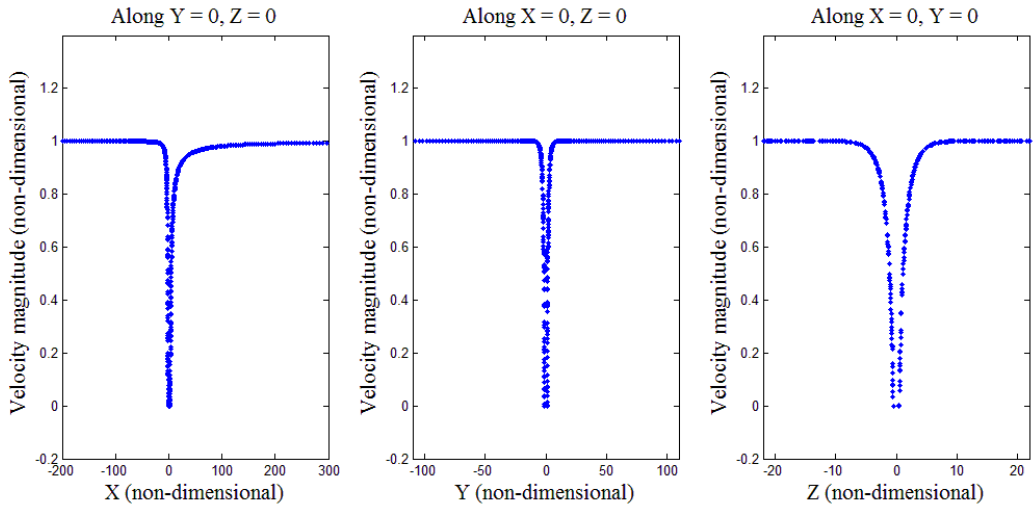

Figure 11: Velocity magnitude distribution in X, Y and Z directions (three-dimensional flow)

A mesh independence test for three-dimensional flows was also carried out taking Re = 1, AR = 20 as the test case. The result has been plotted in Figure 12. Increasing the mesh element size from 2.3 million to about 4.5 million resulted in about 0.35% change in the drag coefficient. A mesh size of about 3.3 million was chosen for all the simulations with parallel cylinders.

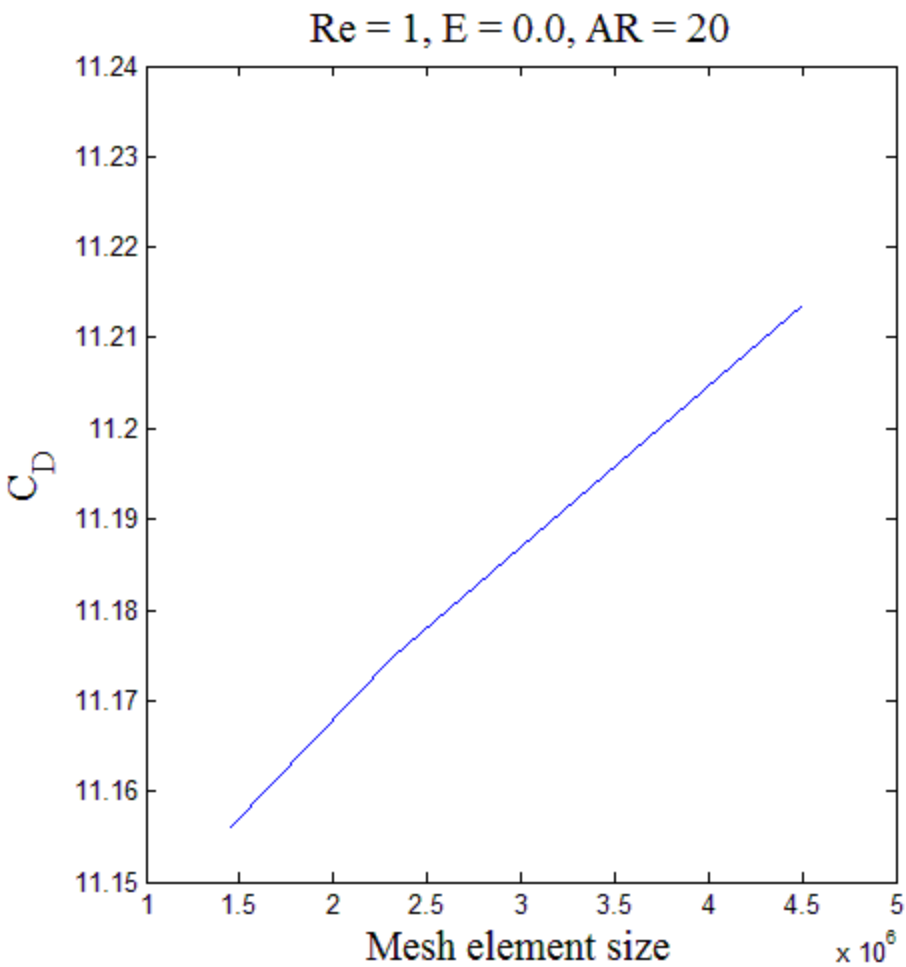

Figure 12: Mesh independence test for three dimensional flows over parallel cylinders

2.4 Two-dimensional simulation results and discussion

Simulations for elliptical cross-sections with ellipticities ranging from 0 to 0.7 with varying distances between the cylinders (*SeR* range 1 - 50) were carried out. In order to validate the simulations as well as understand the effect of cross-sectional variations, simulations were carried out on single cylinders for the complete range of Reynolds numbers. Figure 13, Figure 14 and Figure 15 shows the result of those simulations. The drag coefficients for circular cross-section cylinders are in good agreement with the findings of Sen *et al*. (2008) as well as Fornberg (1980) with an overall maximum error of approximately 1% at higher *Re*. At *Re* = 1, if drag coefficient is computed according to the following relation [9],

$C_D = \frac{16\pi}{Re\ln(7.4/Re)}$, the C_d is 25.1 for an isolated cylinder and hence the error is large. This huge difference in drag coefficients may be attributed to domain size being small. A detailed examination at the extremes of the Reynolds number range shows that at low *Re*, drag increases with decreasing ellipticity whereas the trend is reversed at high *Re*.

The drag coefficient was computed according to the formula,

$$C_d = \frac{F_{drag}}{0.5\rho U^2(2a)} = \frac{F_{drag}}{\rho U^2 a} = \frac{F_{drag}}{Re^2}.\frac{\rho a}{\mu^2}$$

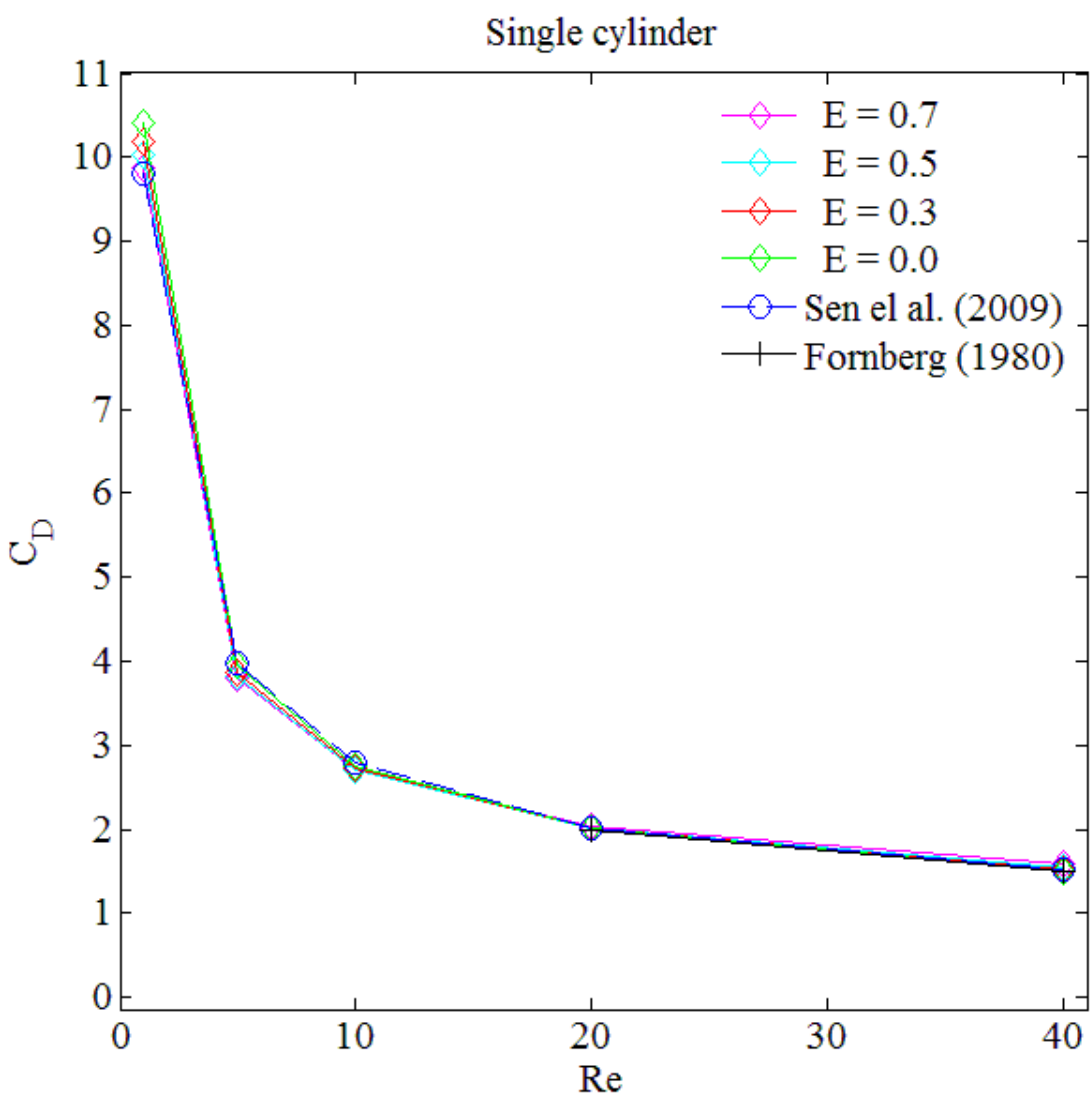

Figure 13: Validation of drag coefficient data obtained for single cylinders

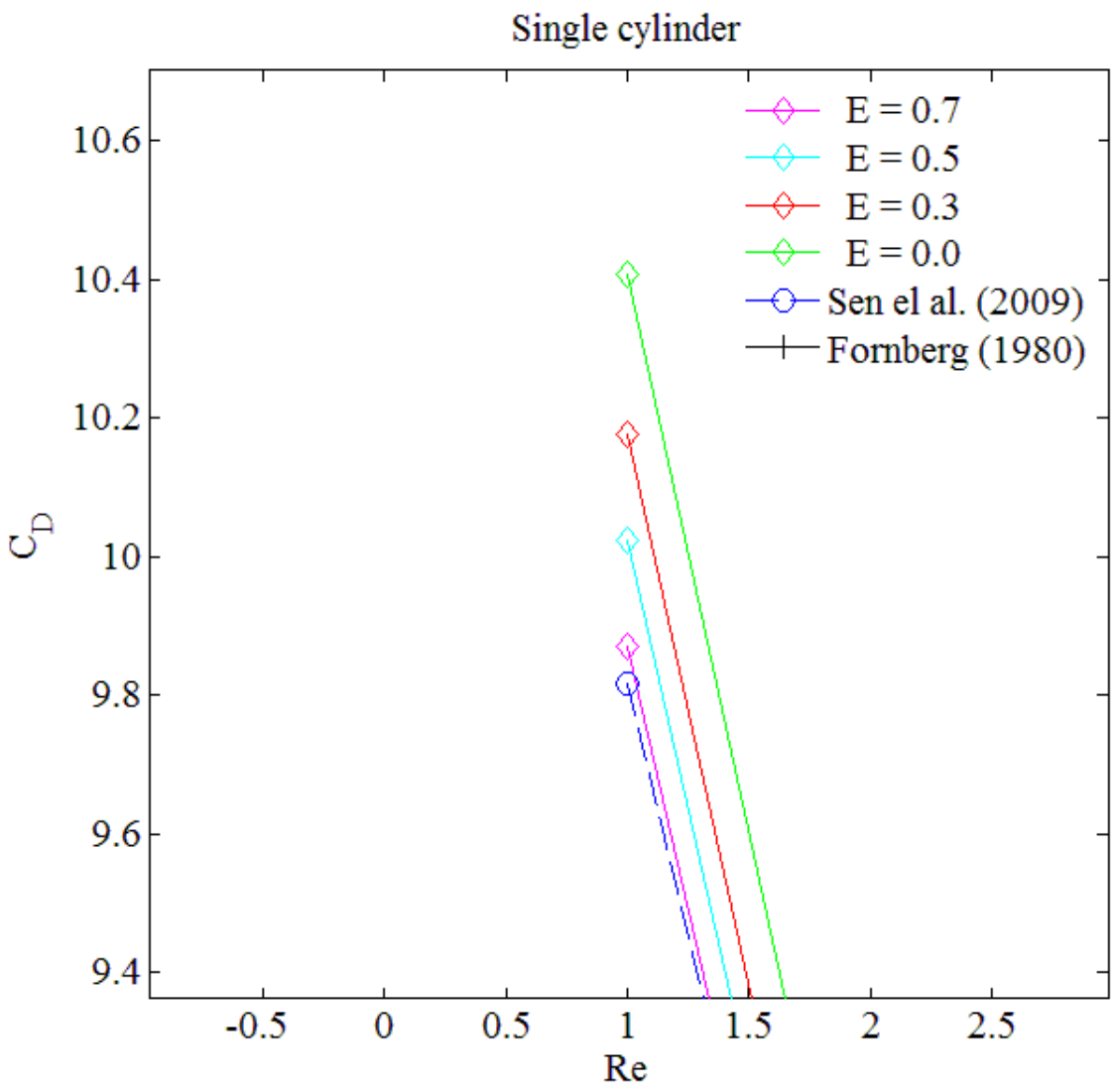

Figure 14: Trend of the drag coefficient at low Re

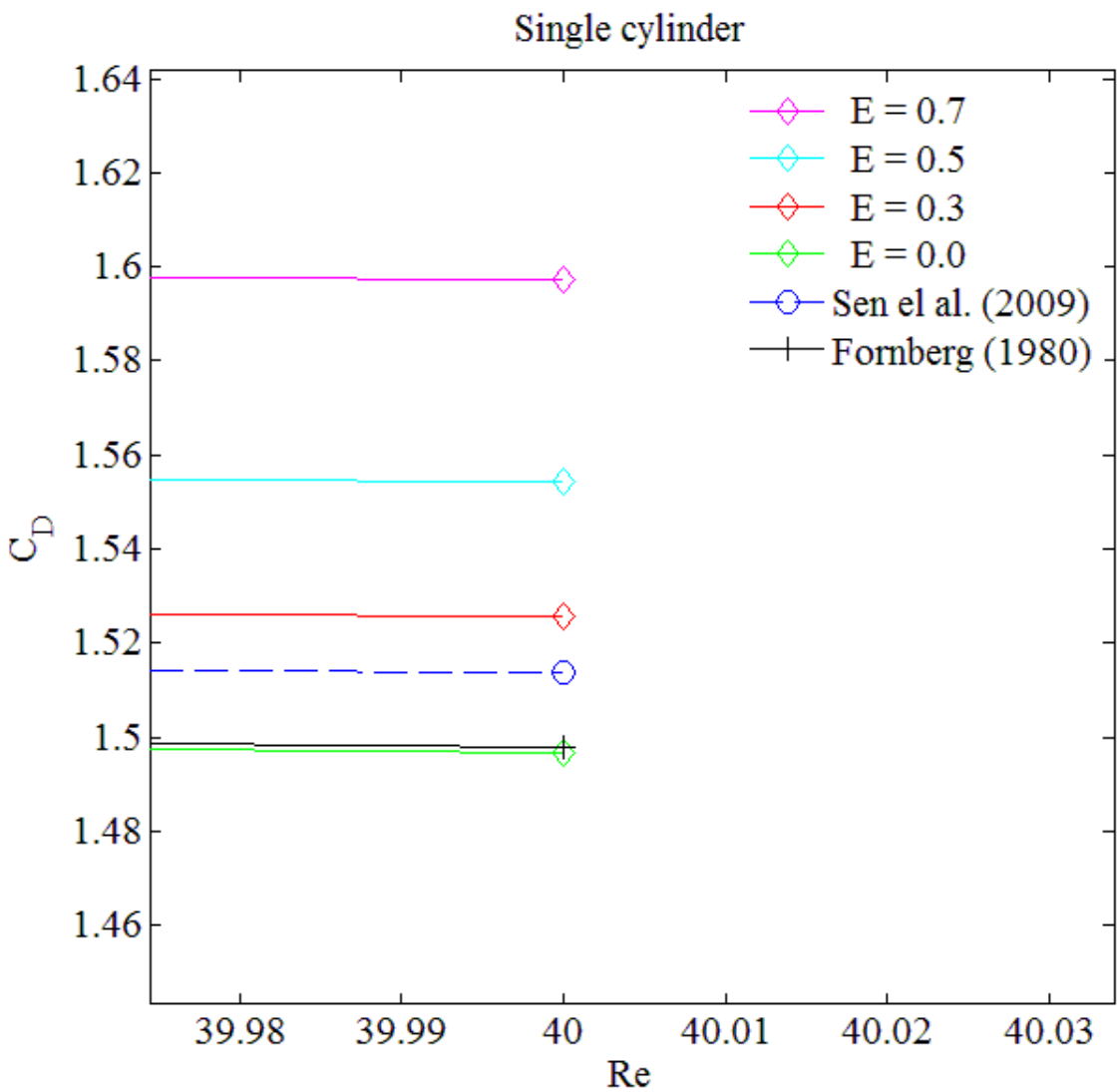

Figure 15: Trend of the drag coefficient at the higher Re

The drag coefficient C_d was plotted versus Reynolds number and the following graphs show the effect of the two geometrical parameters on front and rear cylinders. Figure 16 and Figure 17 show C_d vs. *Re* for different separation ratios for E = 0.7 for the front and rear cylinders. Figure 18 and Figure 19 show the same distribution for E = 0.0, that is, cylindrical cross-section.

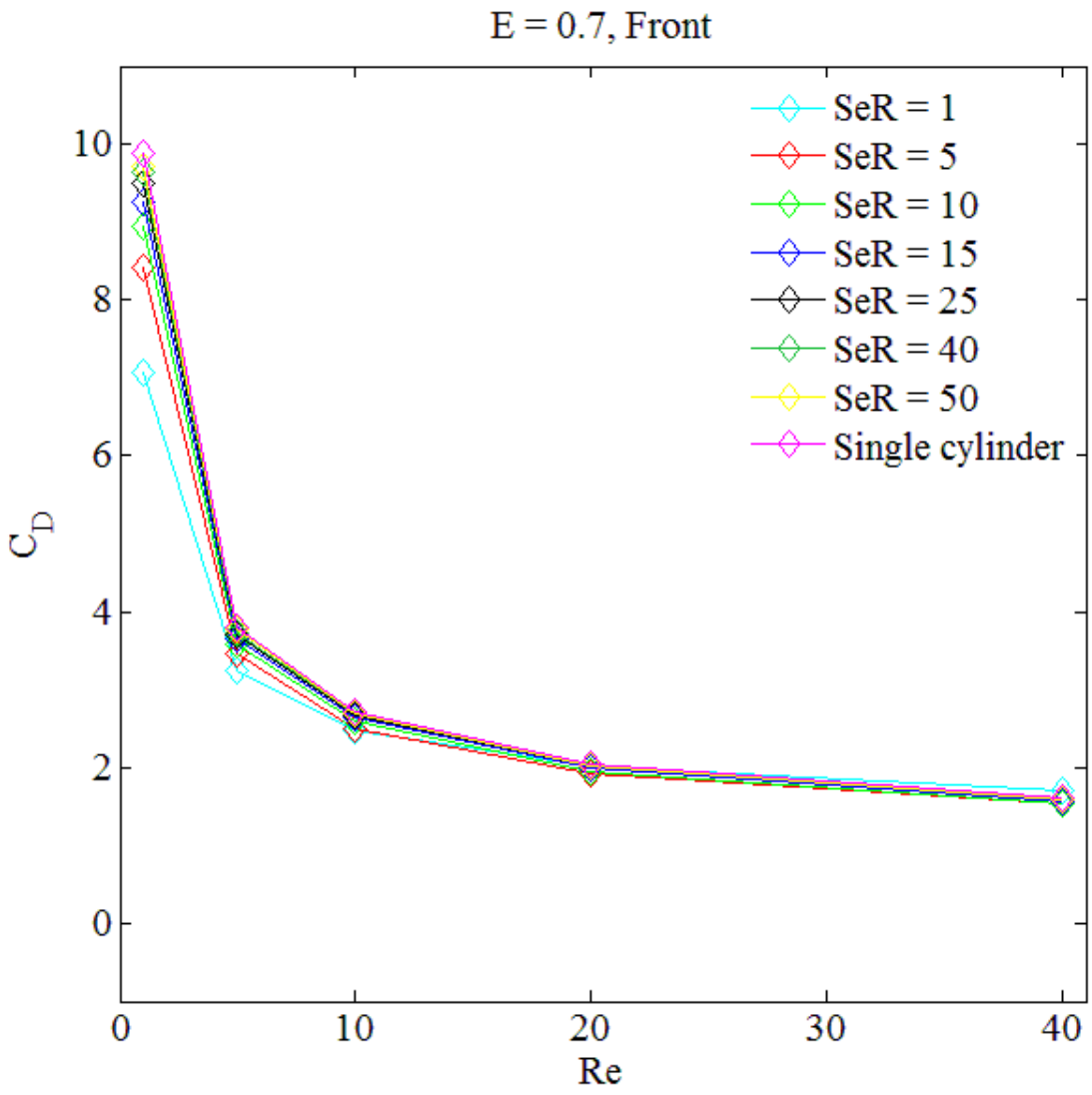

Figure 16: Drag coefficient of front cylinders with E = 0.7 at all SeR

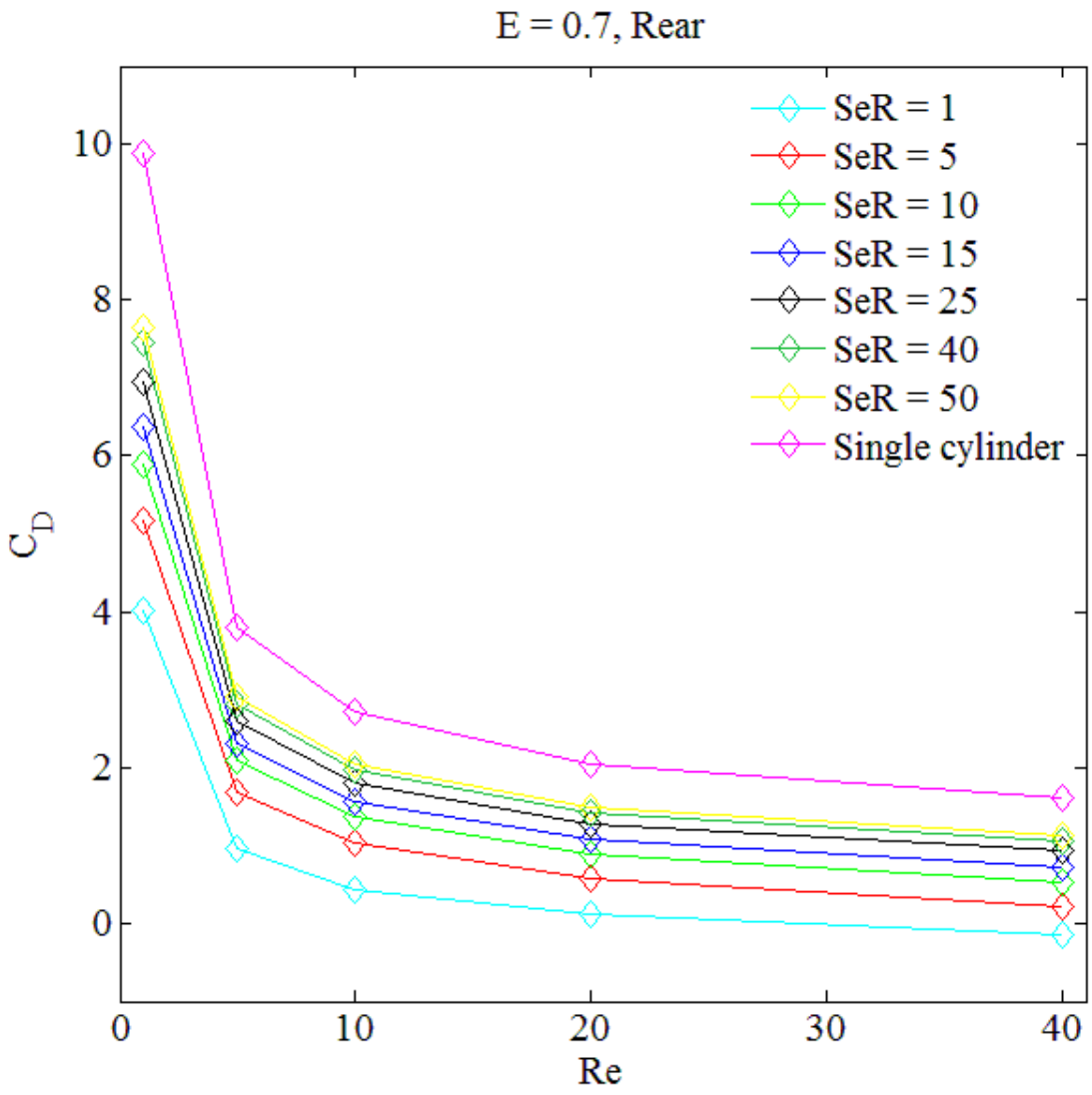

Figure 17: Drag coefficient of rear cylinders with E = 0.7 at all SeR

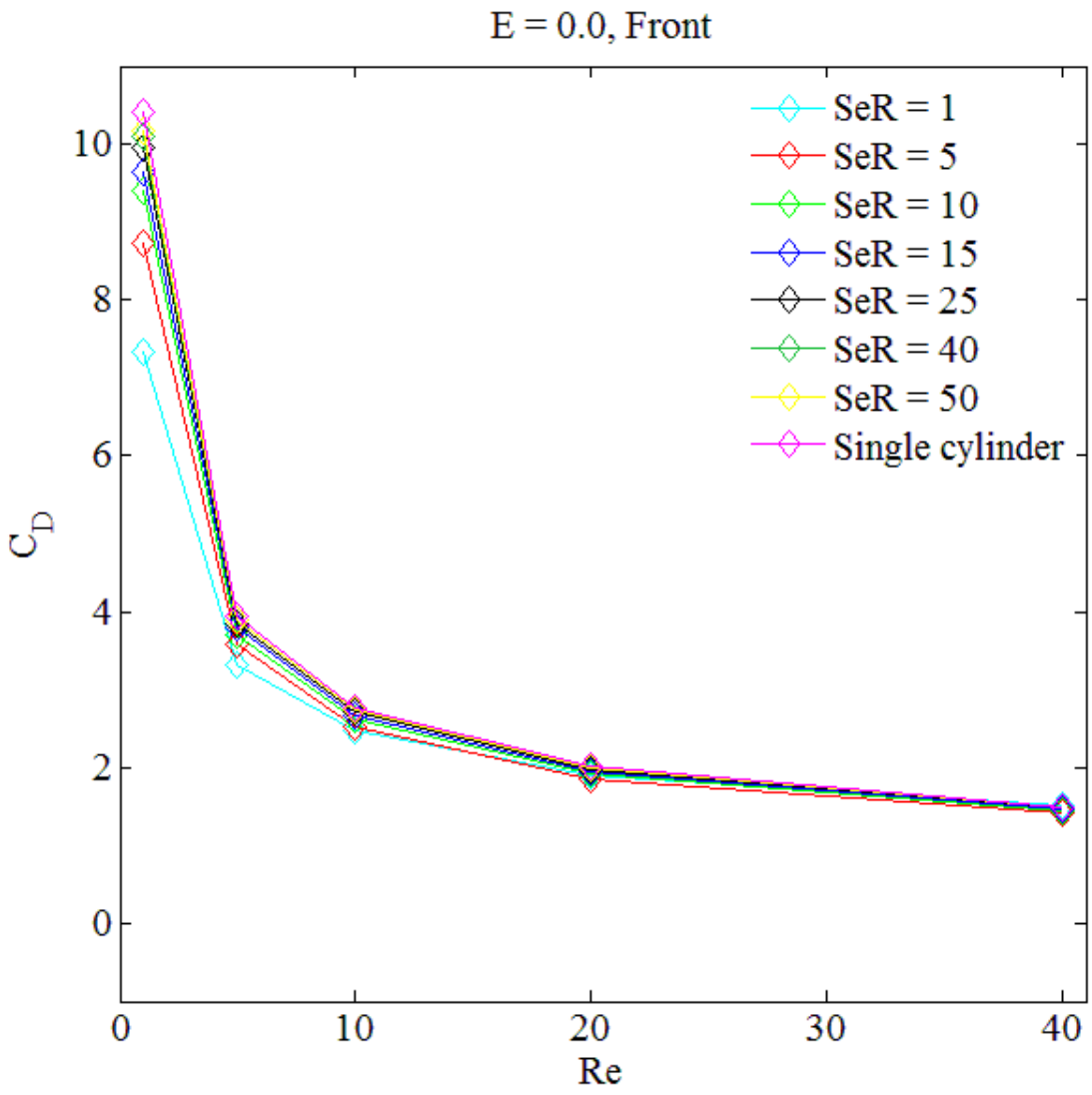

Figure 18: Drag coefficient of front cylinders with E = 0 at all SeR

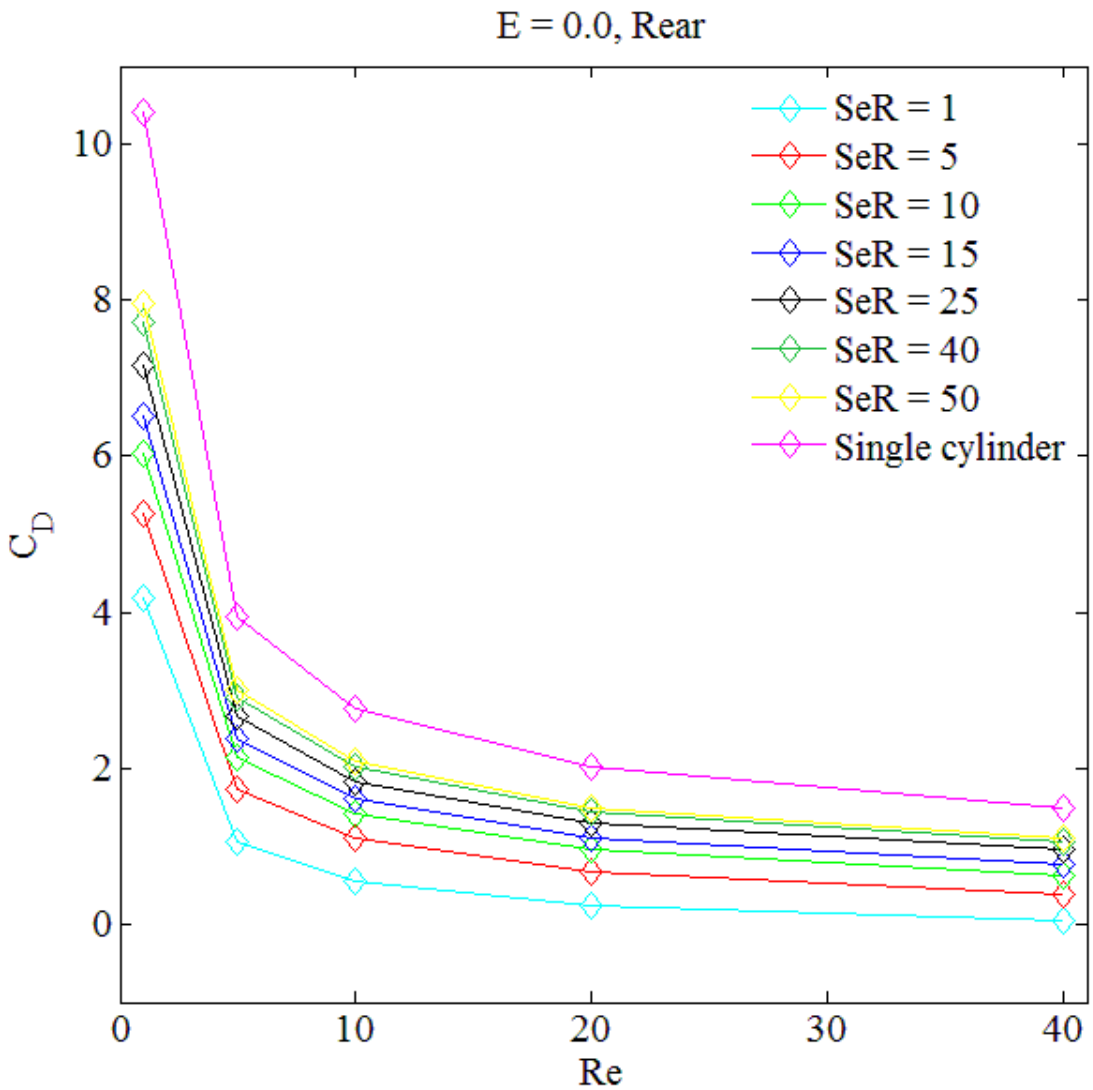

Figure 19: Drag coefficient of rear cylinders with E = 0 at all SeR

The above figures reveal that the drag values for the front cylinder remains in a smaller band than the rear cylinder, the maximum difference being at low Reynolds numbers, where drag increases with increasing separation between the cylinders. For both E = 0 and E = 0.7, the drag of the front cylinder at SeR = 1 and Re = 1, is less than that of a similar single cylinder by approximately 30%. At high Re, a similar uniform trend is not observed for drag on front cylinders but at SeR = 1, maximum drag is experienced by the front cylinder. The trend in drag of the rear cylinder shows uniformity all throughout. Drag always increases with increasing separation. At Re = 1, for both E = 0 and E = 0.7, the drag on the rear cylinder at SeR = 1, is less than that of a similar single cylinder by approximately 60%. At Re = 40 and SeR = 1 there is an order of magnitude reduction of the drag on

the rear cylinder compared with a single cylinder. For high ellipticities, the drag on the rear cylinder may even be negative for small separations (*SeR*~1). The negative drag is believed to be caused by the fact that the rear cylinder is located in the portion of the upstream cylinder wake that would have been occupied by two wake vortices, whose velocity component along the centreline is opposite to the direction of the freestream.

Figure 20 and Figure 21 show the drag coefficient for different ellipticities for *SeR* = 1.0 for front and rear cylinders. The same is shown in Figure 22 and Figure 23 for *SeR* = 50.0.

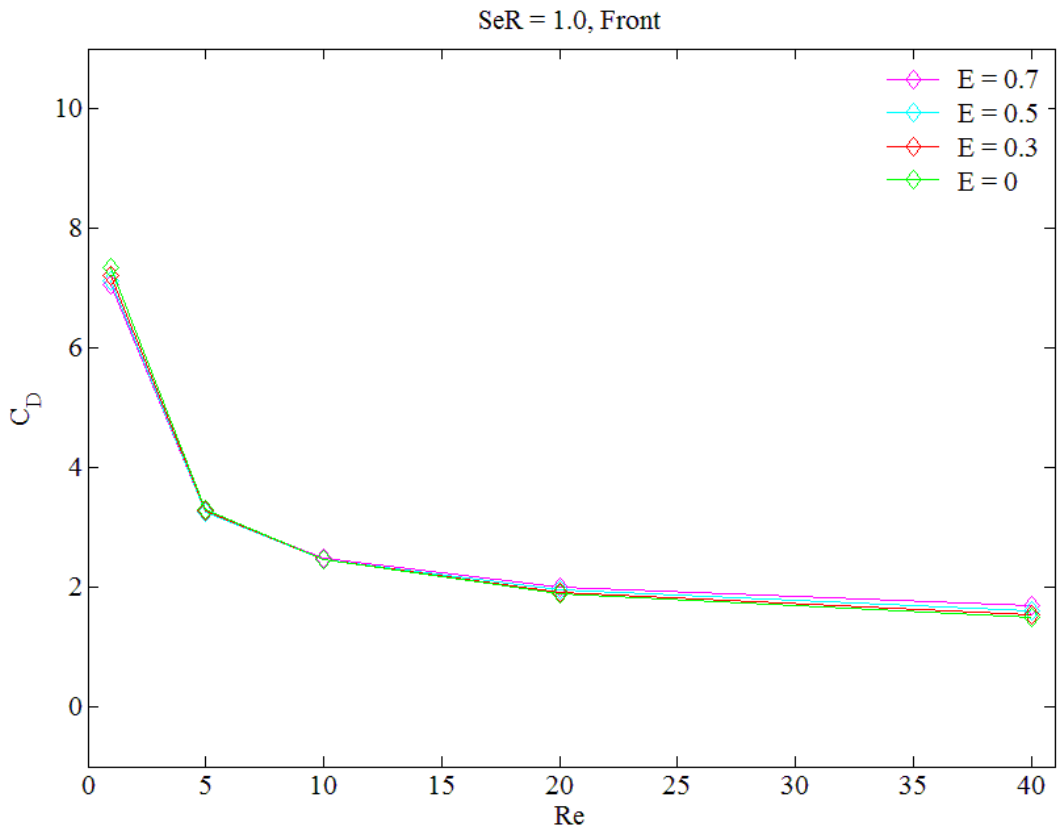

Figure 20: Effect of cross-sectional shape for front cylinders at SeR = 1.0

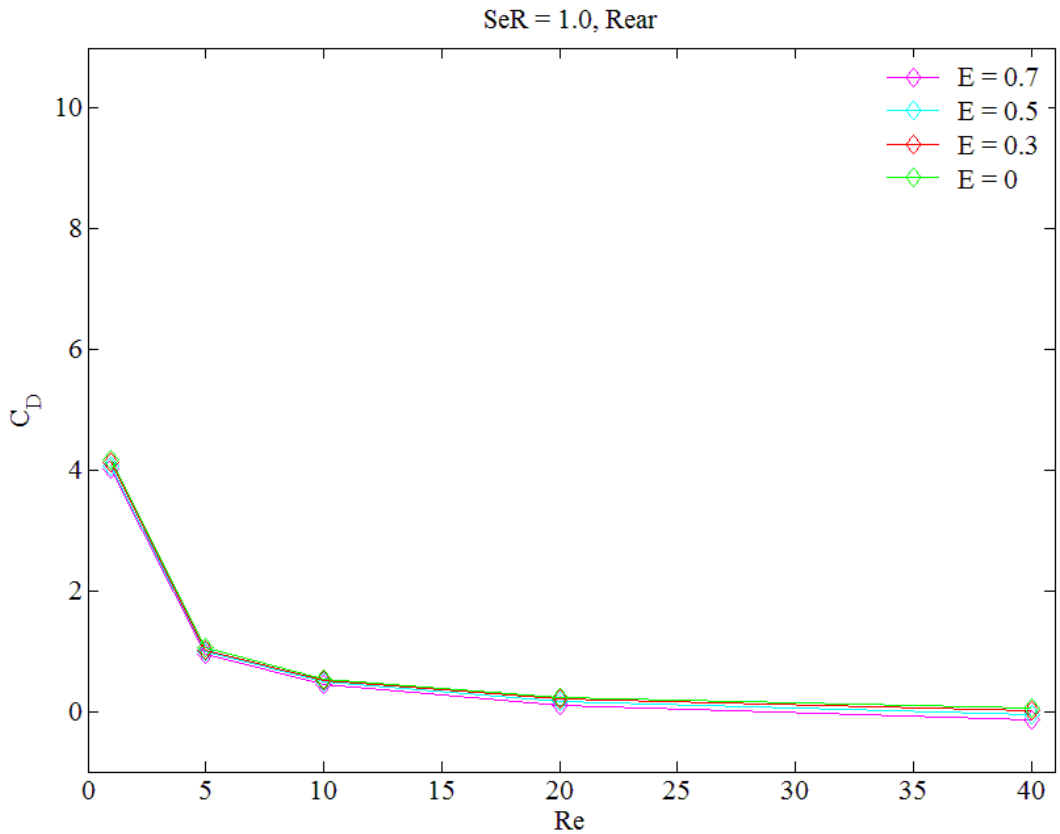

Figure 21: Effect of cross-sectional shape for rear cylinders at SeR = 1.0

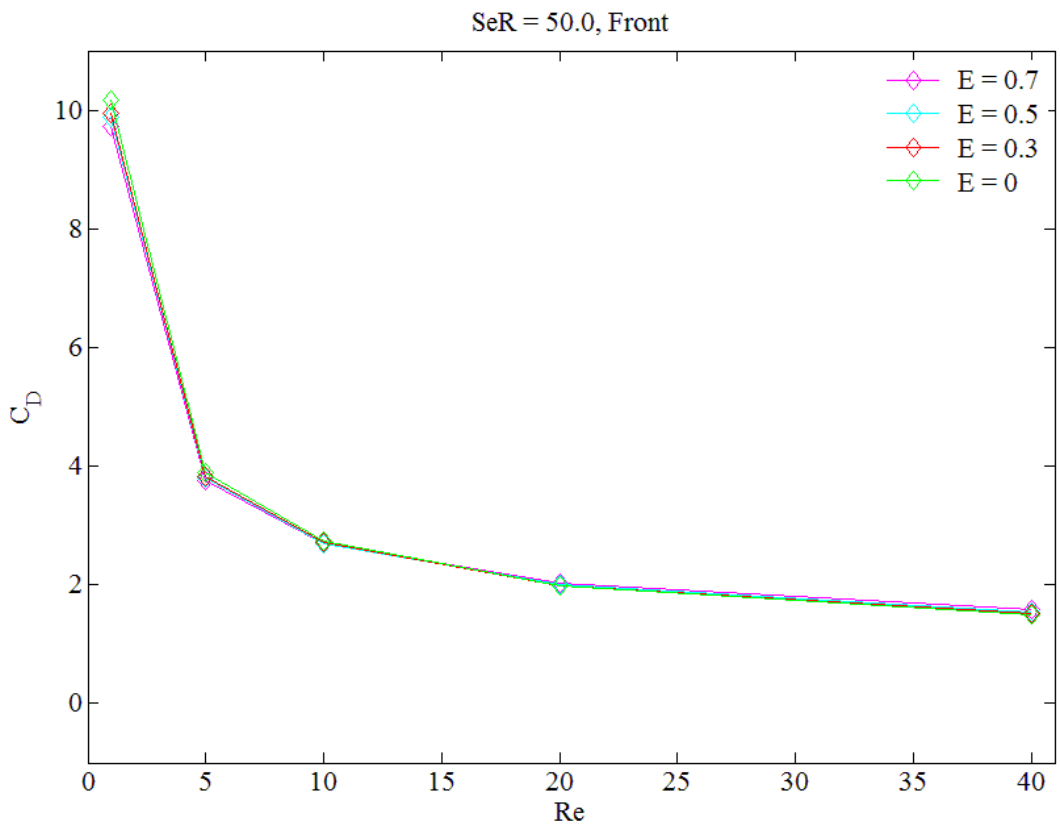

Figure 22: Effect of cross-sectional shape for front cylinders at SeR = 50.0

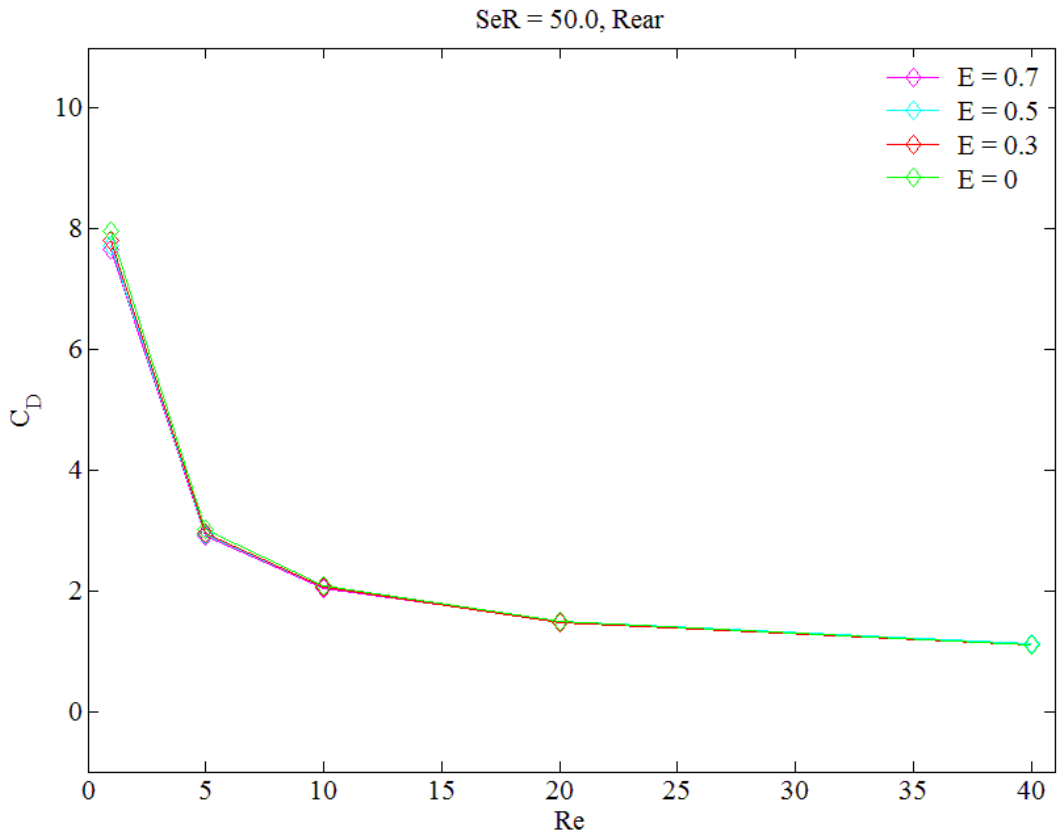

Figure 23: Effect of cross-sectional shape for rear cylinders at SeR = 50.0

It may seem from the above graphical data that there is no significant difference with variations in the cross-sections of the cylinders. A closer examination of the results reveals that for the front cylinders, drag at low *Re* (~1) always increases with decreasing ellipticity but the trend is reversed at higher *Re* (~40). A similar trend is observed for rear cylinders at both *SeR* = 1 and *SeR* = 50 but only at *Re* = 1. When at small separation, the drag coefficient still increases with decreasing ellipticity but the opposite trend is observed at large separation.

Figure 24 shows the effect of separation between fibers at different *Re*. At very close distances at *Re* = 1, the drag on the rear cylinder may be as low as around 57% of drag on front cylinder. This value drops down to around 20% when *Re* is increased to 10.

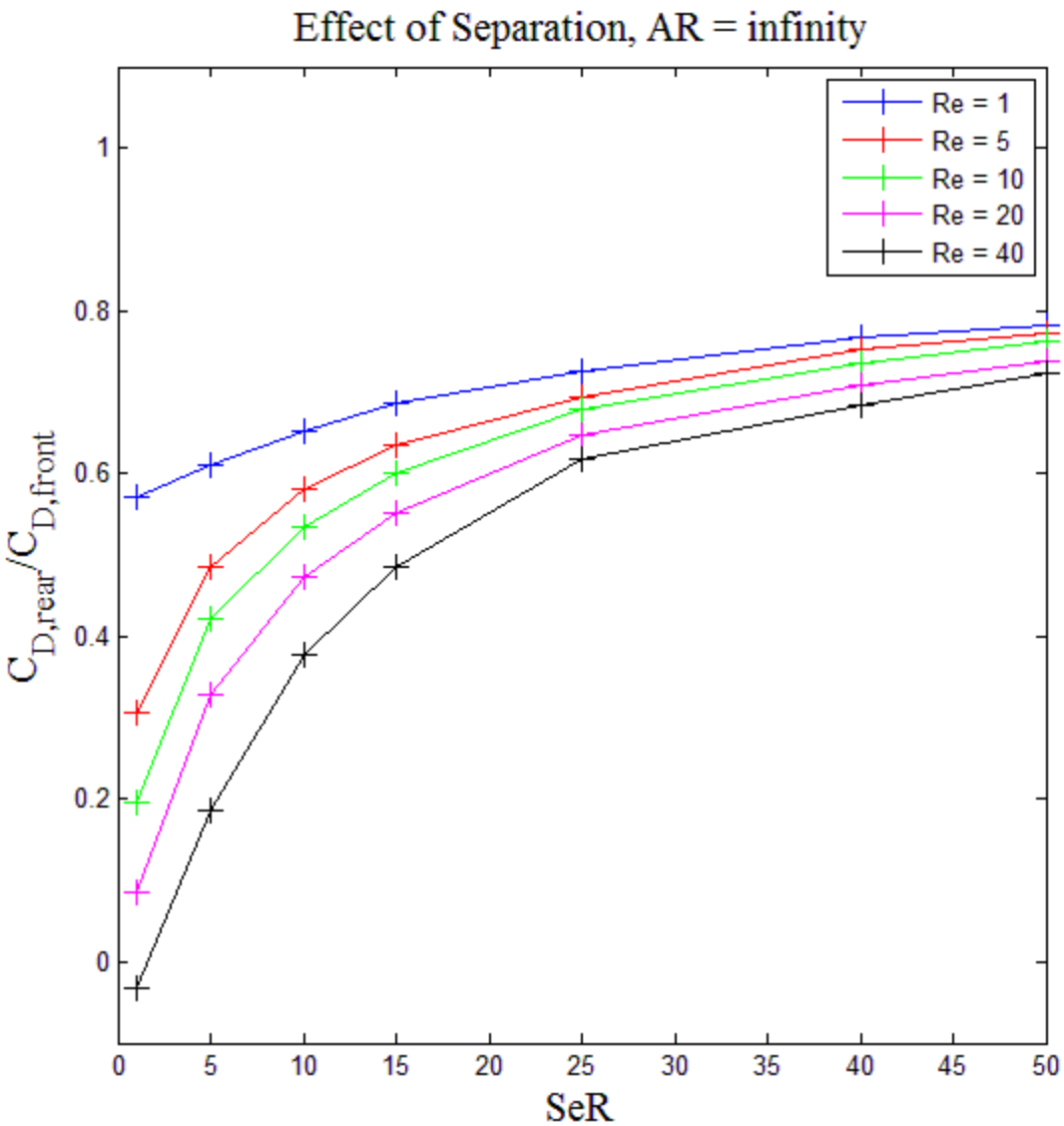

Figure 24: Variation of ratio of drag on rear cylinder to drag on front cylinder with separation at all Re

Streamline patterns for flows at SeR = 1 and SeR = 5 and Re = 1 and Re = 40 are shown in the following figures. The wake region forming in between the cylinders at *Re* = 1 and *SeR* = 1 has been shown in detail in Figure 26. At greater separation, as expected the flow pattern around the front and rear cylinders is more or less the same at *Re* = 1 due to attached flow but at higher *Re*, a long wake is present behind the front cylinder and a relatively smaller wake behind the rear cylinder.

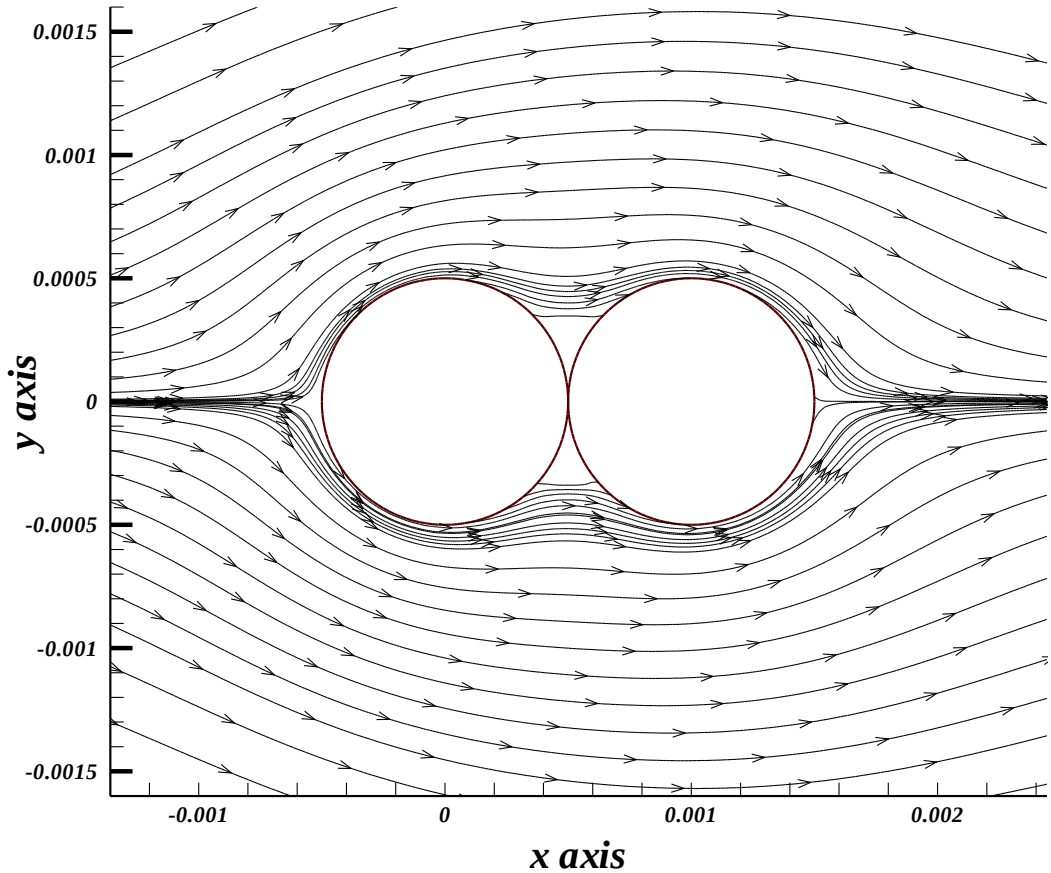

Figure 25: Streamline pattern at SeR = 1, Re = 1

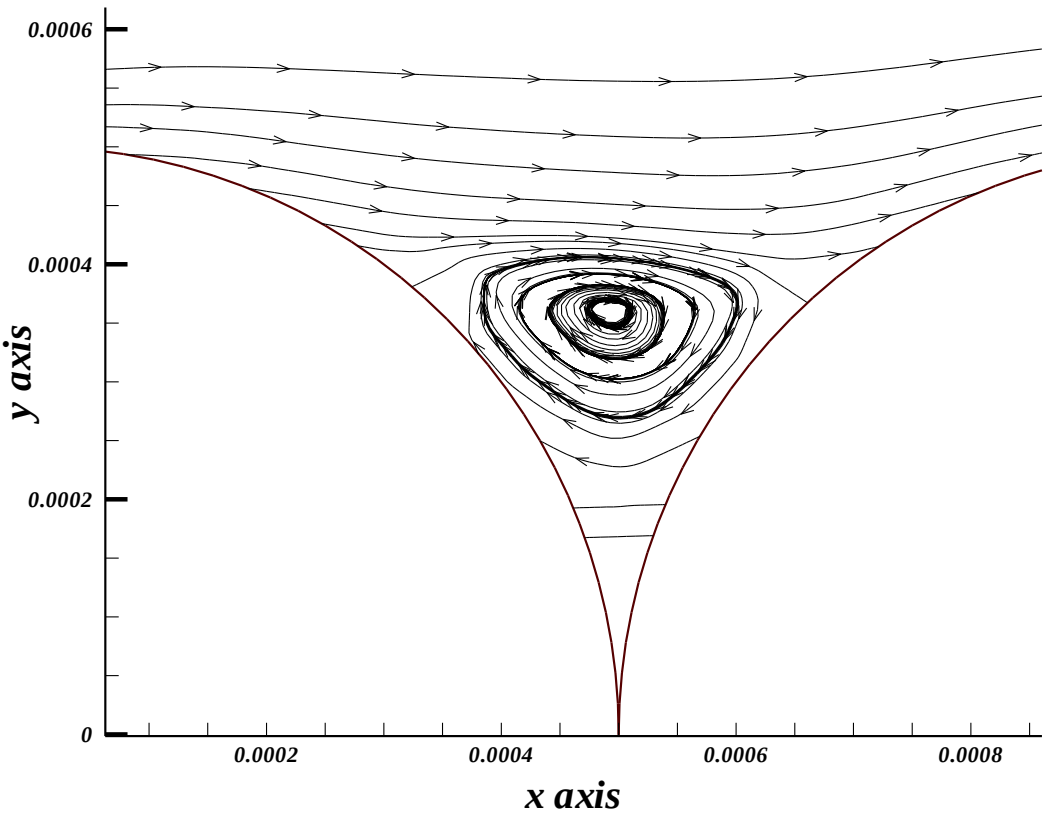

Figure 26: Wake in between the cylinders at SeR = 1, Re = 1

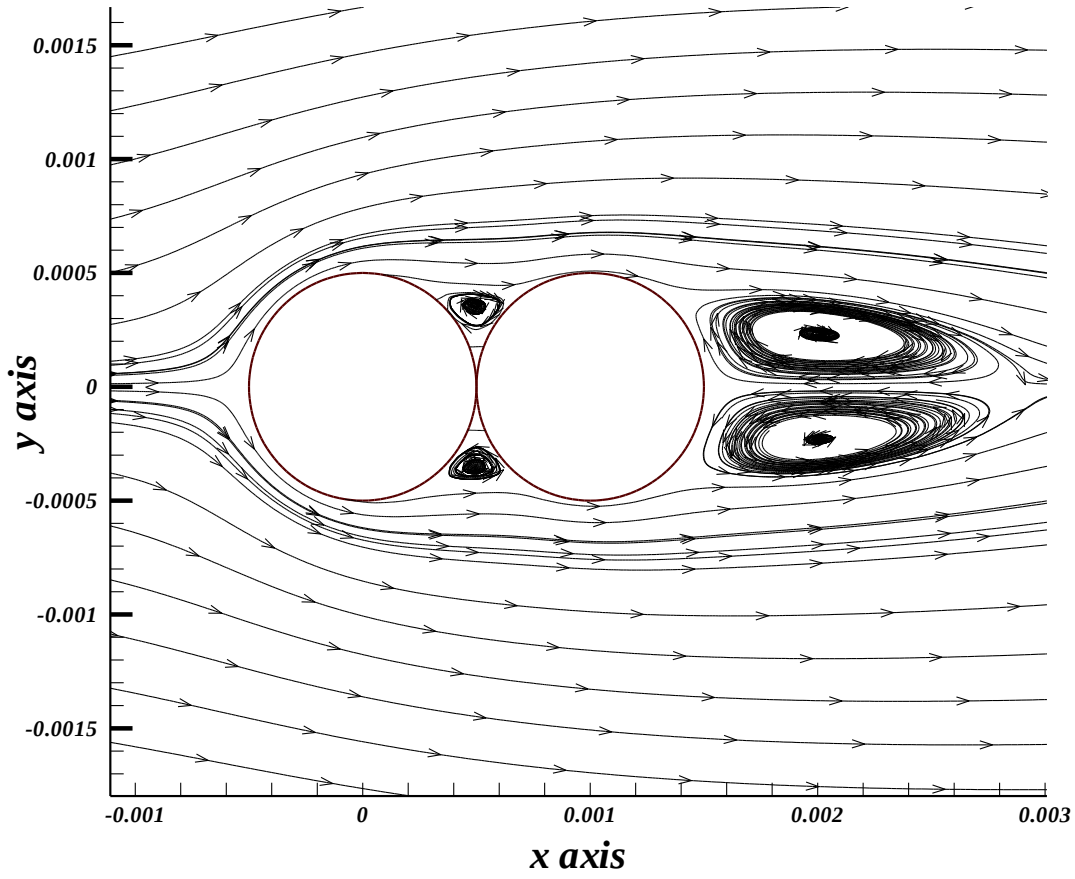

Figure 27: Streamline pattern at SeR = 1, Re = 40

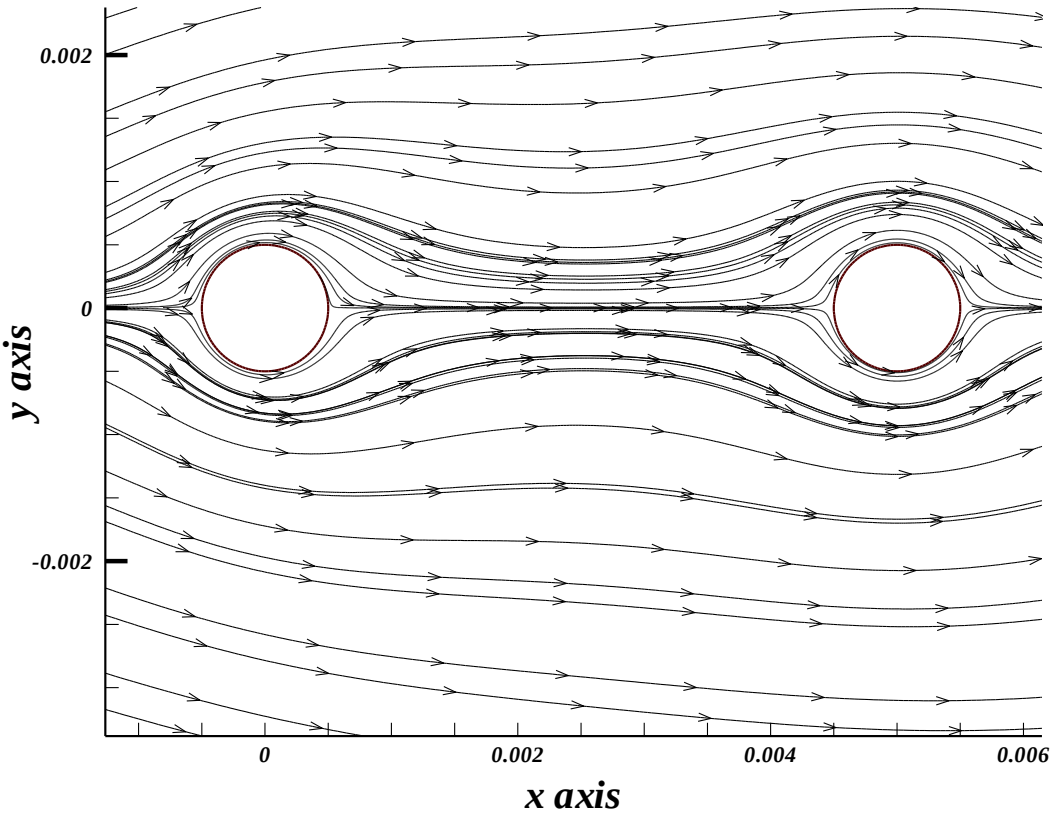

Figure 28: Streamline pattern at SeR = 5, Re = 1

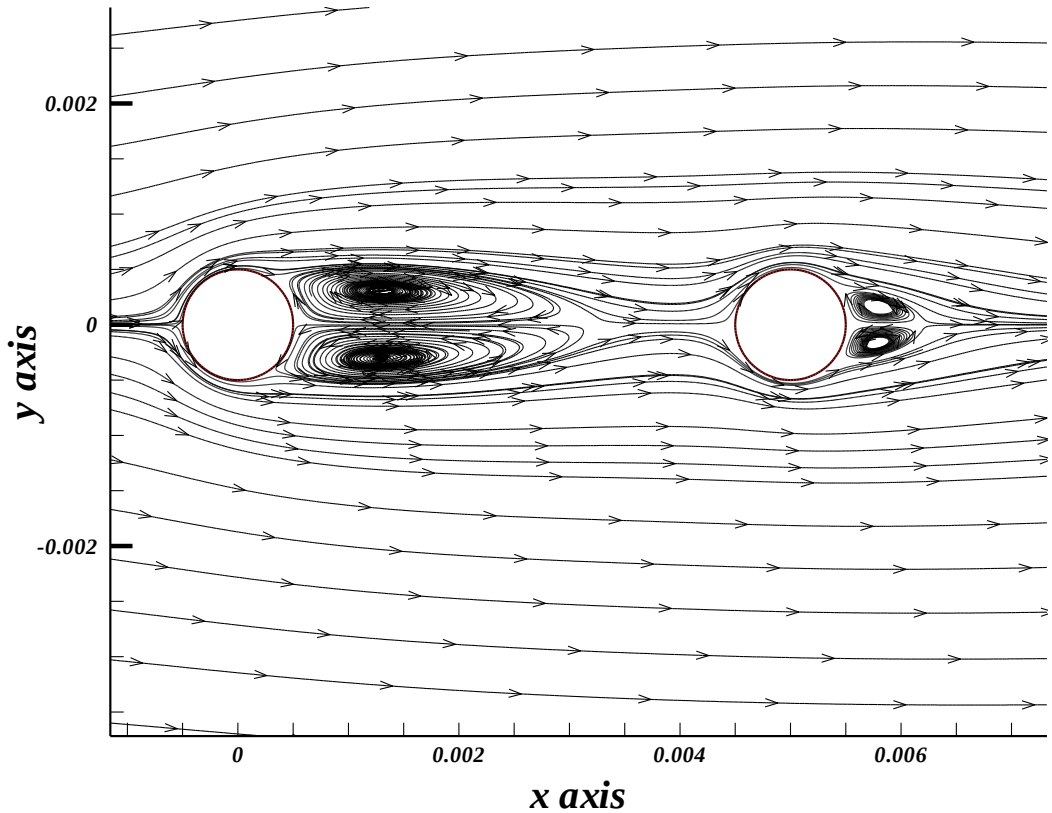

Figure 29: Streamline pattern at SeR = 5, Re = 40

2.5 Three-dimensional simulation results and discussion: parallel cylinders

Simulations for three geometrical parameters, *SeR* (2 - 20), *E* (0, 0.7) and *AR* (2 - 20) were carried out. Figure 30 and Figure 31 show the C_d vs. *Re* plot.

The drag coefficient was computed according to the formula,

$$C_d = \frac{F_{drag}}{0.5\rho U^2 LD} = \frac{F_{drag}}{0.5\rho U^2 AR(4a^2)} = \frac{F_{drag}}{2\rho U^2 ARa^2} = \frac{F_{drag}}{Re^2}.\frac{2}{AR}.\frac{\rho}{\mu^2}$$

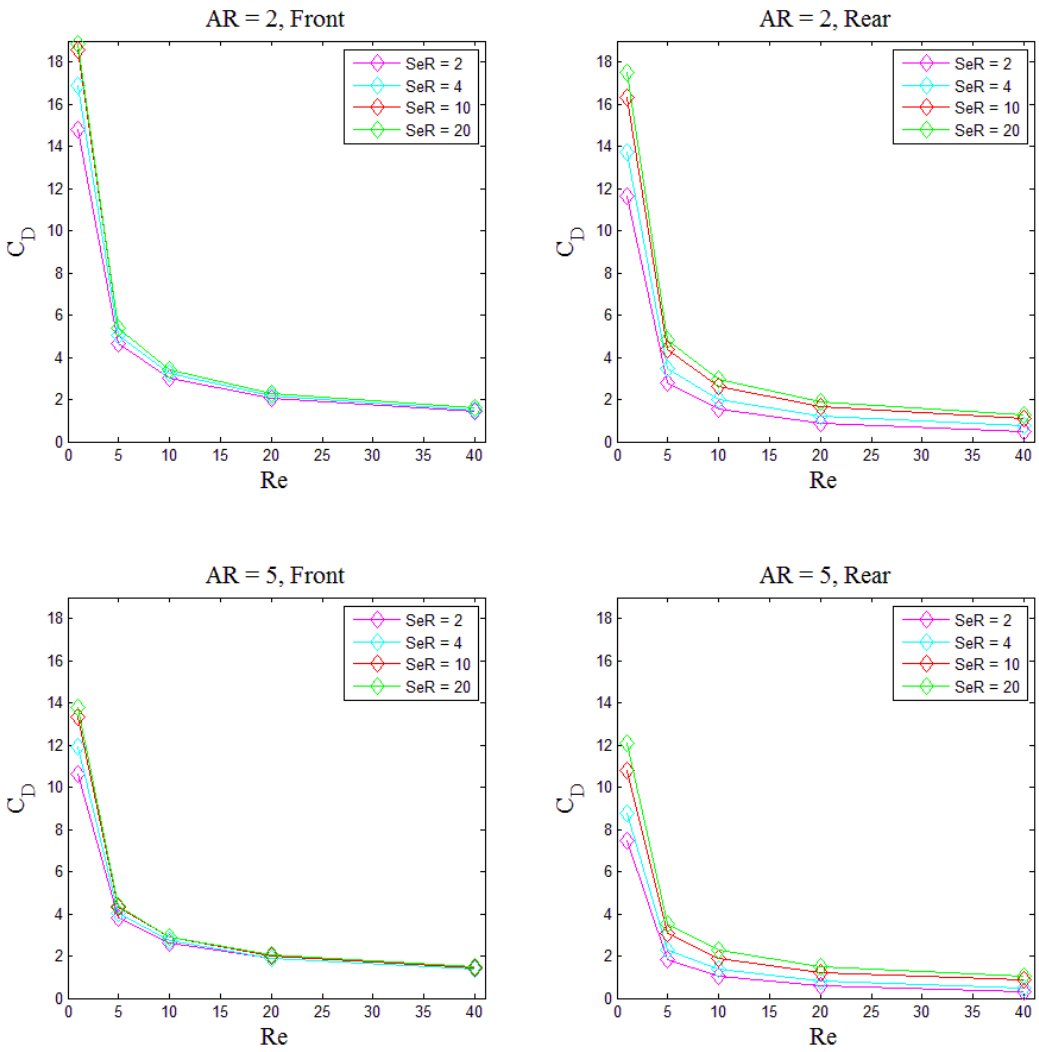

Figure 30: Drag coefficient at AR = 2 and AR = 5 at all SeR

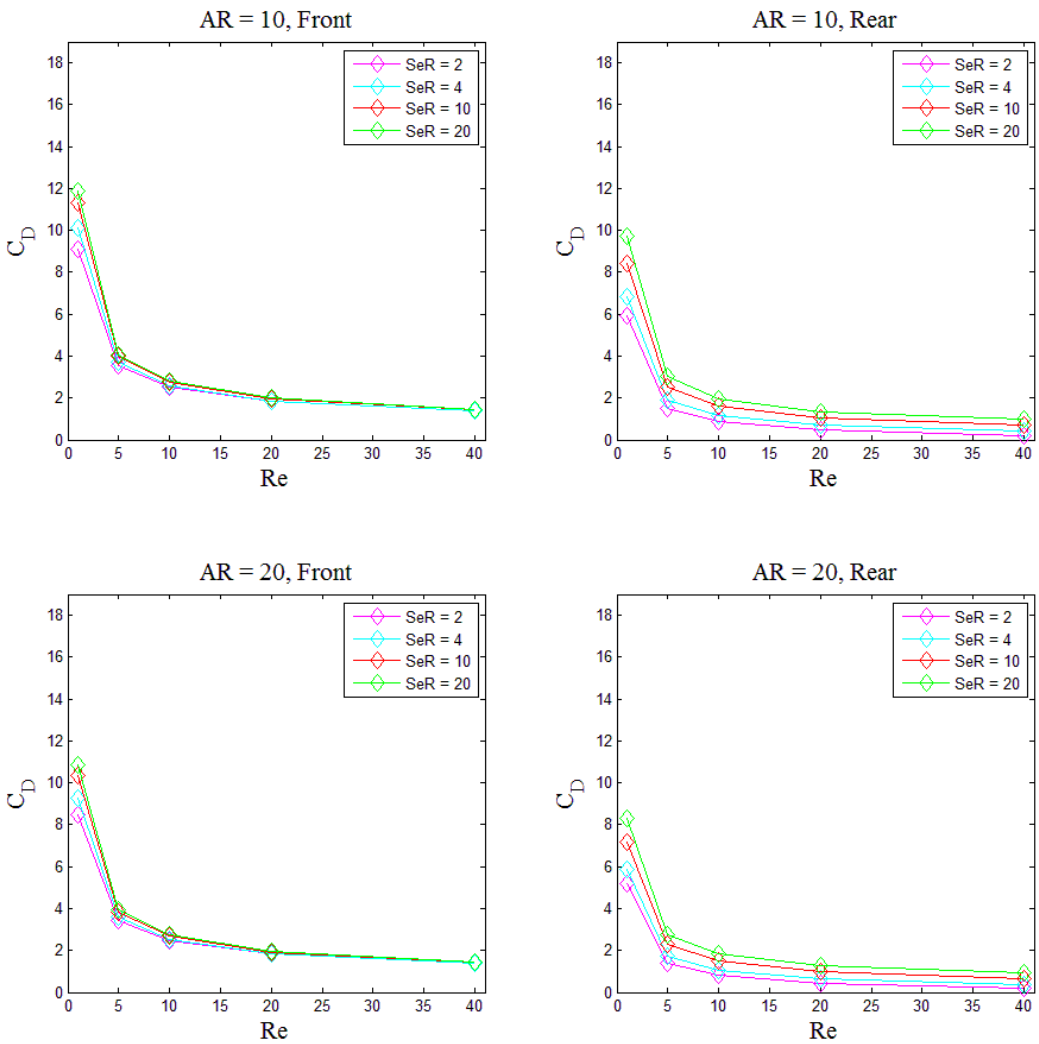

Figure 31: Drag coefficient at AR = 10 and AR = 20 at all SeR

The above graphical data show similar trends as in the two-dimensional cases. The drag values on the front cylinder are closely spaced compared to those on the rear cylinder, the band being most broad at low Reynolds numbers. The trend for rear cylinder, as in 2D, remains the same all throughout. It may be noticed that for both front and rear cylinders the drag coefficient decreases asymptotically with increasing aspect ratio and the following plot in Figure 32 verifies that they converge to the drag coefficients of infinitely long cylinders.

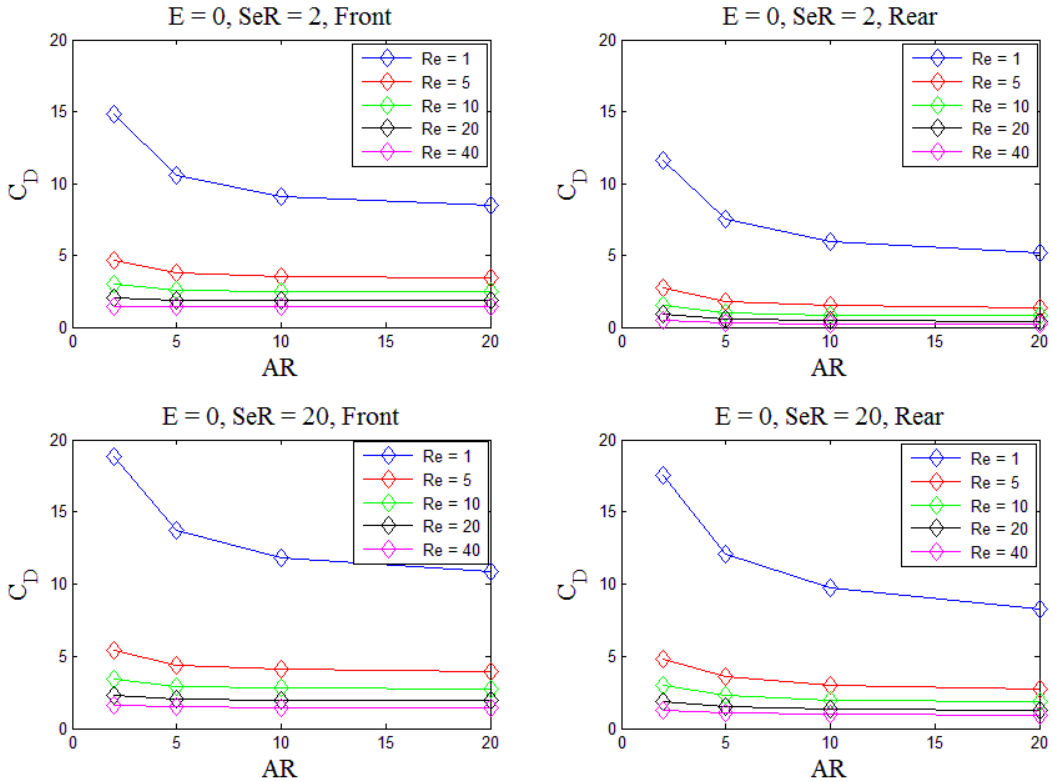

Figure 32: Effect of AR on drag coefficient

The ratio of drag coefficients for finite to infinite cylinders has been shown in Figure 33Figure 33: Drag coefficient normalized with that of infinite aspect ratio cylinder. It is evident from the plots that as the aspect ratio is increased it asymptotically reaches drag coefficient of infinite cylinder at the same separation ratio and Reynolds number.

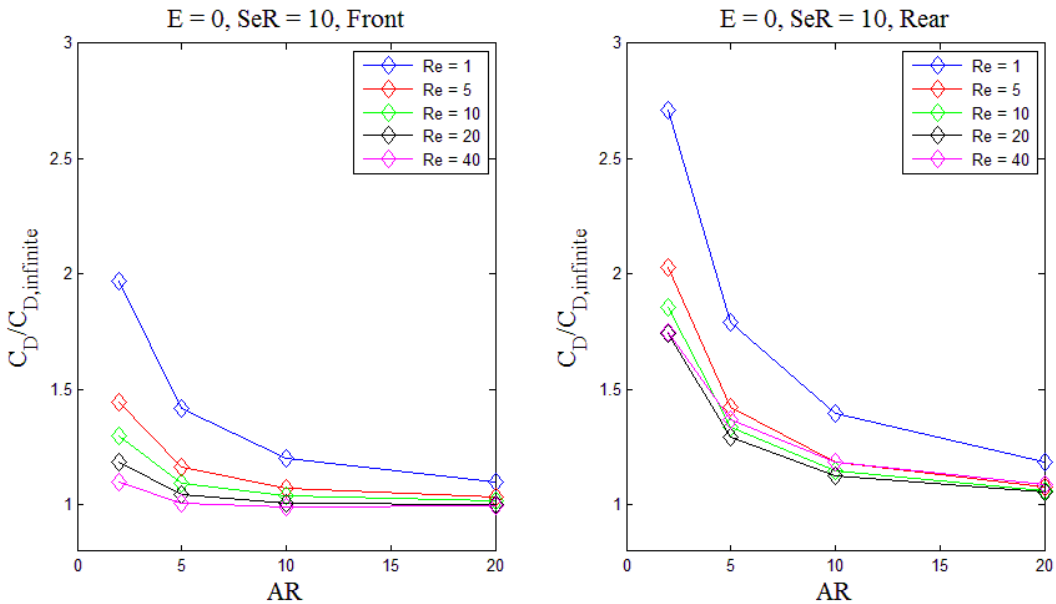

Figure 33: Drag coefficient normalized with that of infinite aspect ratio cylinder

An exponential curve-fit was obtained for front fiber at *Re* = 1 and *SeR* = 10 in the above plots,

$$C_d = 0.8604\, e^{-0.2\,AR} + 2.28\, e^{-AR} + 1.086,$$

according to which, drag coefficient for infinite cylinder is 1.086, which indicates an error of 8.6%.

Ratio of drag on rear cylinder to that on front cylinder is shown in Figure 34 for all situations.

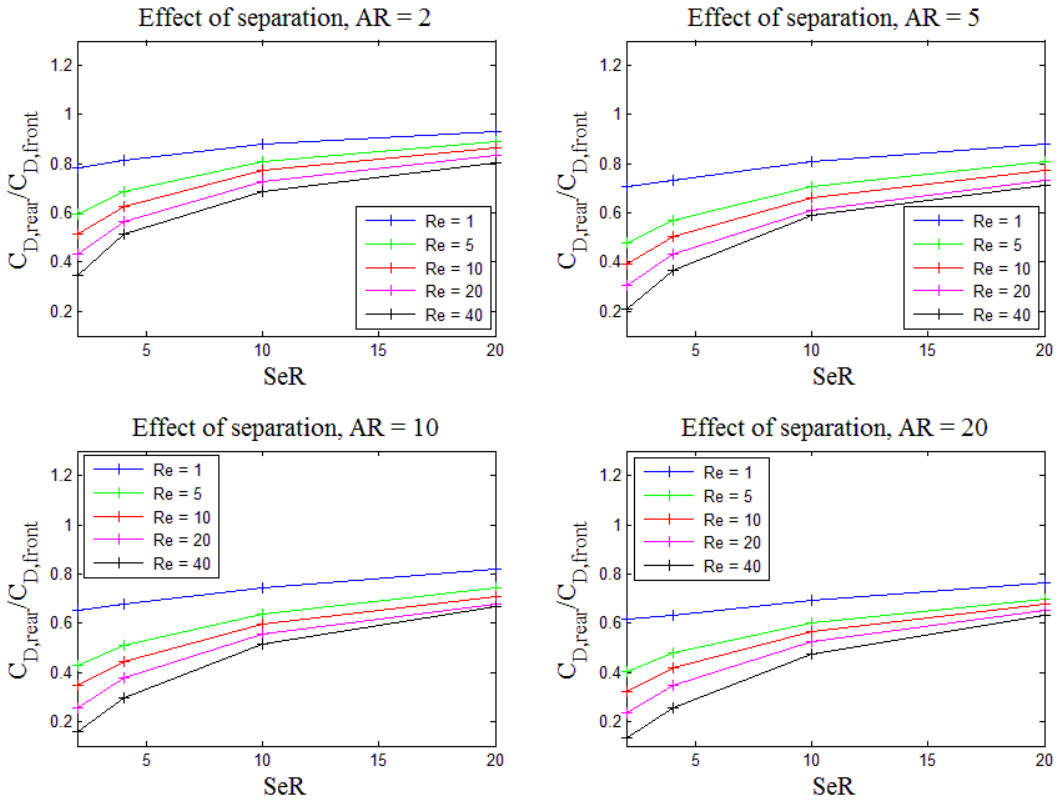

Figure 34: Effect of SeR on ratio of drag on rear cylinder to drag on front cylinder for all Re

Streamlines have been shown in the following figures for *Re* = 1 and *Re* = 40 at *SeR* = 2. The wake structures are three-dimensional in nature as may be seen from Figure 35, Figure 36 and Figure 37. As *Re* rises, this wake structure slowly vanishes. The flow is seen to be attached behind the rear cylinder at *Re* = 1. At *Re* = 40, the wake structure is seen behind the rear cylinder, the wake-length being almost zero at the ends and maximum at the centre.

Streamline plots for cylinders of *AR* = 2, 5 and 20 at *SeR* = 2 and 5 and at *Re* = 1 and 40 are shown in the following figures. As may be seen from the plots, the wake structures in between the cylinders and behind are of highly three-dimensional nature. At small separations and *Re* = 1, the flow is not completely attached and there is a three-dimensional wake in between the cylinders. At high *Re*, the wake has greatest length near the centre of the rear cylinder and reduces in size towards the ends.

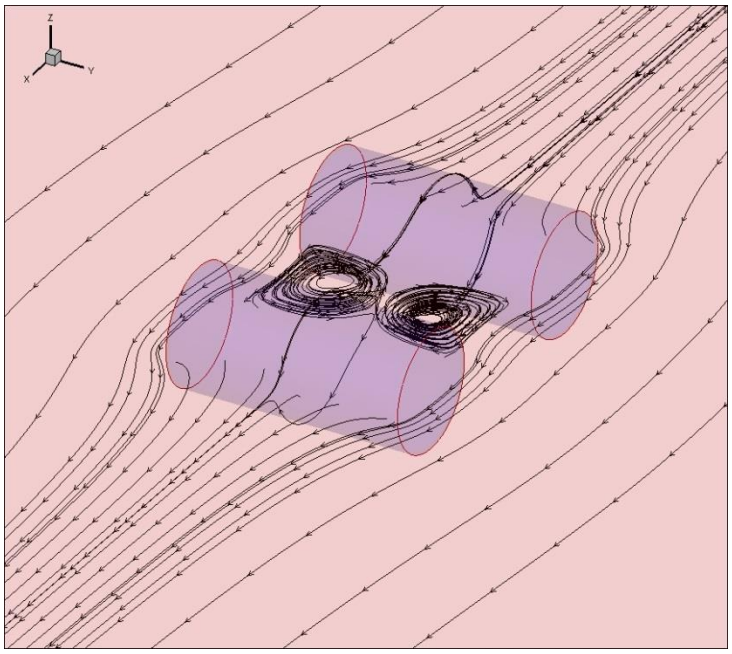

Figure 35: Isometric view of flow over parallel cylinders at Re = 1, AR = 2, SeR = 2

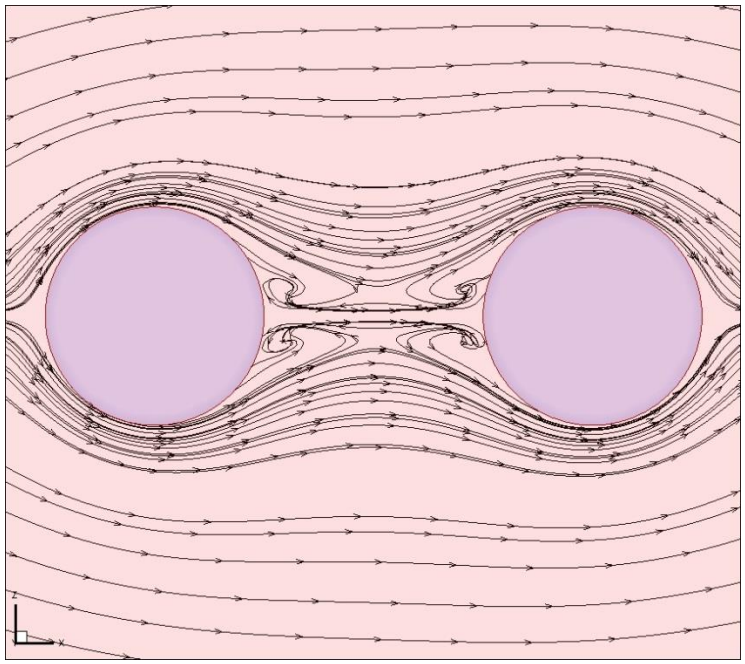

Figure 36: XZ view of flow over parallel cylinders at Re = 1, AR = 2, SeR = 2

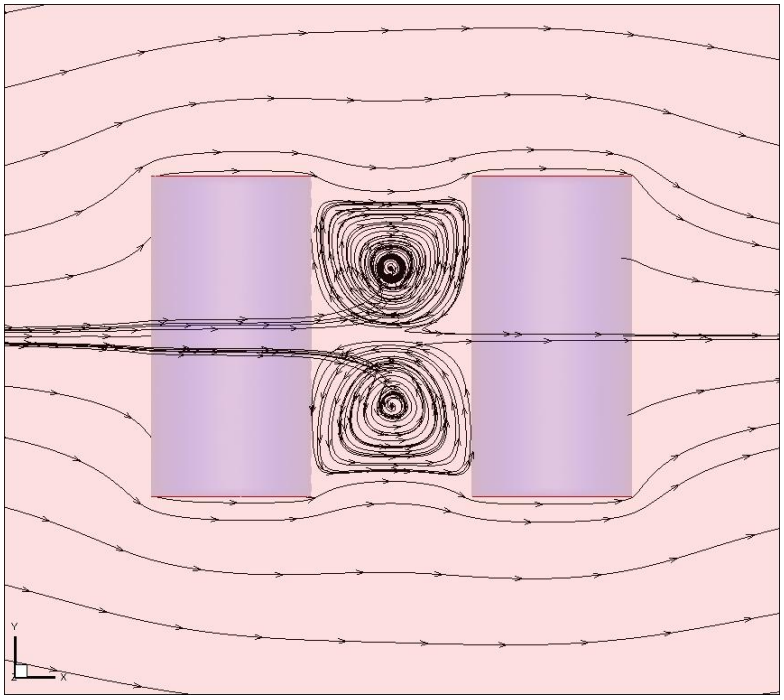

Figure 37: XY view of flow over parallel cylinders at Re = 1, AR = 2, SeR = 2

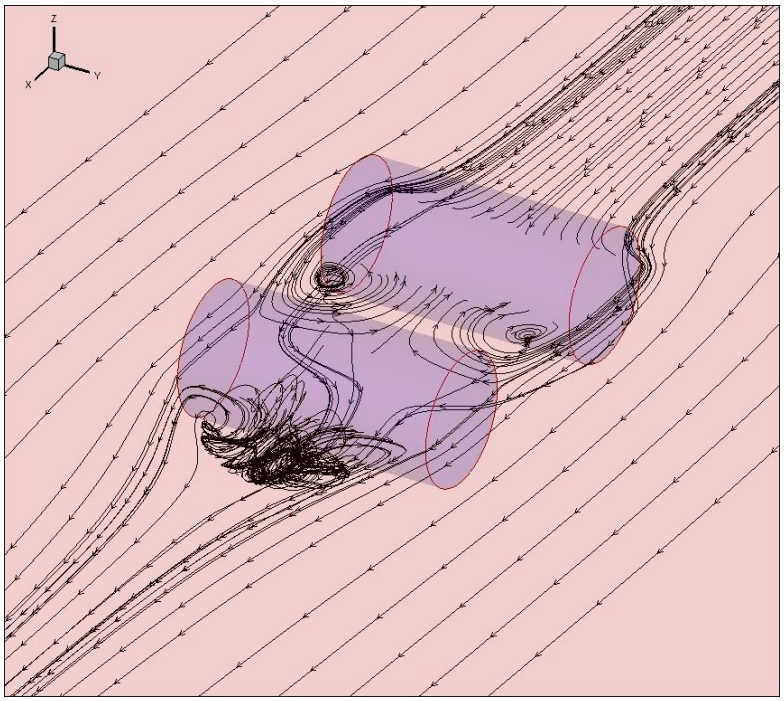

Figure 38: Isometric view of flow over parallel cylinders at Re = 40, AR = 2, SeR = 2

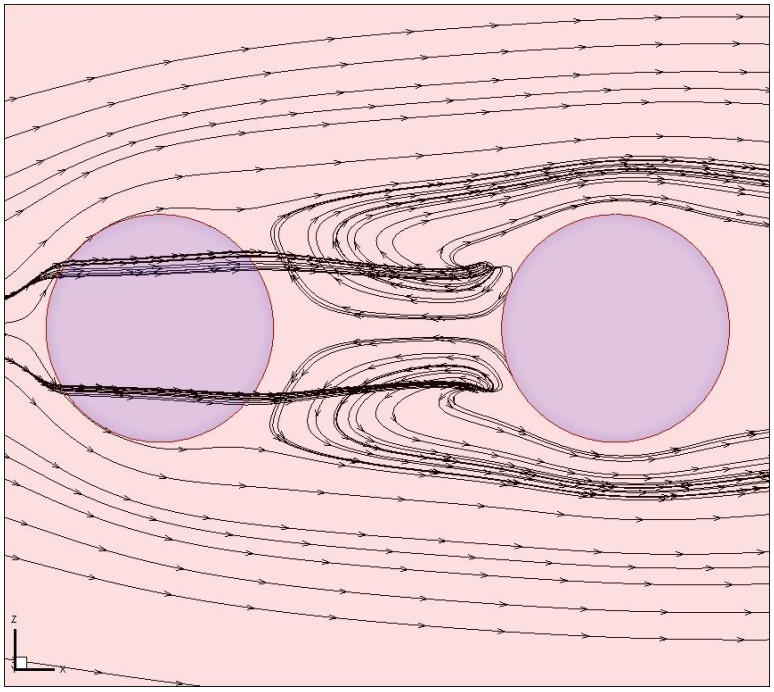

Figure 39: XZ view of flow over parallel cylinders at Re = 40, AR = 2, SeR = 2

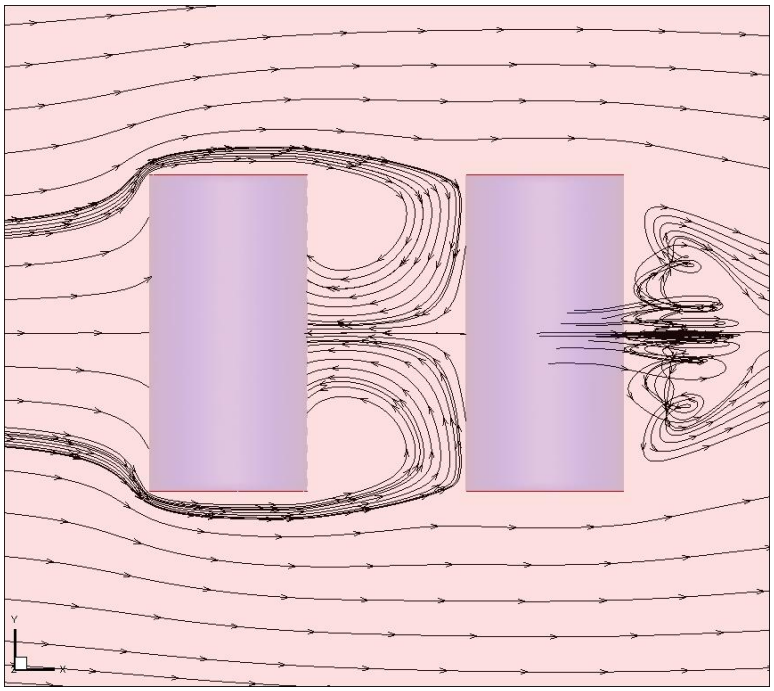

Figure 40: XY view of flow over parallel cylinders at Re = 40, AR = 2, SeR = 2

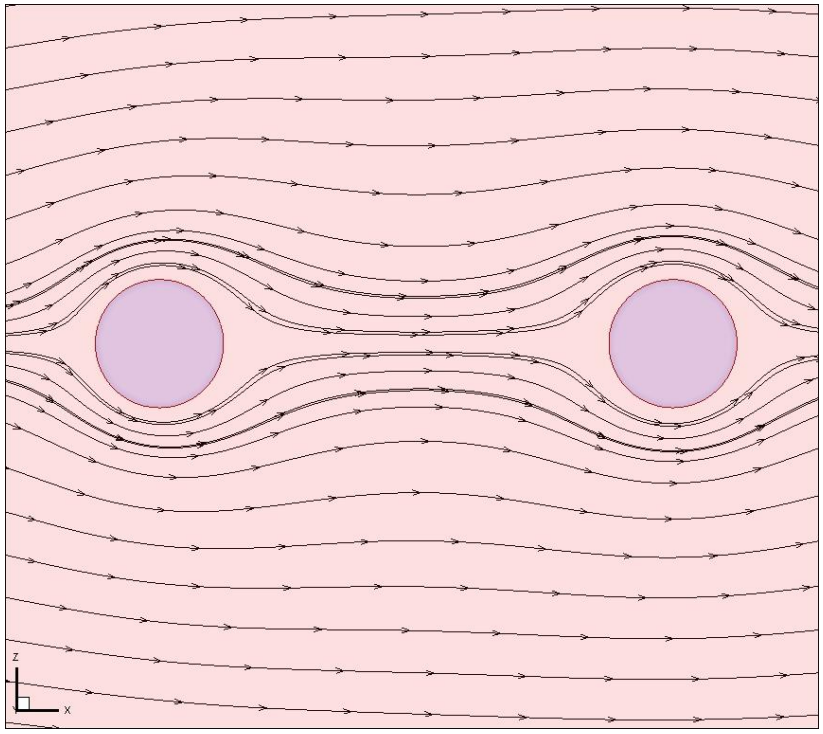

Figure 41: XZ view of flow over parallel cylinders at Re = 1, AR = 2, SeR = 5

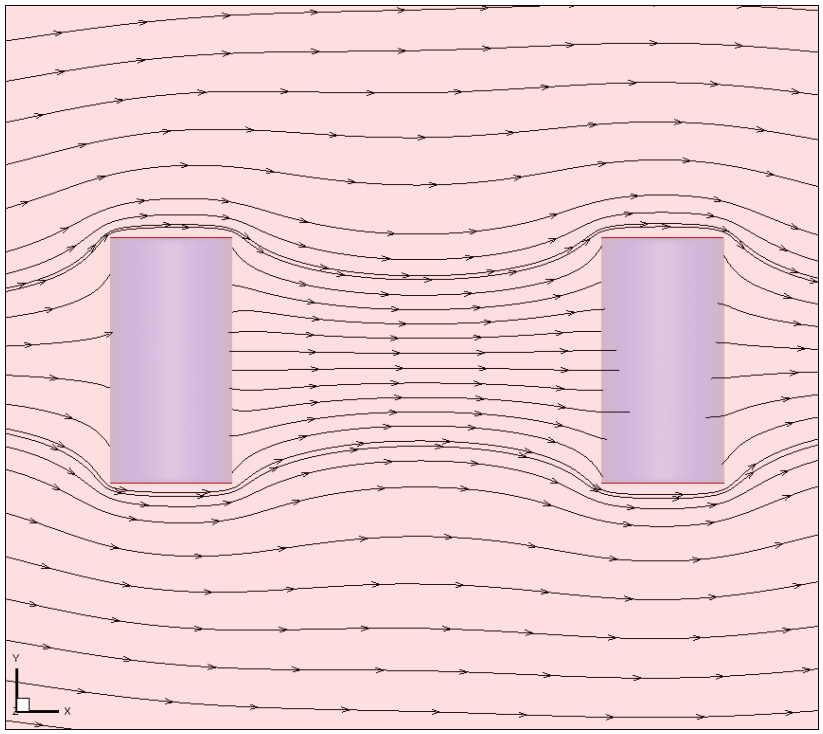

Figure 42: XY view of flow over parallel cylinders at Re = 1, AR = 2, SeR = 5

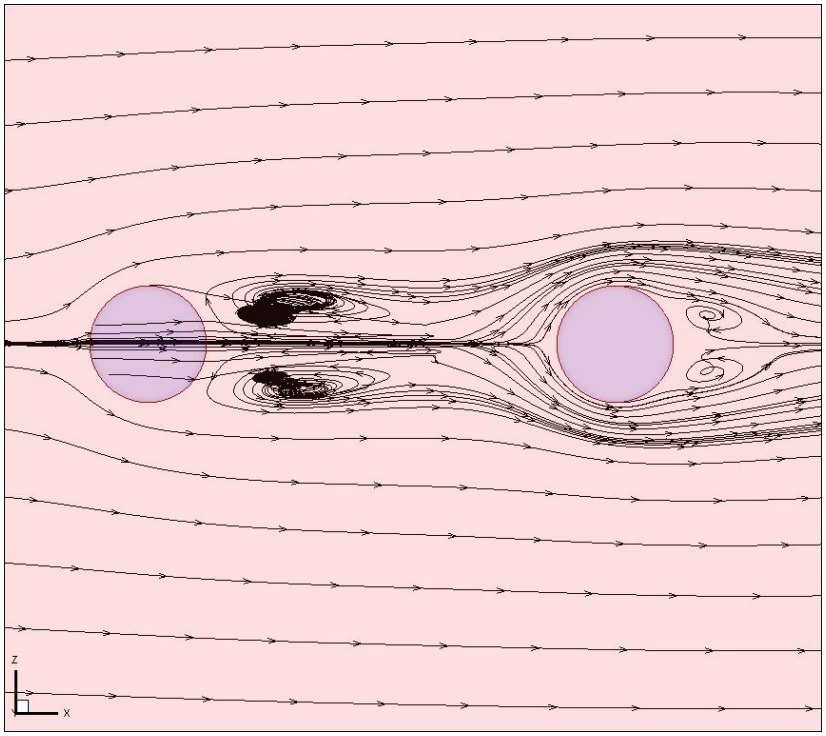

Figure 43: XZ view of flow over parallel cylinders at Re = 40, AR = 2, SeR = 5

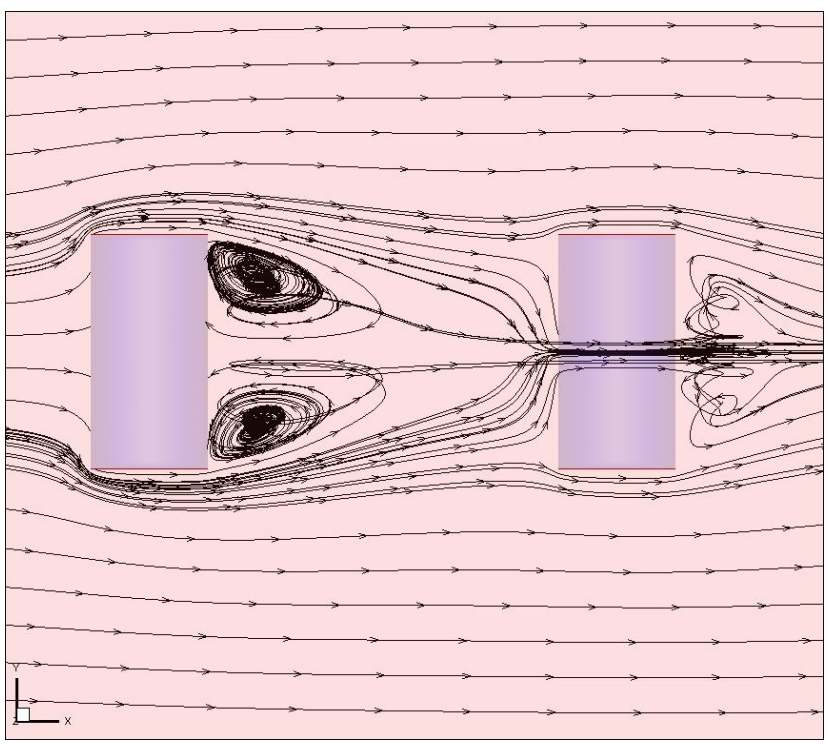

Figure 44: XY view of flow over parallel cylinders at Re = 40, AR = 2, SeR = 5

Streamline plots for cylinders of AR = 5 at SeR = 2 and SeR = 4 at Re = 1 and Re = 40 are shown in the following figures.

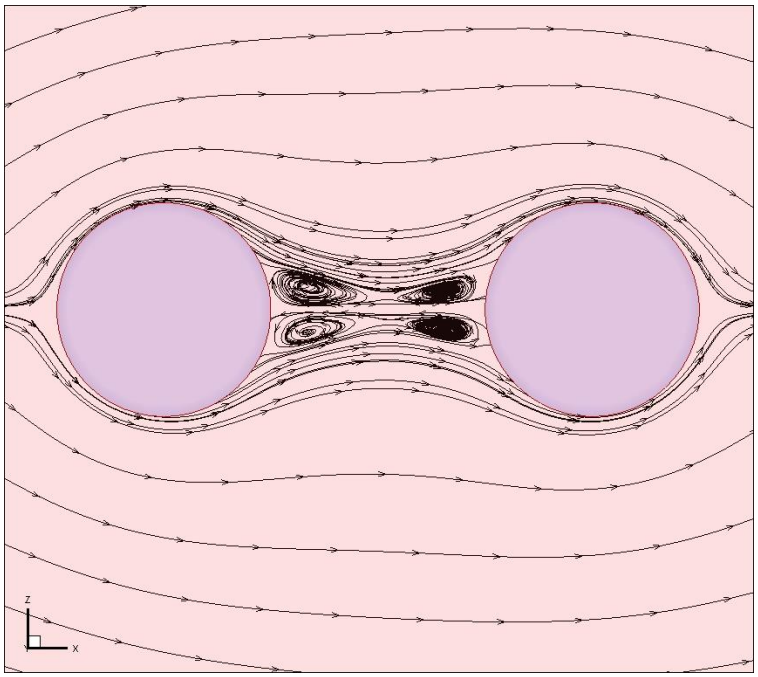

Figure 45: XZ view of flow over parallel cylinders at Re = 1, AR = 5, SeR = 2

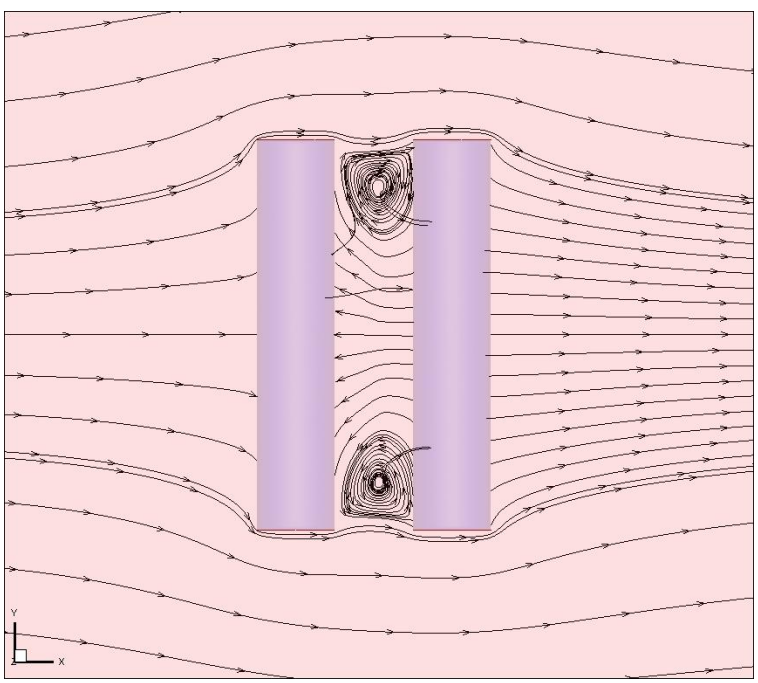

Figure 46: XY view of flow over parallel cylinders at Re = 1, AR = 5, SeR = 2

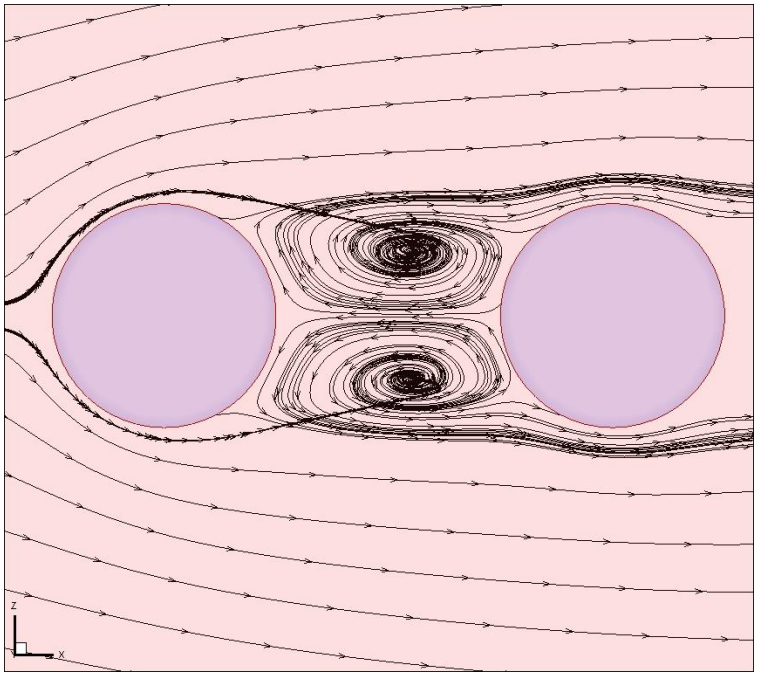

Figure 47: XZ view of flow over parallel cylinders at Re = 40, AR = 5, SeR = 2

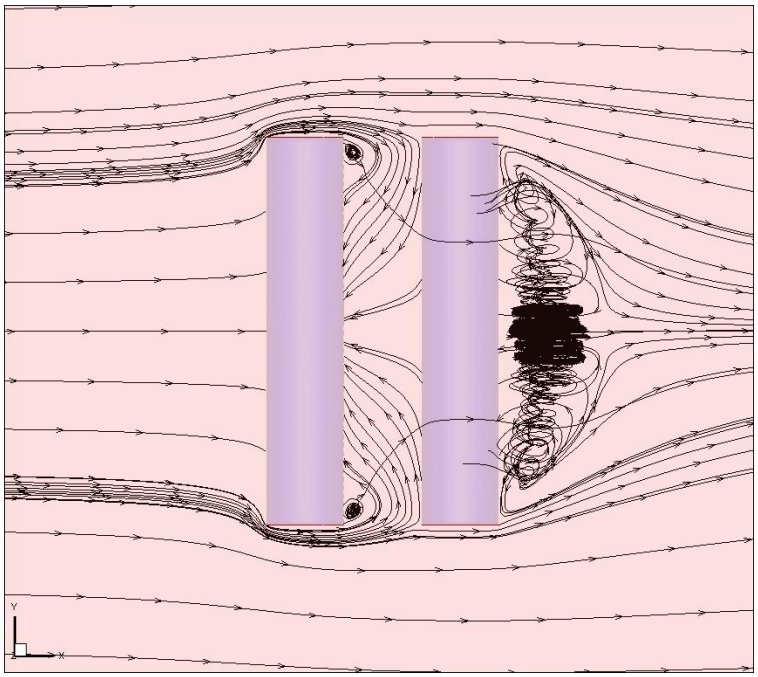

Figure 48: XY view of flow over parallel cylinders at Re = 40, AR = 5, SeR = 2

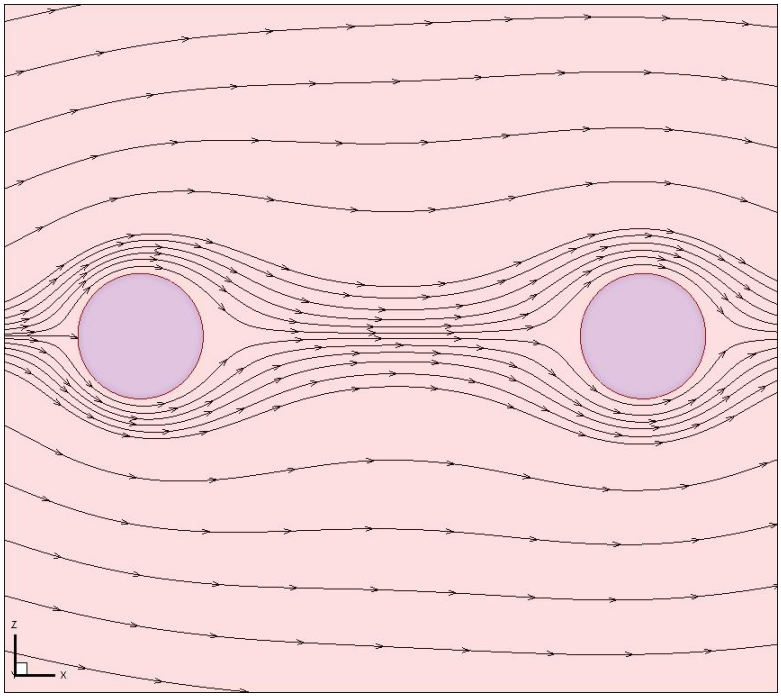

Figure 49: XZ view of flow over parallel cylinders at Re = 1, AR = 5, SeR = 5

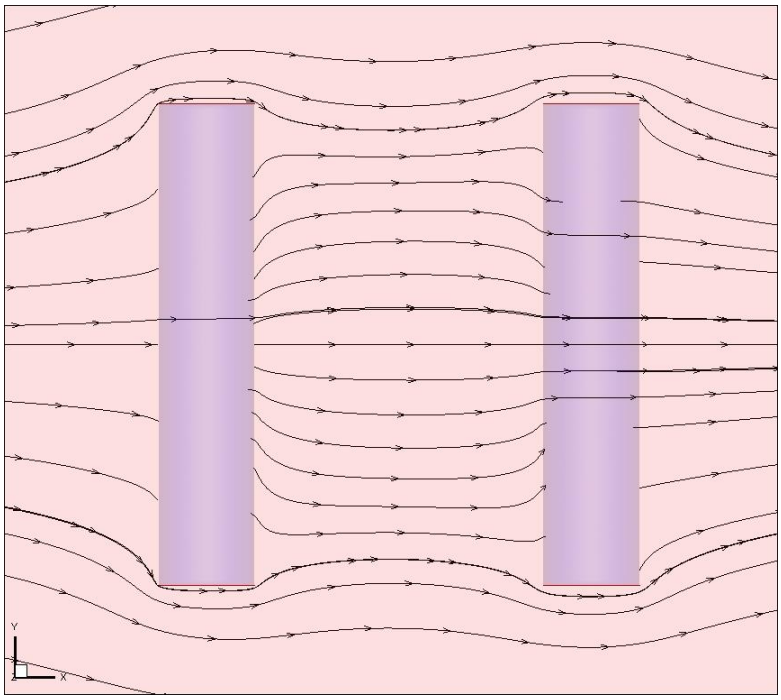

Figure 50: XY view of flow over parallel cylinders at Re = 1, AR = 5, SeR = 5

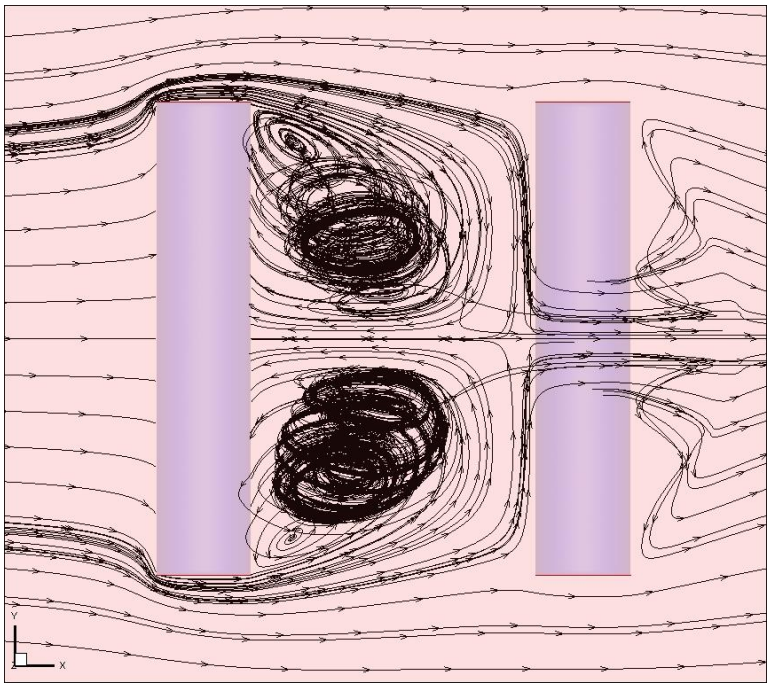

Figure 51: XZ view of flow over parallel cylinders at Re = 40, AR = 5, SeR = 5

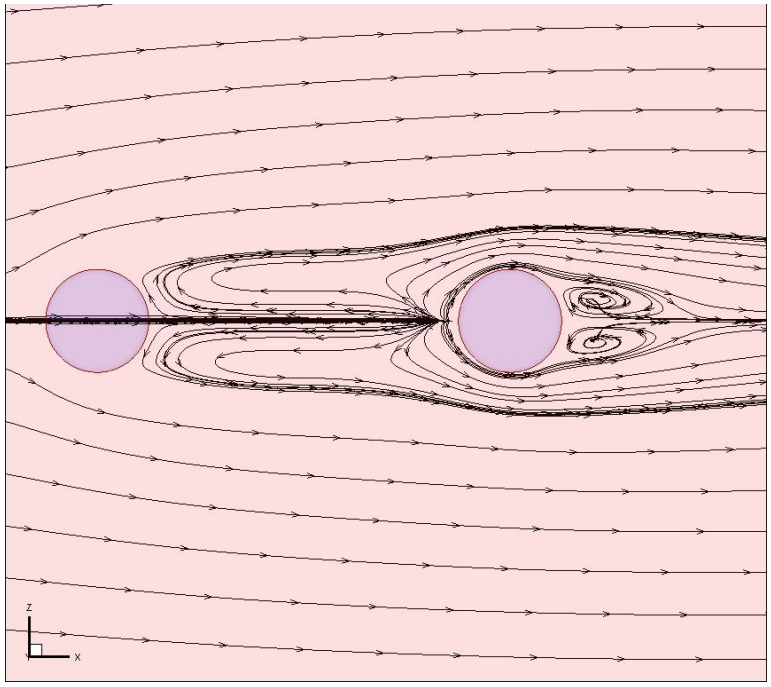

Figure 52: XY view of flow over parallel cylinders at Re = 40, AR = 5, SeR = 5

Streamline plots for cylinders of AR = 20 at SeR = 2 and SeR = 4 at Re = 1 and Re = 40 are shown in the following figures.

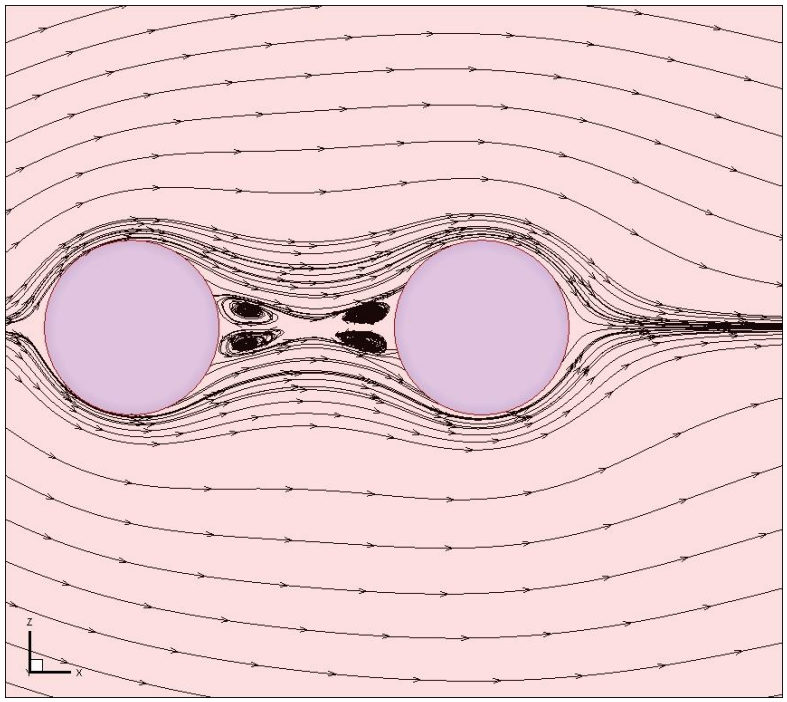

Figure 53: XZ view of flow over parallel cylinders at Re = 1, AR = 20, SeR = 2

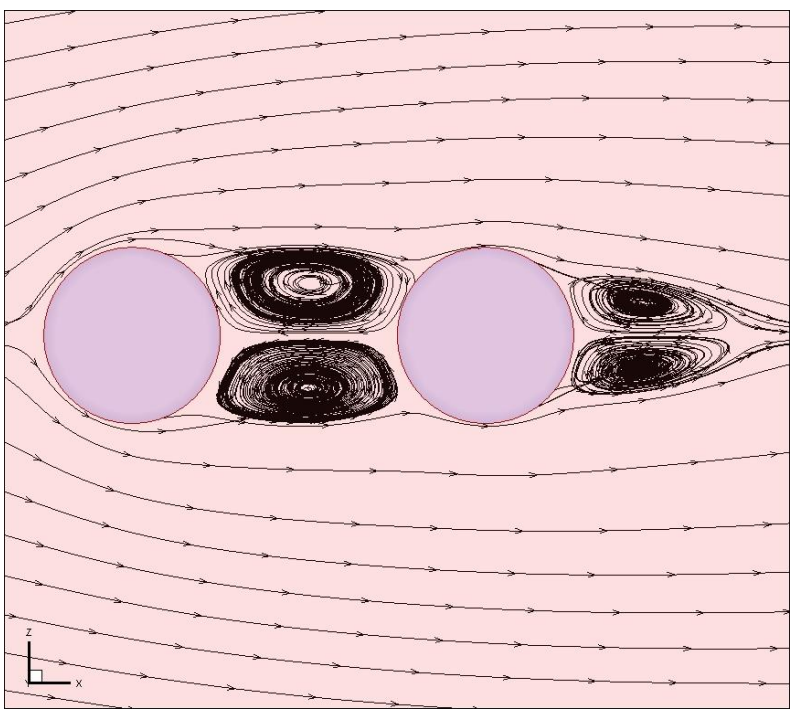

Figure 54: XZ view of flow over parallel cylinders at Re = 40, AR = 20, SeR = 2

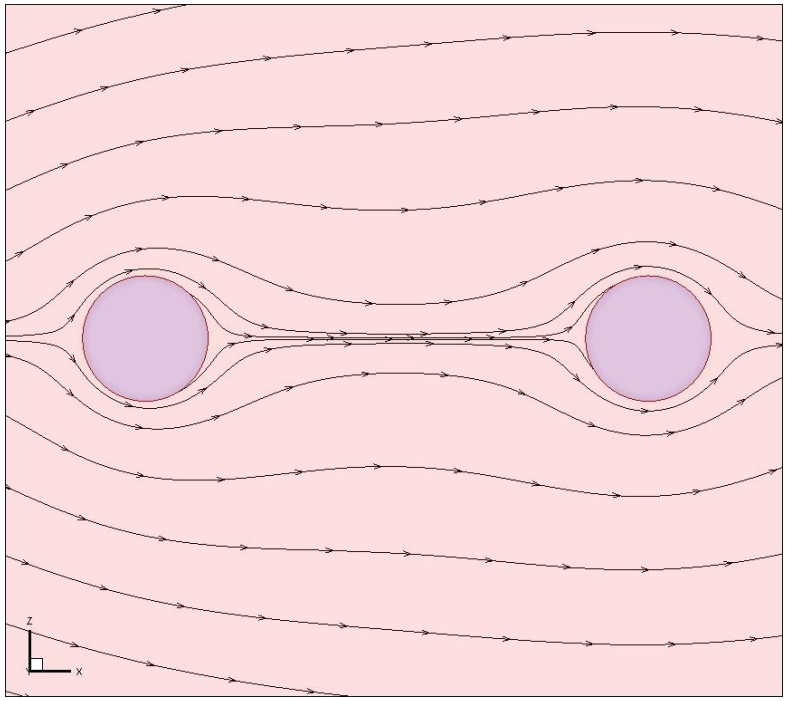

Figure 55: XZ view of flow over parallel cylinders at Re = 1, AR = 20, SeR = 5

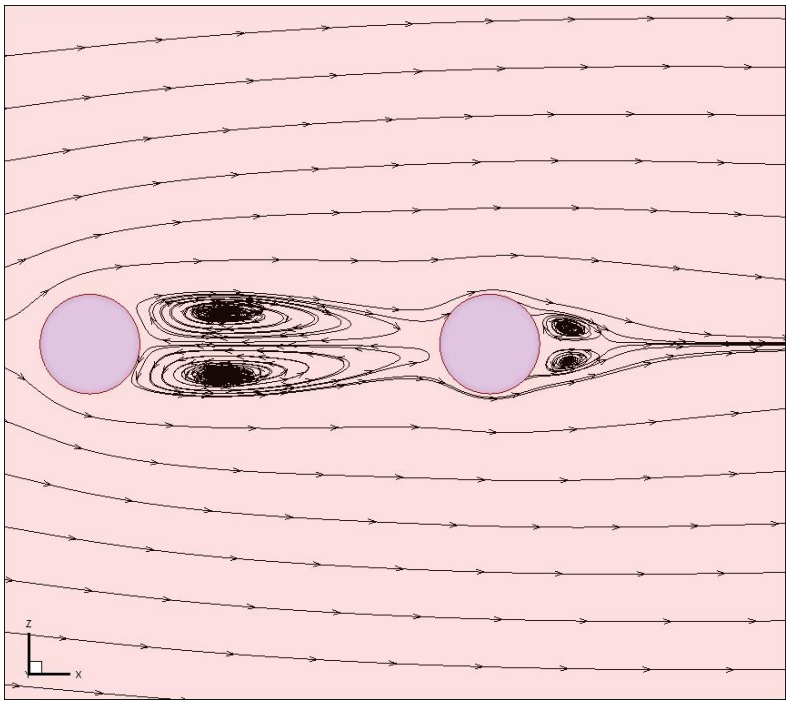

Figure 56: XZ view of flow over parallel cylinders at Re = 40, AR = 20, SeR = 5

Chapter 3 – Hydrodynamic interaction of skew cylinders in tandem arrangement

3.1 Introduction

As fluid flow in many applications may rapidly change in speed and direction, it is quite possible to observe changes in orientations of suspended particles in close proximity. These changes in orientations may have drastic effects on the dynamics of particles depending on their shapes. It may be said that for objects which have elongated shapes, for example, fiber suspensions, it is possible to have hydrodynamic torques and increased drag due to non-parallel alignment, which may significantly affect their motion.

3.2 Geometry and meshing

Flow around parallel cylinders in tandem arrangement was followed by a study in which the cylinders in tandem arrangement remained at some angle when viewed from the flow direction, that is, the axes of the cylinders were skew lines at angles which ranged from 5 to 90 degrees. The geometry is shown in Figure 57. As this angular difference could be as much as 90 degrees, the cross-section of the flow domain lost its high aspect ratio (W_y/W_z). The upstream and downstream lengths were kept the same as in the case of parallel cylinders but W_y = W_z = 110D. Figure 58 elucidates the angular difference from the upstream direction (or the negative x-direction).

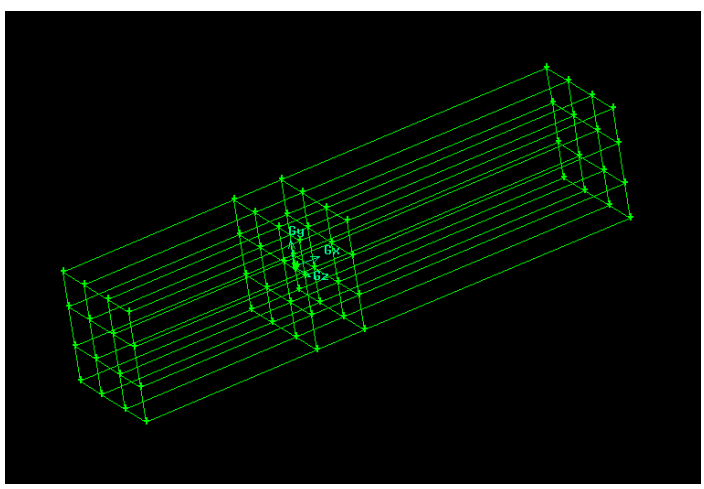

Figure 57: Domain partition for 3D flows around cylinders with skew axes

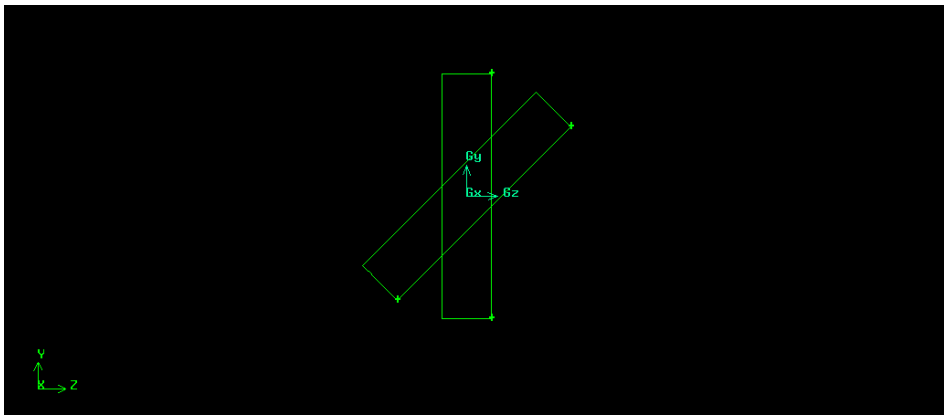

Figure 58: Angular separation between cylinder axes seen from the flow direction (X)

3.3 Domain-size and mesh independence

As these simulations have cylinders with non-parallel axes with angular separation between the cylinders ranging from 5 to 90 degrees, the Y and Z dimensions were equal unlike the case of parallel cylinders. Figure 59 and Figure 60 show the spatial variation of non-dimensional pressure and velocity magnitude in all directions. They all diminish to near zero.

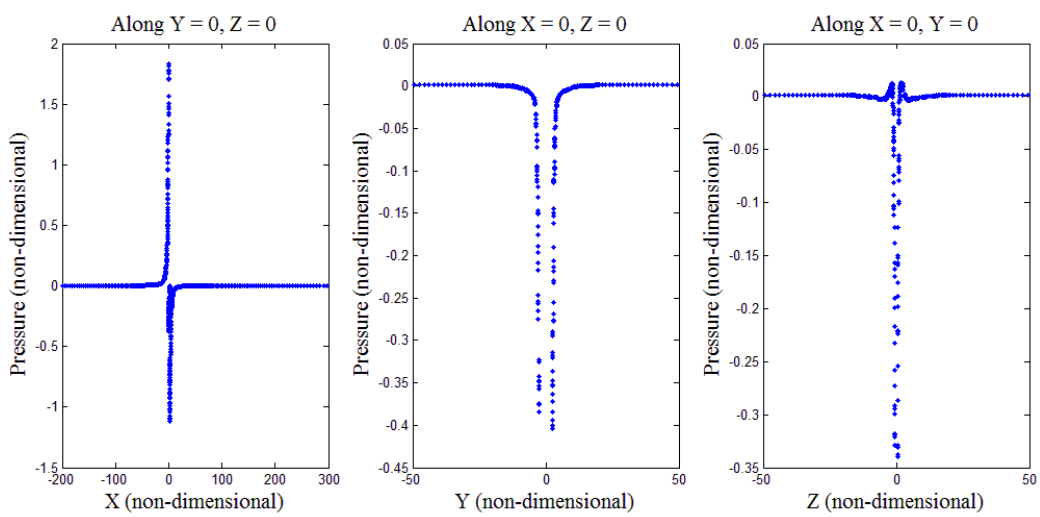

Figure 59: Pressure distribution in X, Y and Z directions

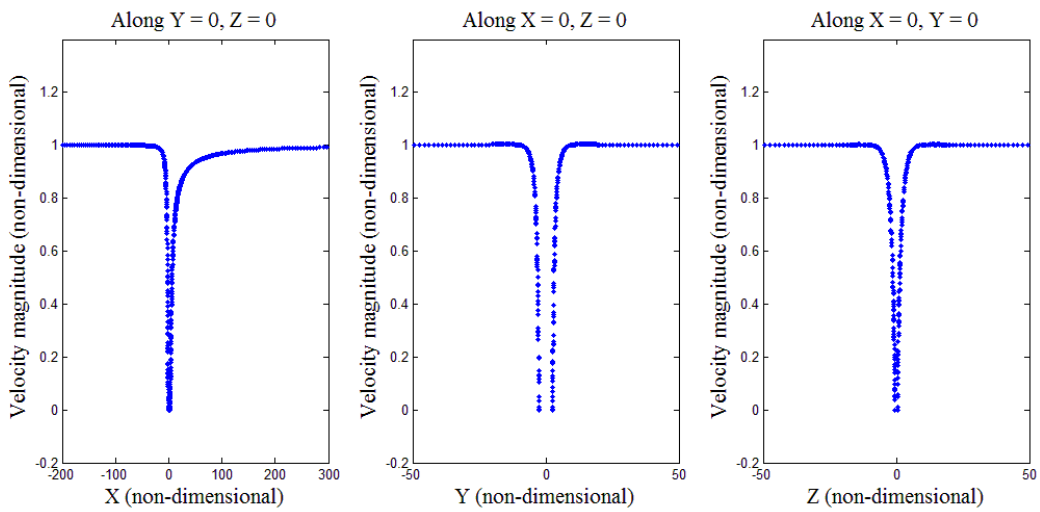

Figure 60: Velocity magnitude distribution in X, Y and Z directions

A mesh independence test was also carried out for cylinders of AR = 5 at 5 degrees angular separation at Re = 1. The results are plotted in Figure 61. Increasing the mesh element size from 2.2 million to 6.3 million resulted in 0.11% and 0.08% in drag coefficient of front and rear cylinders respectively. Hence a mesh size of about 2.2 million was used for all simulations in this category.

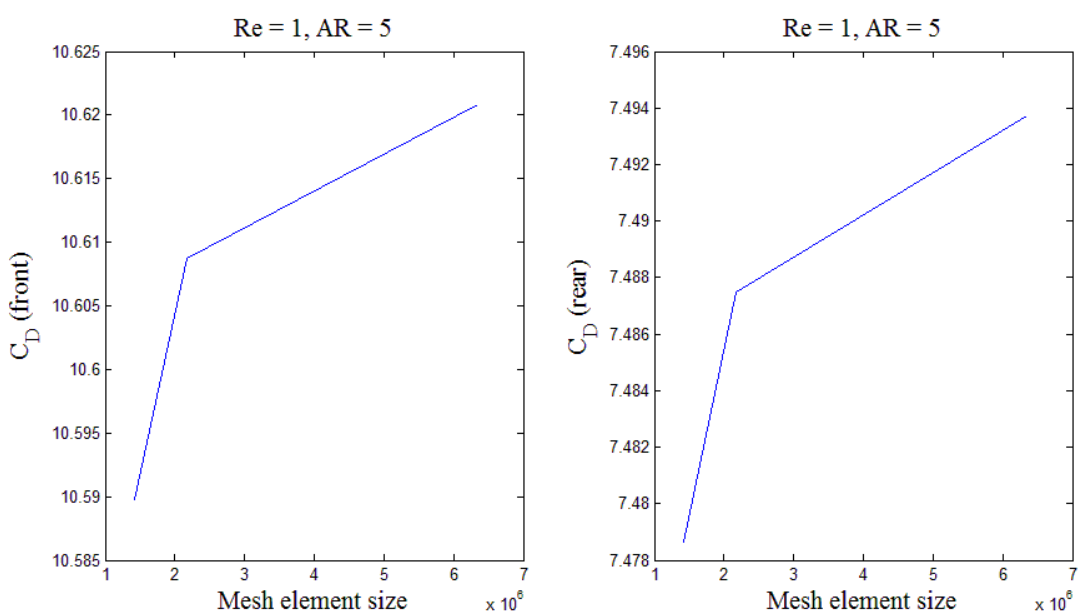

Figure 61: mesh independence test for three-dimensional flow over skew cylinders

3.4 Three-dimensional simulation results and discussion: skew cylinders

In this part the cylinders of AR = 5 were kept at SeR = 2,3 and 5 but their axes, though being always normal to the freestream, had an angular difference Θ_d when seen from the flow direction. This

study was carried out for $5 \leq \Theta_d \leq 90$ degrees. Due to this angular difference, both the front and rear cylinders experience torques. It is clear that Θ_d = 0 and Θ_d = 90 degrees correspond to symmetry and hence the hydrodynamic torques vanish. Figures show the effect on drag due to angular difference.

Figure 62 and Figure 63 show the effect of angular difference on drag force for both front and rear cylinders at *SeR* = 2 and *SeR* = 5. It is evident from the plots that the effect on front cylinders is much less than on rear cylinders. As expected, the effect of angular difference diminishes with separation. For Re>5 there is no significant change in drag coefficient for front cylinder. The maximum change observed for front cylinder was around 5% from zero angular difference to 90 degrees, at *SeR* = 2 and *Re* = 1.

Drag increases on the rear cylinder with increasing angular difference. At Re = 1, SeR = 2, the drag coefficient increases by 17% from 0 to 90 degrees whereas at Re = 40, drag coefficient is increased by about 2.7 times.

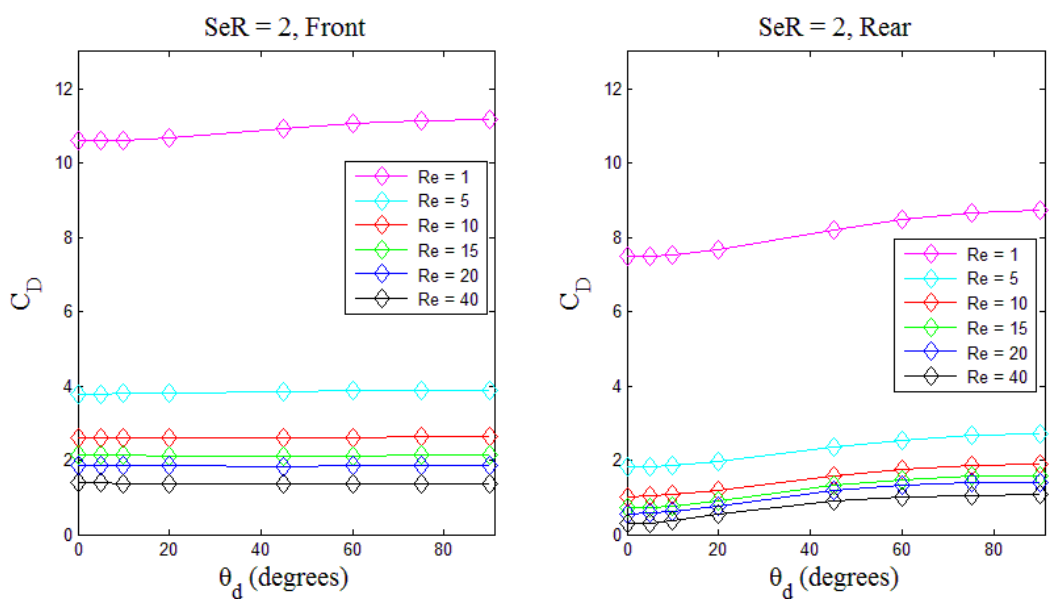

Figure 62: Drag coefficient distribution at SeR = 2 for all Re

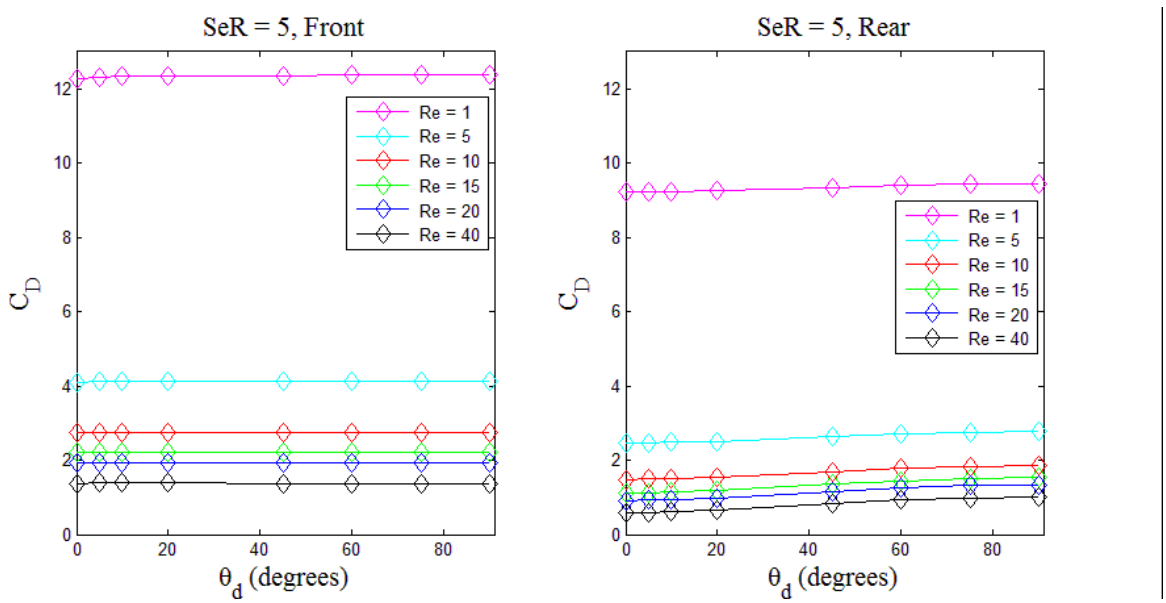

Figure 63: Drag coefficient distribution at SeR = 5 for all Re

The drag forces acting on the front and rear cylinders may be viewed from the ratio perspective. Figure 64 shows the ratio of drag force on the rear cylinder to that on front cylinder at each angle for all the Reynolds numbers and three different separation distances. The least and greatest variation in this ratio are seen for *Re* = 1 and *Re* = 40 for all separation ratios. Another observation that may be made is that except for *Re* = 1, the ratio trend at small angles (drag ratio decreases with increasing Reynolds number) gets reversed at large angular separations. Also this reversing of trend may be said to be taking place in the angular separation range of 40 – 45 degrees approximately. At *Re* =1, there is flow separation and a wake region exists between the cylinders when they are close to being parallel but at higher angular separation, this wake region is reduced to a very small region (between the cylinders, near their centroids) and flow is attached to a great extent, which may be the reason why behavior at low *Re* is significantly different from that at higher *Re*.

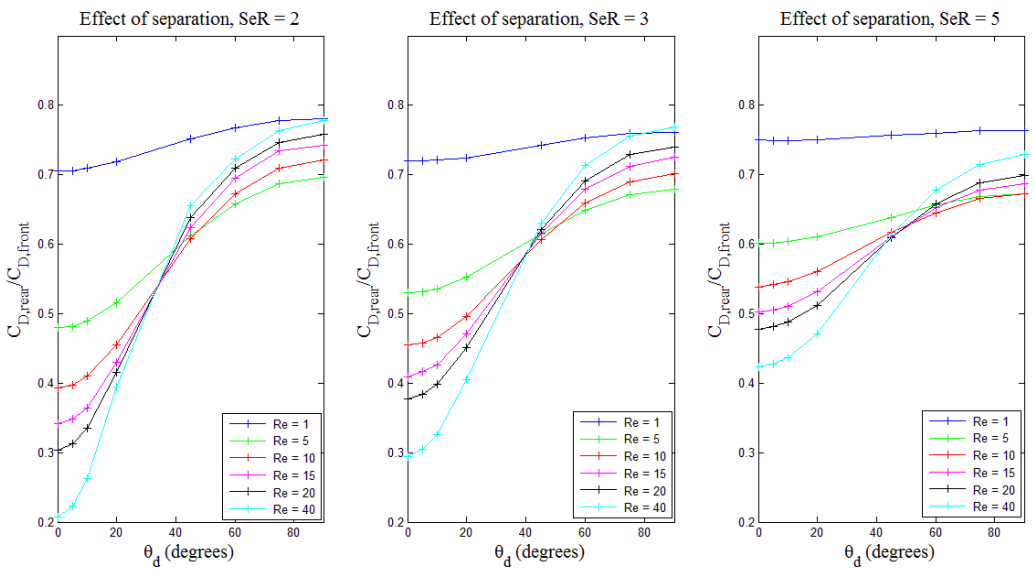

Figure 64: Effect of angular separation on ratio of drag on rear cylinder to drag on front cylinder for all Re

Figure 65 and Figure 66 give information about the moments acting on the cylinders and how they vary in the complete angle range. Here also it is noticed that the moments diminish with increasing separation. Except at *SeR* = 2, *Re* = 40, the moments on both cylinders have the same sign, and thus if allowed to rotate, both cylinders would tend to rotate in the same direction. In order to get an idea of how the angular separation between the cylinders will change initially, the difference between the moments of front and rear cylinders was plotted at all *Re* and *SeR* = 2 and *SeR* = 5 and the result is shown in Figure 67. It shows that except at small separation and Re<15, where the angular separation tends to increase between the cylinders, at all other situations the cylinders have a tendency to get aligned.

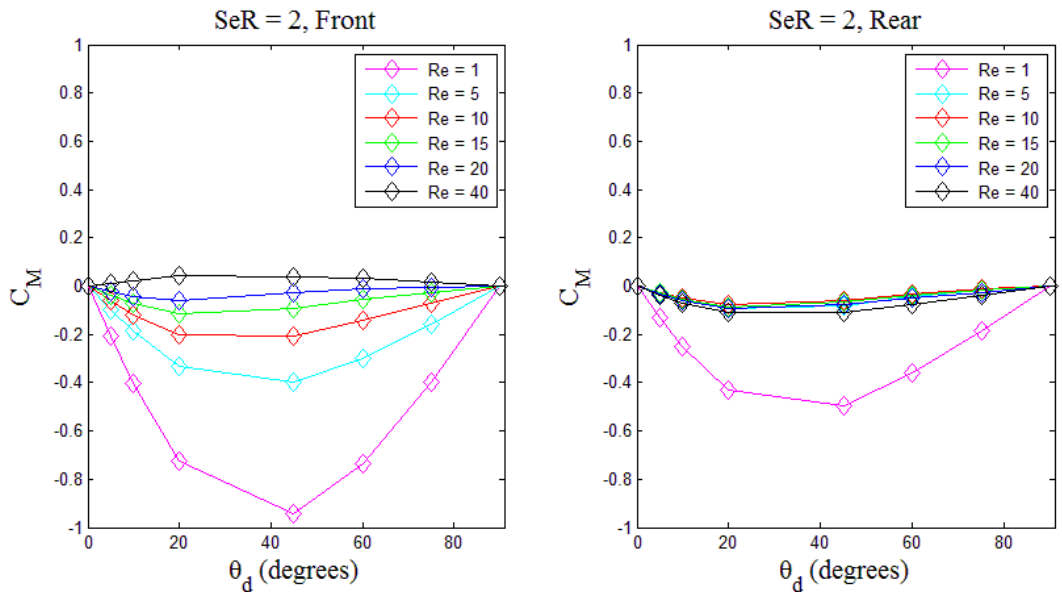

Figure 65: Moment coefficient distribution at SeR = 2 for all Re

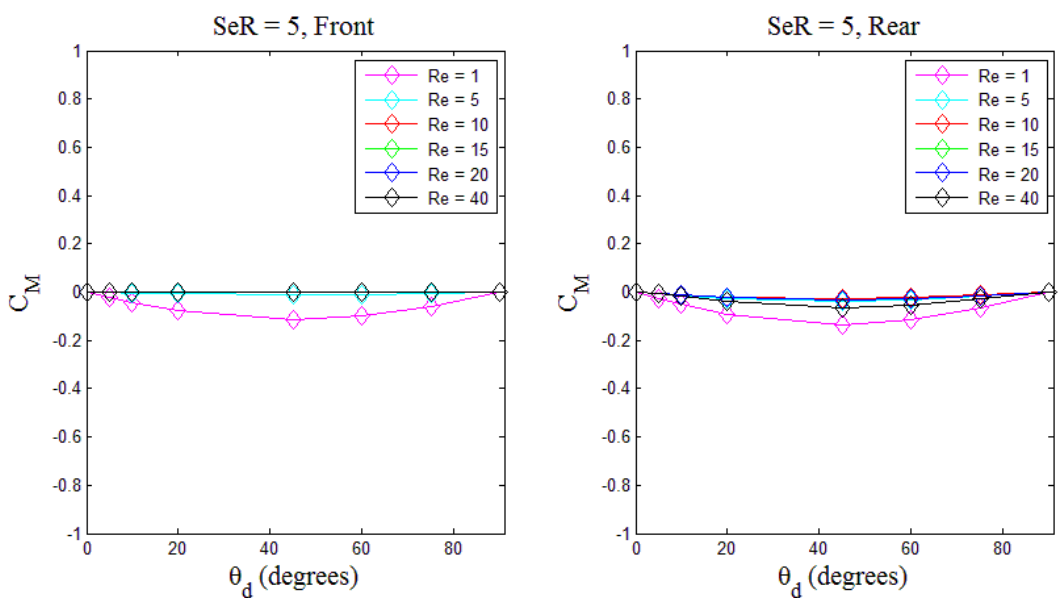

Figure 66: Moment coefficient distribution at SeR = 5 for all Re

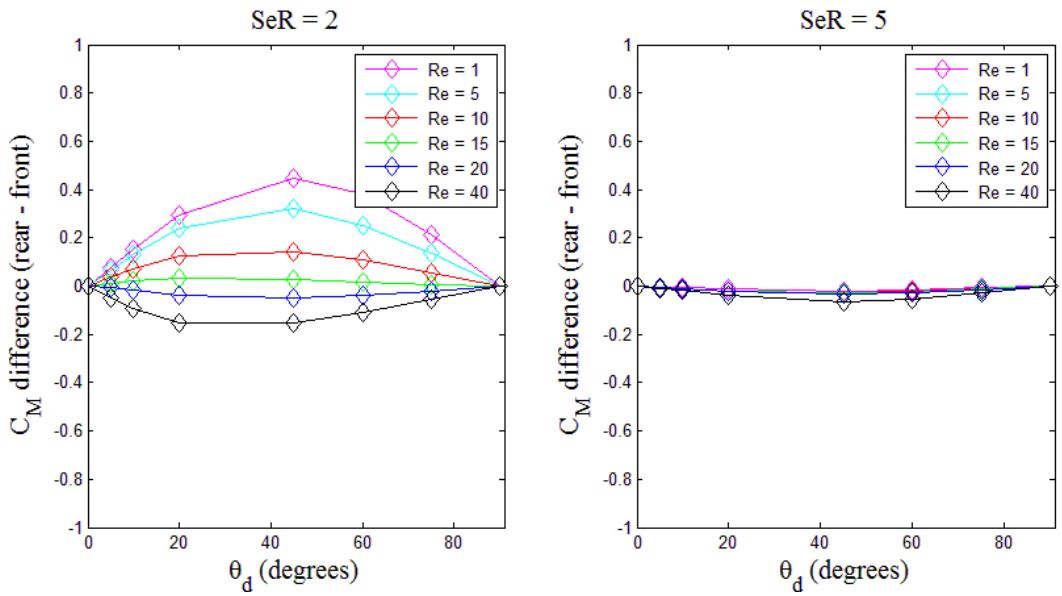

Figure 67: Moment coefficient difference distribution at SeR = 2 and SeR = 5 for all Re

The following figures show streamline plots at *Re* = 1 and *Re* = 40, *SeR* = 2 and angular separation of 5 degrees. It can be seen that at *Re* = 1 the wake structure seen earlier in the case of parallel cylinders at *Re* = 1 and *SeR* = 2 is no longer seen to exist probably because of the highly three-dimensional nature of the flow. At *Re* = 40, the wakes behind the rear cylinder is shorter in length than that seen in the case of parallel cylinders. A view from the Y-direction at a slightly off-centre location (Y = 0.2*D*), it can be seen that the flow at both *Re* = 1 and *Re* = 40 are asymmetric with strong recirculating wakes forming at *Re* = 40.

Streamline plots are shown in the following figures at angular separations 5, 45 and 90 degrees at *Re* = 1 and *Re* = 40. The flow streamlines are highly three-dimensional due to non-parallel alignments of the cylinders. At low *Re*, the flow is attached and at high *Re*, the three-dimensional wake forming behind the rear cylinder is of smaller size compared to those forming in the case of parallel cylinders.

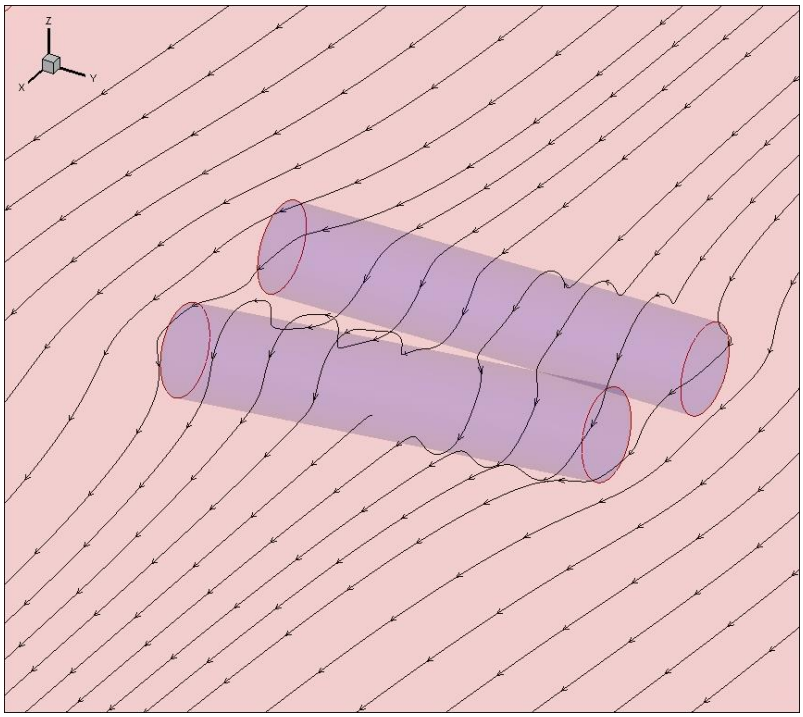

Figure 68: Isometric view of cylinders with angular separation = 5 degrees, Re = 1

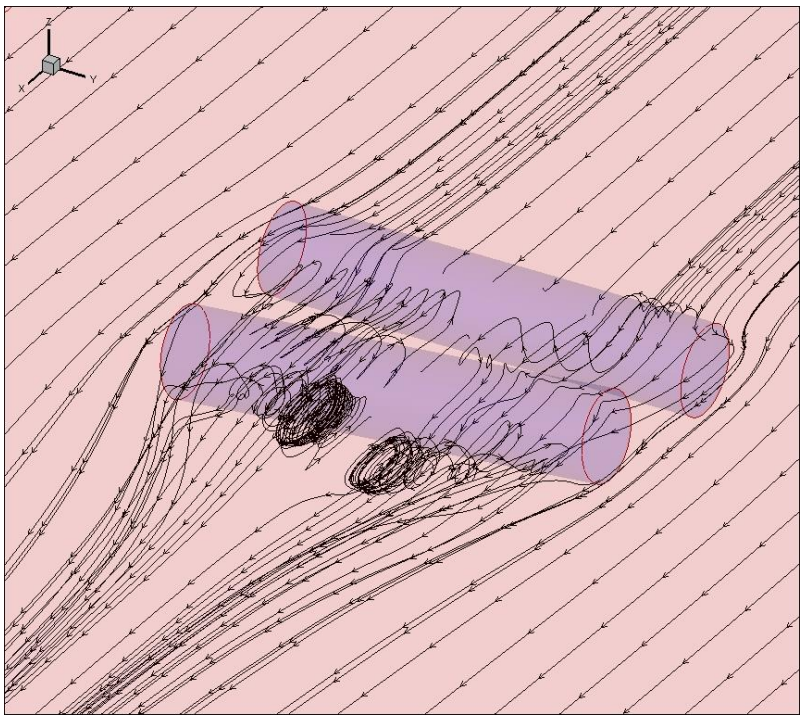

Figure 69: Isometric view of cylinders with angular separation = 5 degrees, Re = 40

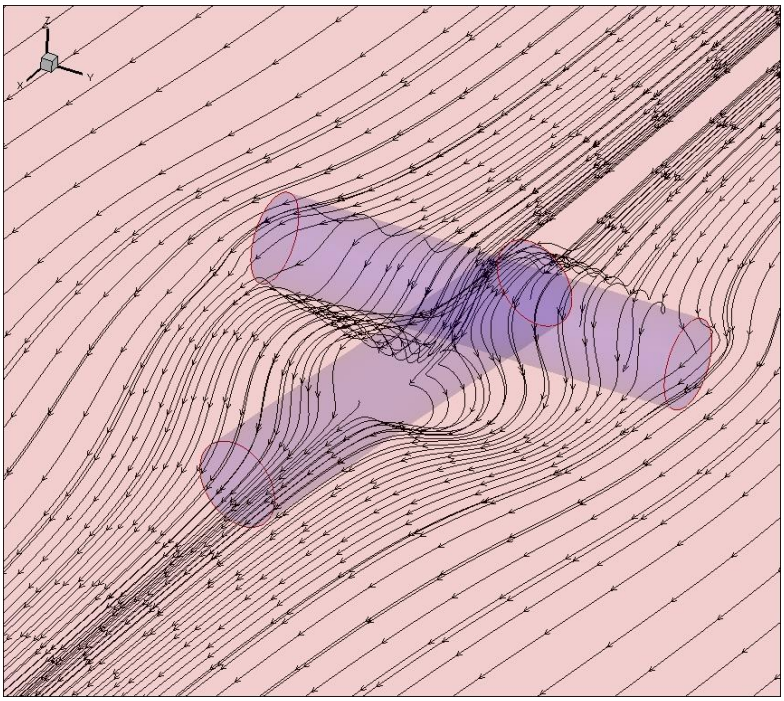

Figure 70: Isometric view of cylinders with angular separation = 45 degrees, Re = 1

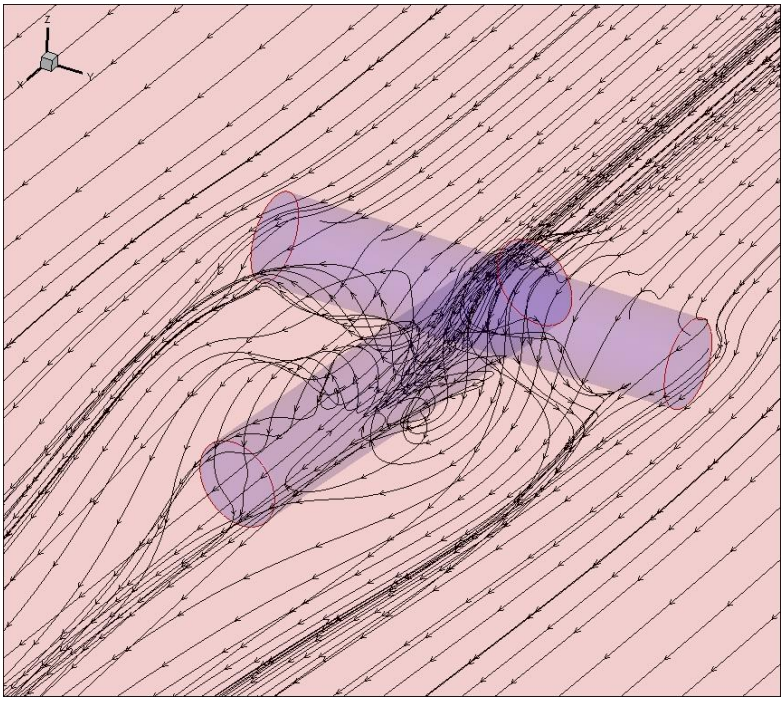

Figure 71: Isometric view of cylinders with angular separation = 45 degrees, Re = 40

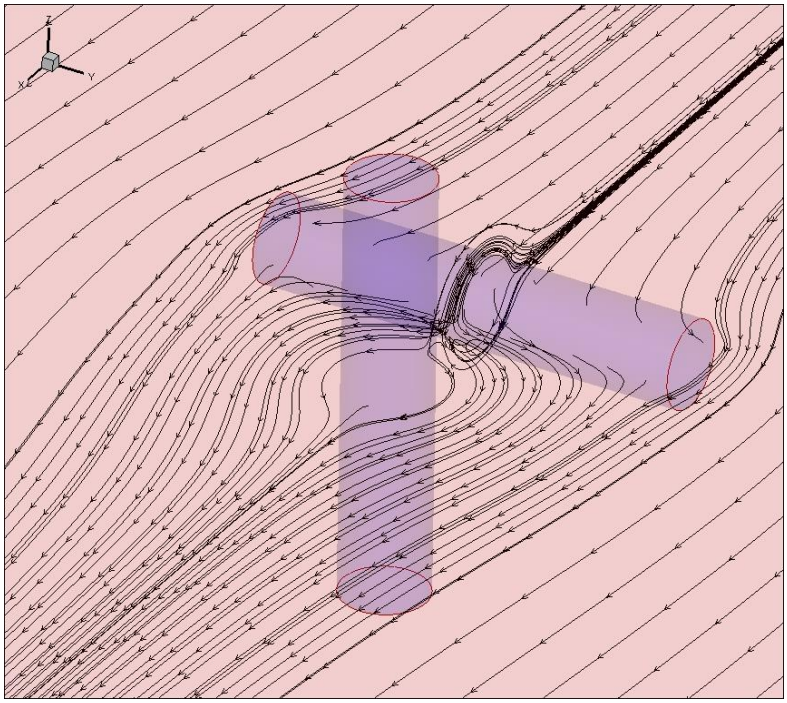

Figure 72: Isometric view of cylinders with angular separation = 90 degrees, Re = 1

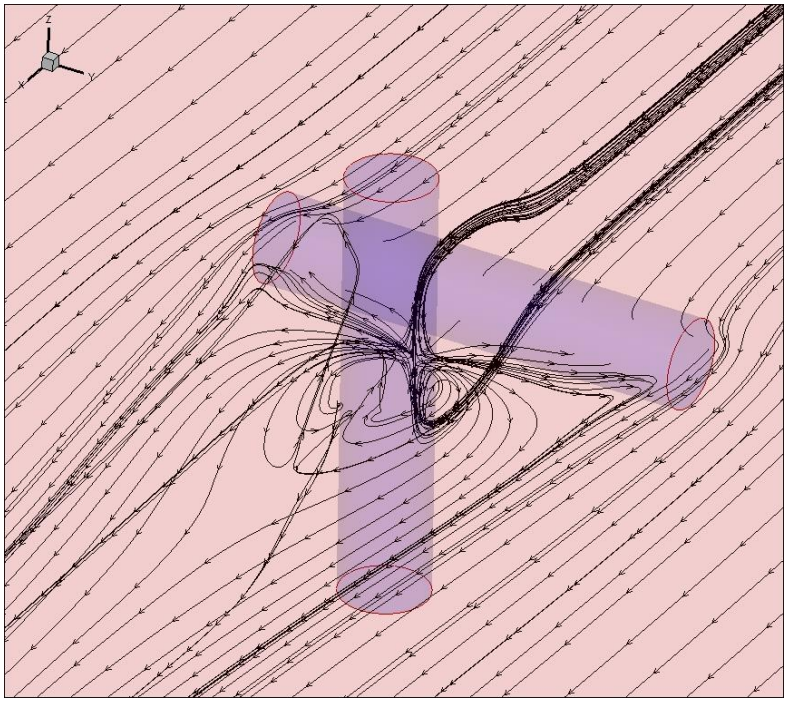

Figure 73: Isometric view of cylinders with angular separation = 90 degrees, Re = 40

Chapter 4 – Rotational motion of cylinders due to hydrodynamic moments

4.1 Introduction

After simulating the effect of angular separations between axes of cylinders in proximity, it was important to verify the results of the steady state analyses with unsteady flow simulations. Here transient rotation of an isolated cylinder (AR = 5) and two cylinders in proximity were studied at Re = 1 and Re = 40.

4.2 Geometry and meshing

For the unsteady 3D simulations, meshing involved the addition of sliding mesh interfaces. The central box region which contains the cylinder(s) was further subdivided into regions in a way that each cylinder was inside a spherical or cylindrical region which would rotate with the cylinder and thus had a mesh interface with the non-moving remainder of the central box.

For unsteady simulations of flow over a cylinder initially at an angle of 45 degrees to the flow direction, the partitioned central box is shown in Figure 74. The cylinder is inside a sphere and it is at the boundary of this sphere that there exists an interface. The meshing done inside this sphere rotates with the cylinder as it rotates due to hydrodynamic moment acting on it.

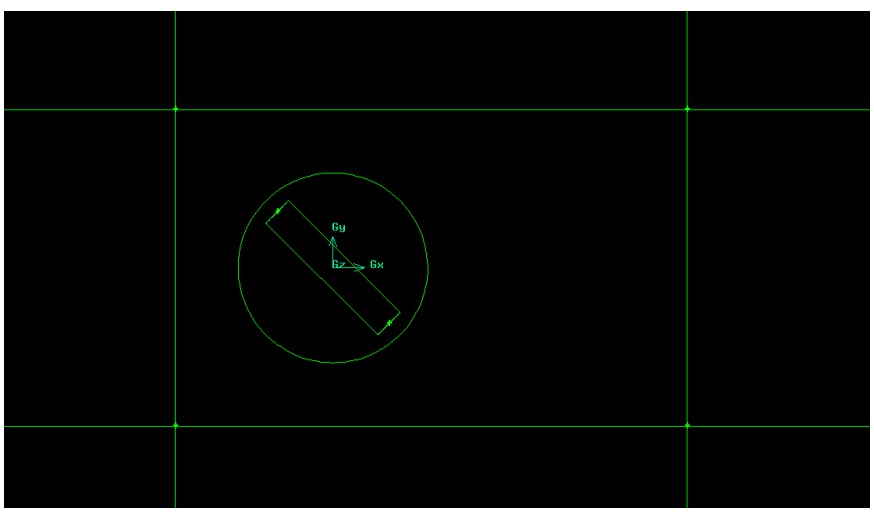

Figure 74: Domain partition for making mesh interfaces

In the case of two cylinders, which are very closely located (S = 2D), this kind of "spherical-mesh" envelope is not possible, so they were placed inside different cylinders as shown in Figure 75, Figure 76 and Figure 77.

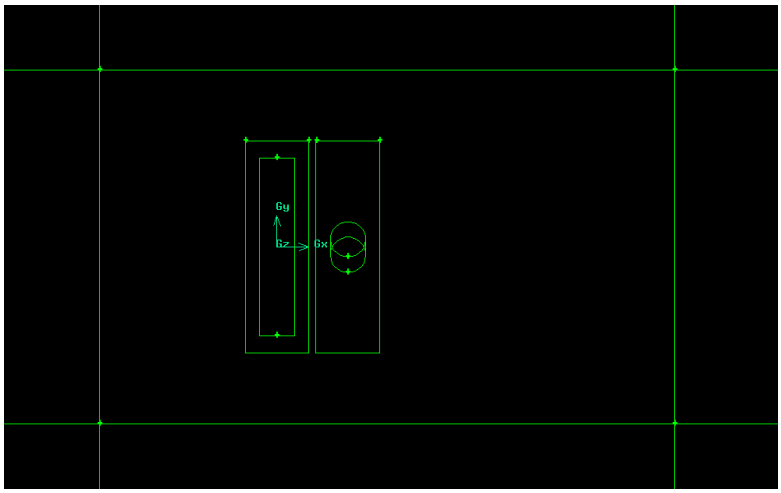

Figure 75: Skew cylinders inside separate regions boundaries of which form mesh interfaces

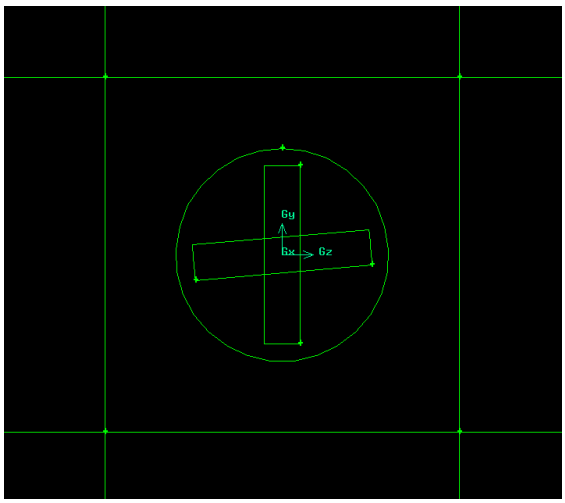

Figure 76: Angular separation between axes of front and rear cylinders seen from the flow direction (X)

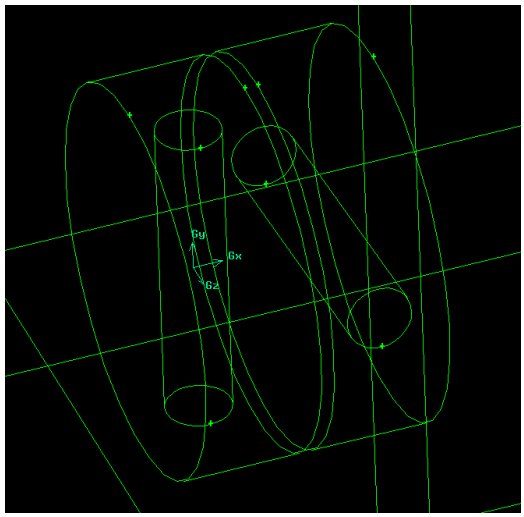

Figure 77: An oblique view of skew cylinders inside separate cylindrical regions boundaries of which form mesh interfaces

4.3 Domain-size and mesh independence

For the unsteady simulations, the mesh was prepared separately with further reduction in cross-sectional dimensions. Pressure and velocity-magnitude plots are shown in Figure 78 and Figure 79 which show zero-slope at the ends of the domain.

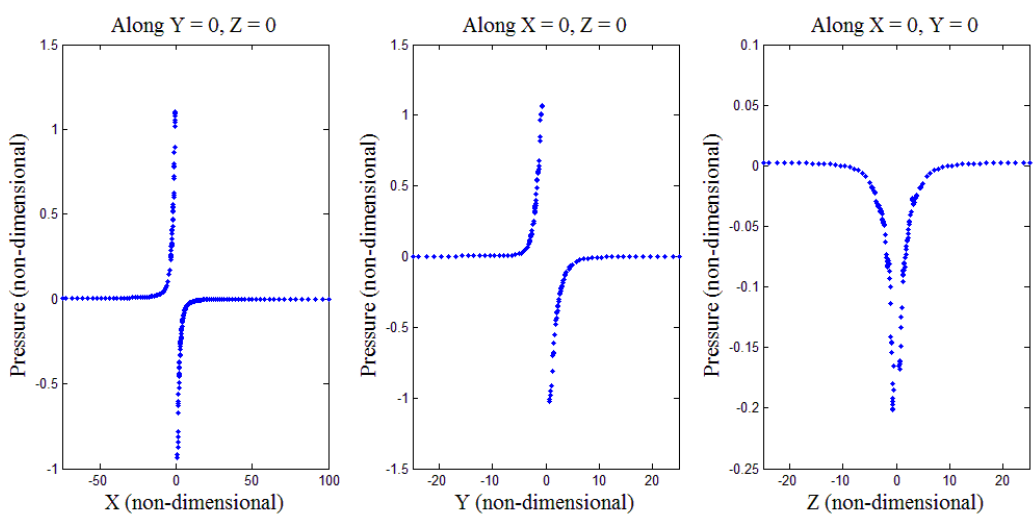

Figure 78: Pressure distribution in X, Y and Z directions

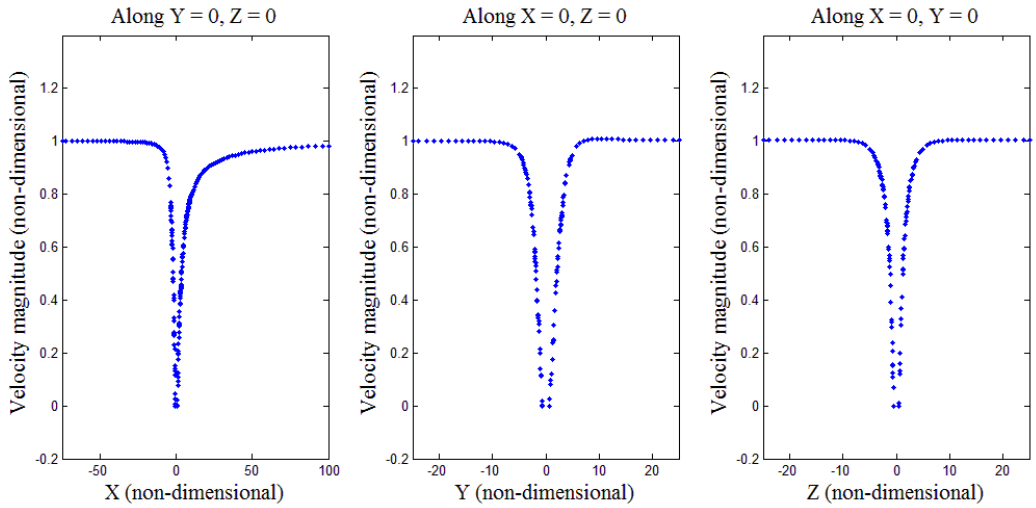

Figure 79: Velocity magnitude distribution in X, Y and Z directions

4.4 Unsteady simulations results and discussion

4.4.1 Single cylinder at an initial angle of 45 degrees to freestream

Vakil *et al.* 2009 threw some light on lift and drag forces experienced by a cylinder ($2 \leq AR \leq 20$) in a steady flow with its axis at different angles with respect to the freestream for $1 \leq Re \leq 40$. Here, a cylinder of AR = 5 was chosen and kept at 45 degrees to freestream. At both Re = 1 and Re = 40, taking the steady state solution for fixed cylinders as initial condition, unsteady flow analysis was carried out in order to determine the rotational motion tendency of the cylinder. The translation of the cylinder was blocked by writing a User-Defined Function (UDF) file in Fluent. The 6-DOF solver in Fluent was employed to solve for the motion of the cylinder.

The method employed in the study was validated by analyzing the rotational motion of a sphere in a shear flow. Jeffery, 1922 states that for an ellipsoid given by,

$$\frac{x^2}{\alpha^2} + \frac{y^2}{\beta^2} + \frac{z^2}{\gamma^2} = 1,$$

which has the *xyz* co-ordinate system attached to it, and is subjected to a shear flow in a global co-ordinate system *x'y'z'* such that *x* = *x'* and *yz* plane is related to *y'z'* by an angle ϕ, the rotation may be given as,

$$\tan\phi = \frac{\beta}{\gamma}\tan\frac{\beta\gamma\kappa t}{\beta^2+\gamma^2}$$

where κ is the shear strain rate. A sphere may be said to be an ellipsoid with α = β = γ. And hence for a sphere the above rotational equation may be simplified to $\phi = \kappa t/2$

or $\frac{d\phi}{dt} = \kappa/2$. For validation, a sphere was kept inside a channel of width 1 unit and the top and bottom walls were given tangential wall velocities of 5 and -5 units which meant a shear rate of 10 units. Hence according to the above theory expected angular velocity would be 5 radians/unit-time.

Three validation cases were started for different time steps and different weights of the sphere. A steady state solution was first obtained for a non-moving sphere and the solution was used as an initial condition for the unsteady cases. For very low weights of the sphere (density ~ surrounding fluid), the initial angular acceleration of sphere is sufficiently high to require a very small time step. Hence heavy spheres, as heavy as 10^3 to 10^4 times the surrounding fluid was used. Two different time-steps Δt = 0.001 and Δt = 0.0005 were used. Figure 80 shows a comparison for the two time-steps. It may be said that the time-steps chosen produced reliable results. The L2-relative error norm was 0.0022. It also shows that after a brief transient the solution reaches a steady angular velocity as expected from Jeffery's formulation.

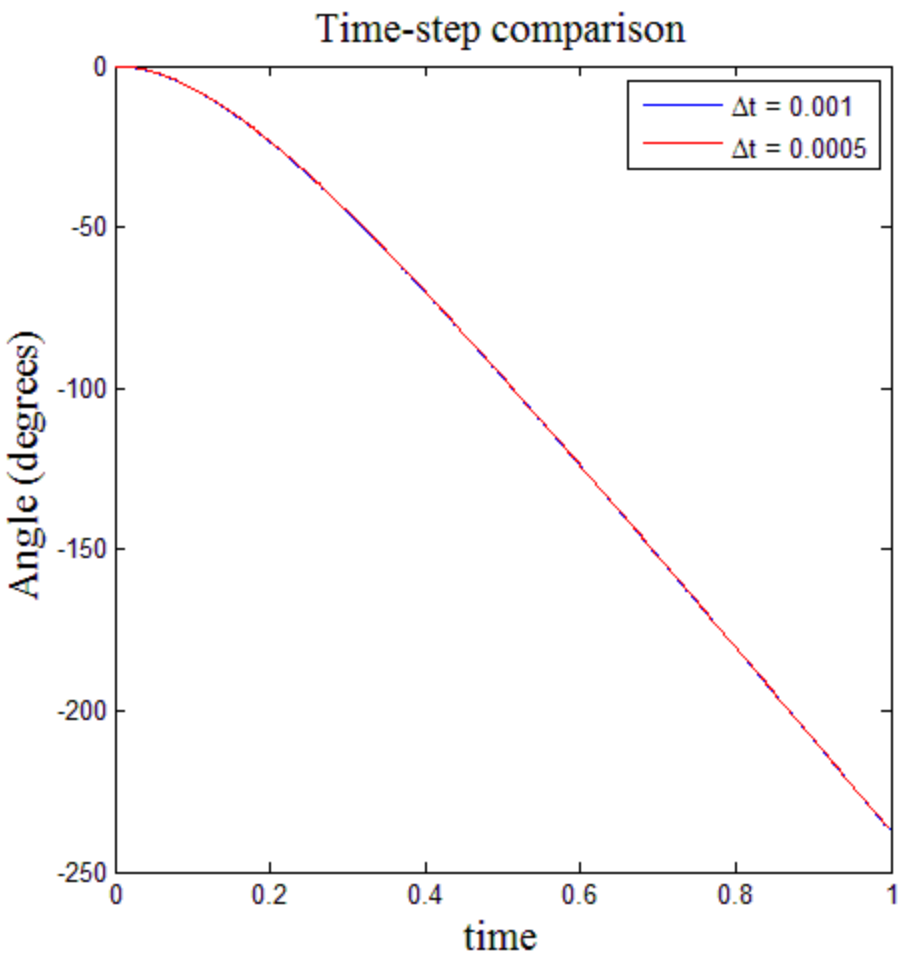

Figure 80: Angle vs. time for two different time-steps

The rotation angle with respect to time for spheres of two different densities has been shown in Figure 81. Though the simulation for the heavier sphere was discontinued, it may be said that it is tending towards acquiring the same angular velocity. An asymptotic trend for the angular velocity of the heavier sphere towards the constant angular velocity already acquired by the lighter sphere is seen.

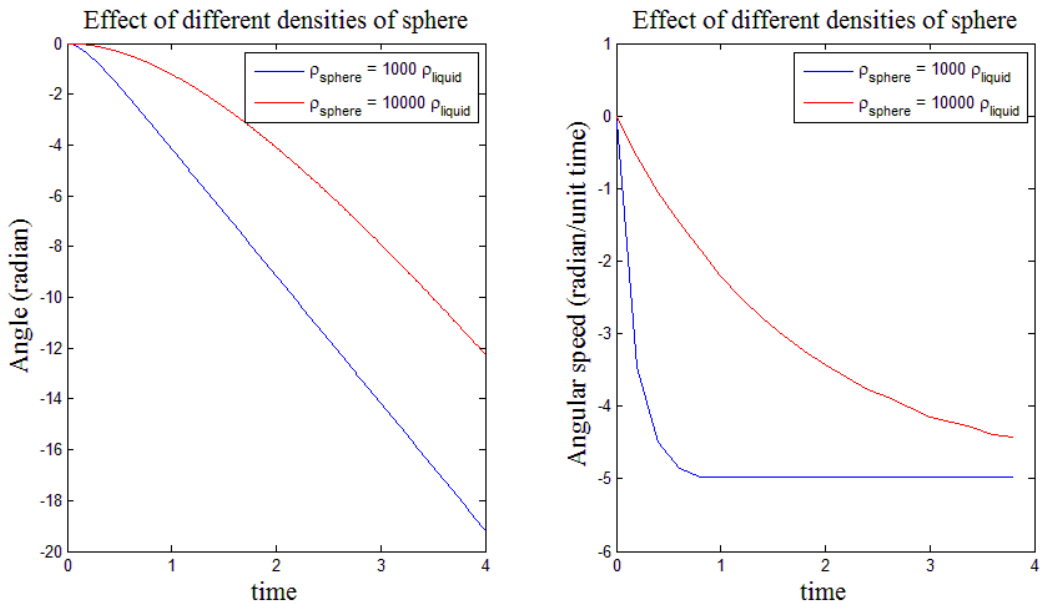

Figure 81: Angular position and angular velocity of spheres with different densities

A calculation shows that the constant angular velocity obtained by the lighter sphere is 5 radians/unit-time, which is in agreement with theoretical formulation.

The simulations with the cylinders (AR = 5) were carried out for Re = 1 and Re = 40. The simulation for the higher Re was carried out for three different time-steps to reconfirm proper time-stepping. Figure 82 shows the cylinder's rotation behavior with respect to time. Once again, it may be said that results for different time-steps are in good agreement. The cylinder's rotation at Re = 1 is shown in Figure 83. Viscous effects are dominant at low Re and the cylinder rotates to asymptotically reach an orientation in which its axis is at 90 degrees to the freestream direction. The same final orientation is attained at high Re also but it shows an under-damped behavior with overshoots with respect to its final stable orientation.

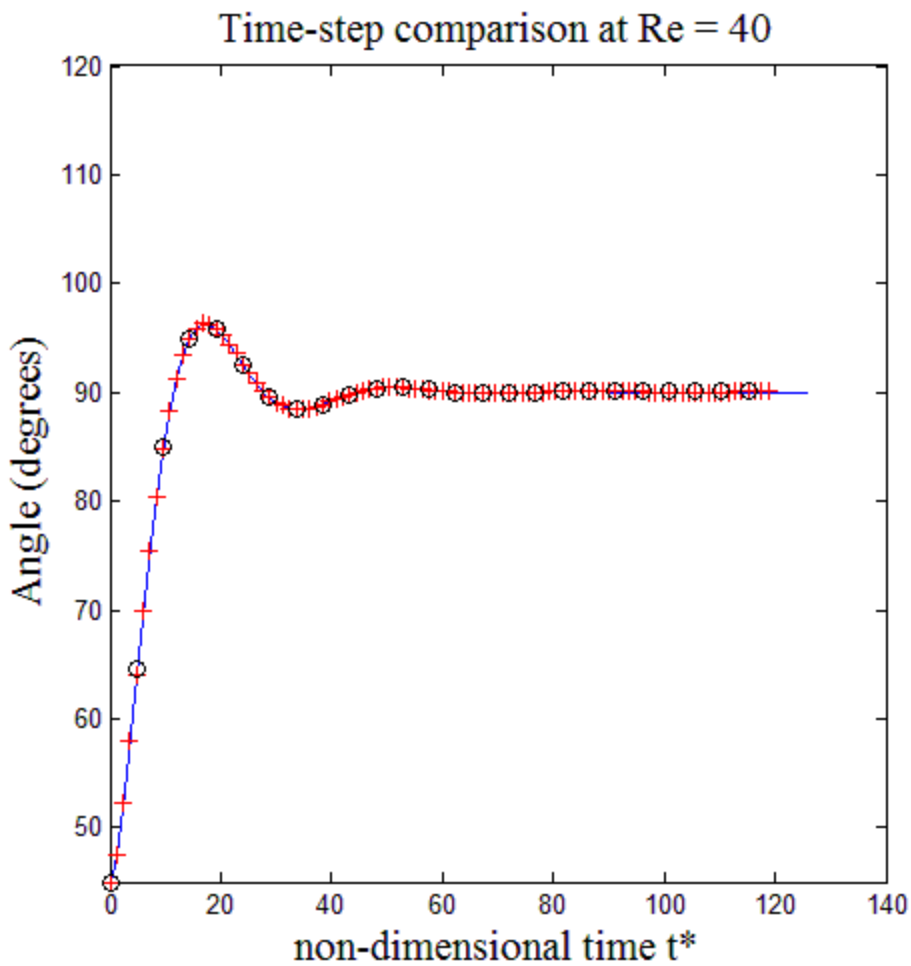

Figure 82: Transient rotation of cylinder at Re = 40

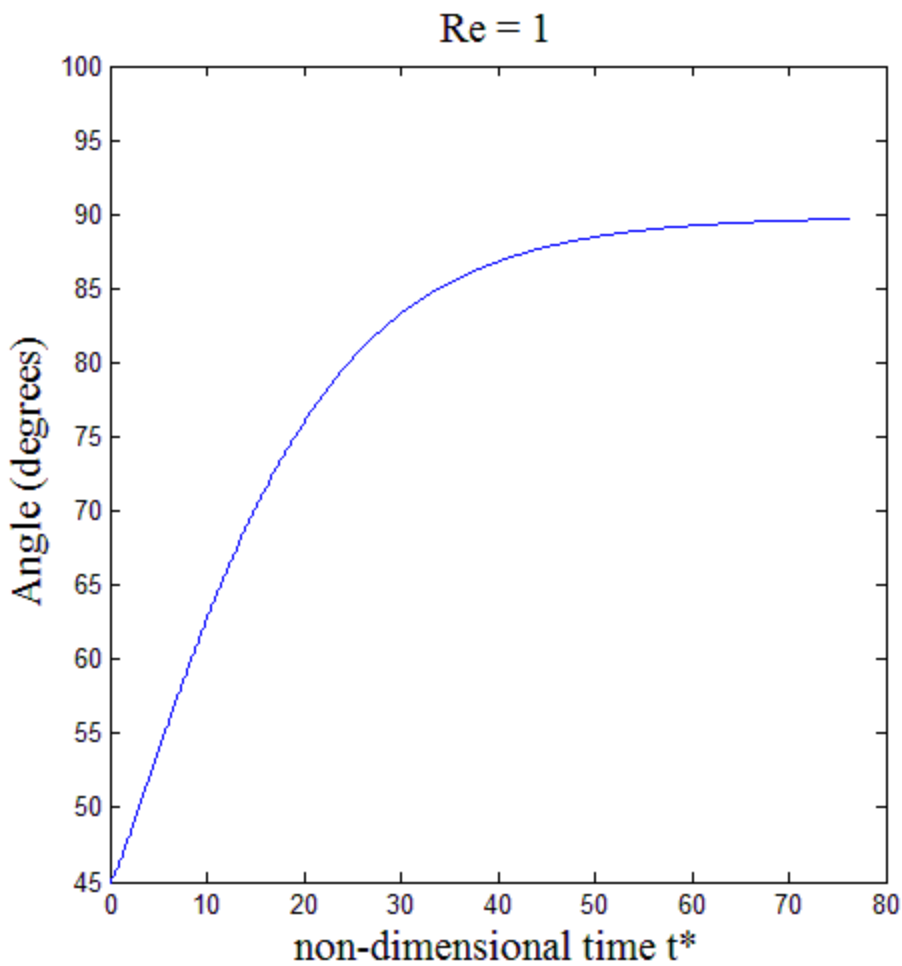

Figure 83: Rotation of a cylinder at Re = 1

Some steady-state simulations were carried out to determine the moment acting on a cylinder of *AR* = 5 at *Re* = 1 and *Re* = 40 and at different angles of the cylinder axis to the freestream vector. Figure 84 shows the distribution over the angular range. The abscissa denotes angular deviations from the equilibrium position of 90 degrees to the freestream vector

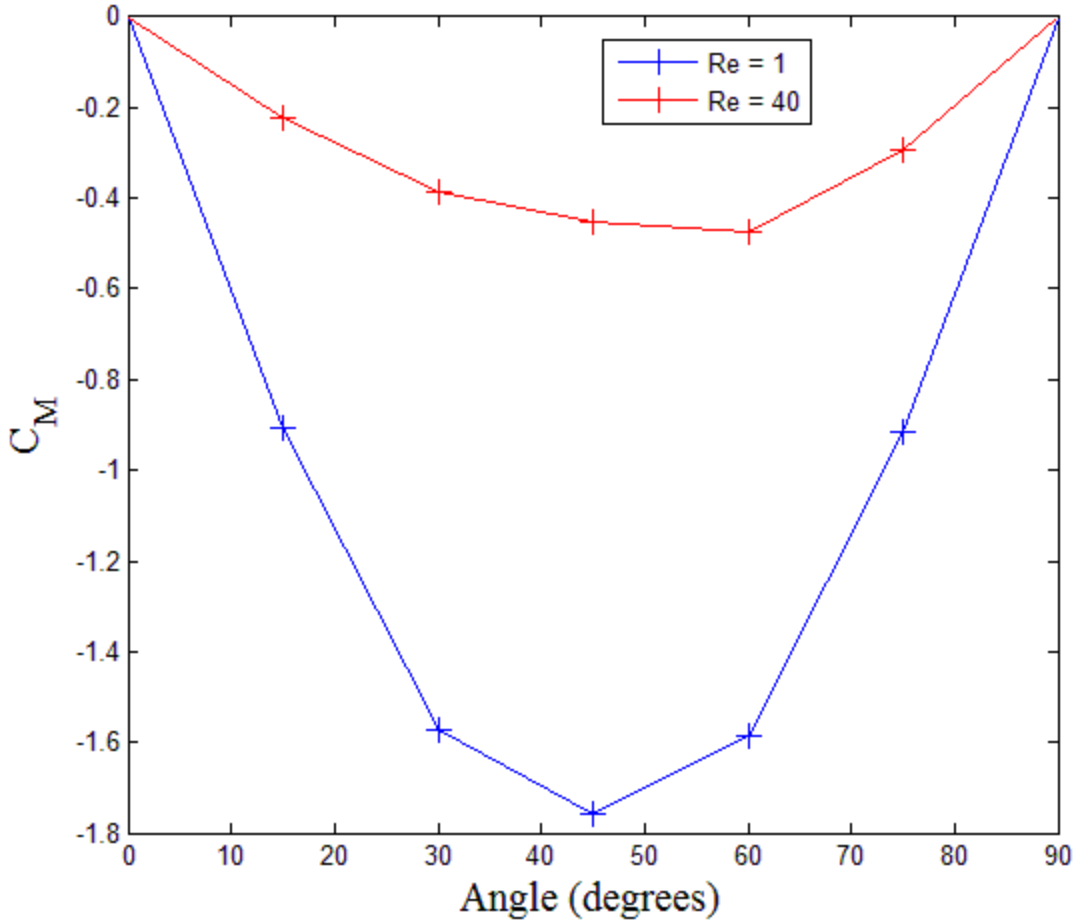

Figure 84: Moment coefficient at different angles to freestream of cylinder with AR = 5 in steady-state

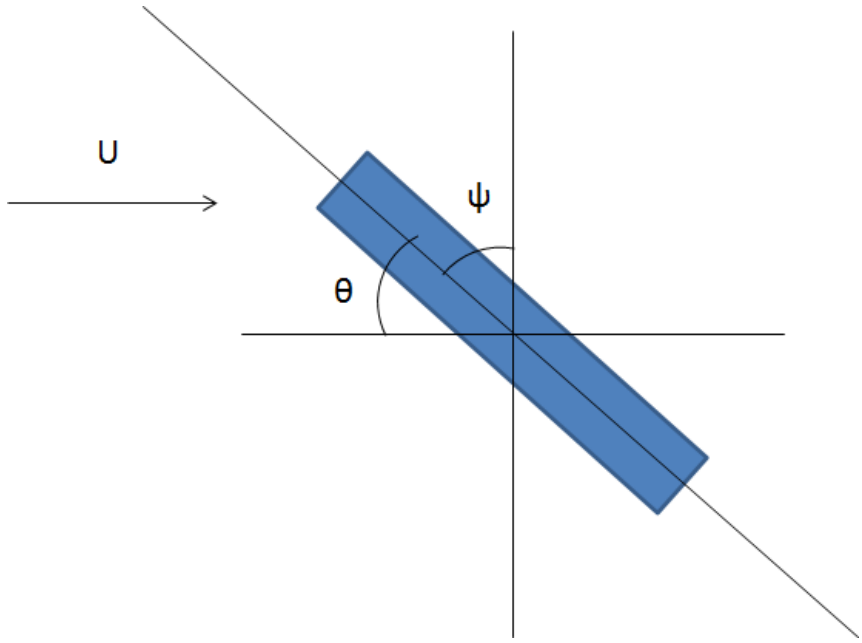

Figure 85: Inclined cylinder

From the above figure, equilibrium position is given by $\theta = \pi/2$ or $\psi = 0$. Curve-fits were obtained for a part of the above distribution. For ψ less than π/4 radians (45 degrees),

$C_M = 2.313\psi^3 - 0.02819\psi^2 - 3.645\psi$ at $Re = 1$ and,

$C_M = 0.7533\psi^3 + 0.2543\psi^2 - 1.242\psi$ at $Re = 40$. Hence,

$\frac{dC_M}{d\psi} = 2.2599\psi^2 + 0.5086\psi - 1.242$ at Re =40 and at $\psi = 0$, $\frac{dC_M}{d\psi} = -1.242$. Hence for small angular deviations from the equilibrium position of $\psi = 0$, $C_M = -1.242\psi$. Also,

Moment $\tau = 0.5\rho U^2 L D^2 C_M = 0.5\rho U^2 (AR) D^3 C_M = -0.621\rho U^2 (AR) D^3 \psi$. The fluid used for simulations had properties $\rho = 1$ kg m^{-3} and $\mu = 1$ kg m^{-1} s^{-1}. $D = 1$ m, $AR = 5$ and $U = 40$ m s^{-1} and hence,

$\tau = -4968\psi$ and moment of inertia $I = (\pi/192)\rho AR(3+4AR^2)D^5 = 8.4267$ kg m^2. Hence natural angular frequency $\omega_0 = (4968/8.4267)^{1/2} = 24.3$ s^{-1}. A curve-fit resembling a damped harmonic oscillator was obtained for the $Re = 40$ case and compared in Figure 86.

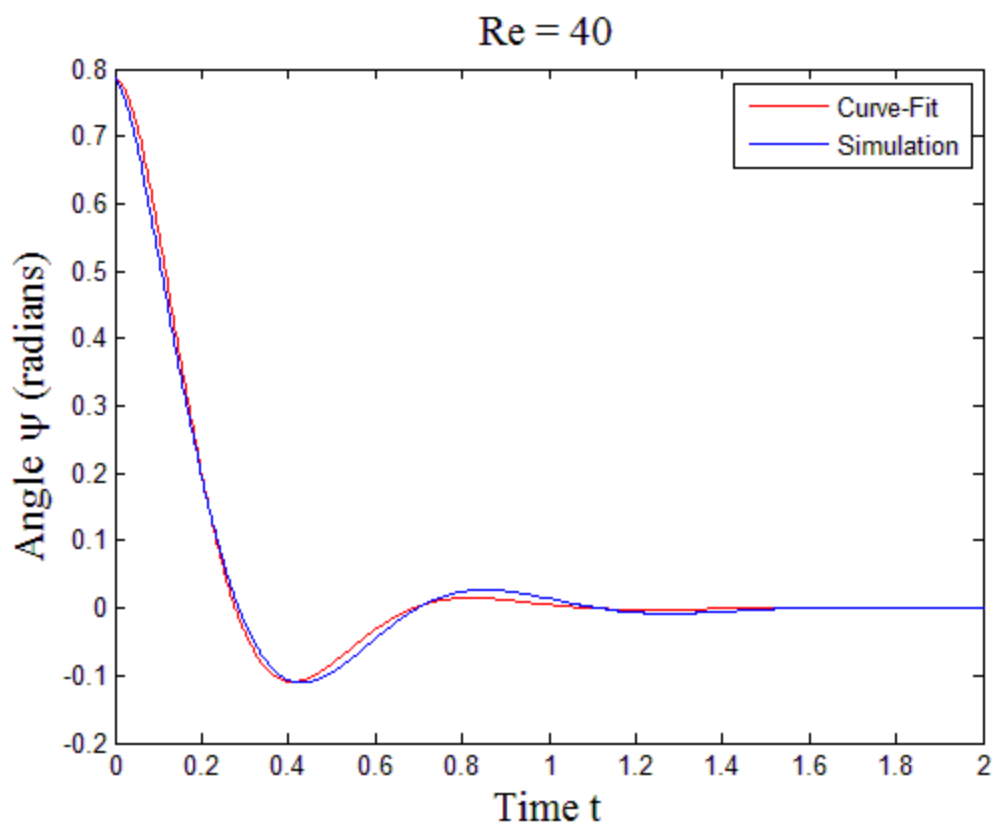

Figure 86: Single cylinder at 45 degrees to freestream and Re = 40 compared with damped harmonic oscillations

The equation of the curve-fit is given by,

$\psi_{curve-fit}(t) = 0.9277e^{-4.8188t}\sin(7.6657t + 1.0096)$. From the curve fit equation, the natural angular frequency ω_0 and damping ratio ς are given as,

ω_0 (fit) = 9.0545 s^{-1} and ς (fit) = 0.5322. The difference between the values of natural angular frequencies in unsteady simulation and that obtained from an analysis of steady state moments may be attributed to the fact that the moment curve-fits were obtained by taking moment coefficient values at angular positions equidistant by π/12 radians (15 degrees) in the range $0<\psi<\pi/2$ and hence the curve-fit may not be very accurate near the equilibrium. Also, if the inaccuracy in the curve-fit is ignored, it must be noted that the cylinder rotates through an angular region in which the dependence of steady-state moment (τ) on the angular position (ψ) is not linear.

For the case of *Re* = 1, in which the transient response shows over-damped behavior, a curve-fit was obtained. Figure 87 shows the comparison between the solution and the curve-fit.

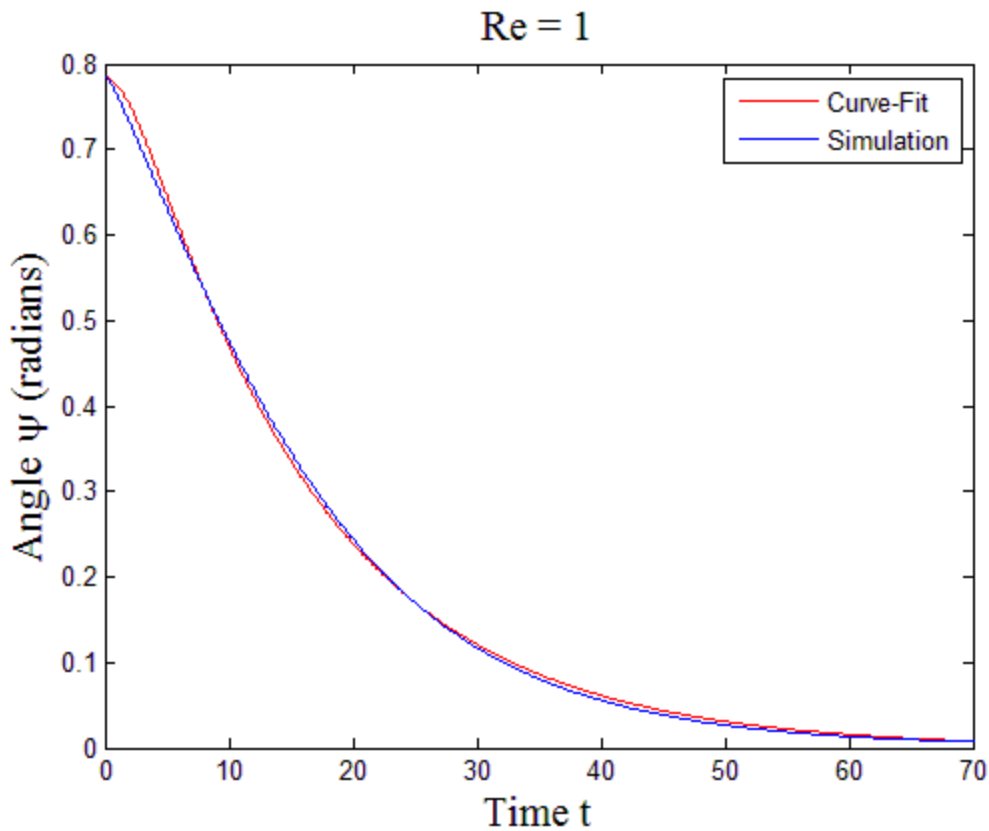

Figure 87: Single cylinder at 45 degrees to freestream and Re = 1 compared with over-damped response

The curve-fit for the above plot is given by,

$\psi_{curve-fit}(t) = e^{-0.2518t}(0.9304e^{0.1839t} - 0.1450e^{-0.1839t})$. Comparison with the general equation of an over-damped transient response gives the natural angular frequency and damping ratio as,

ω_0 (fit) = 0.172 s^{-1} and ς (fit) = 1.464. Similar steady-state moment analysis as above for Re = 40 gives, ω_0 = 1.0398 s^{-1}. Here also, the discrepancy in the values of natural angular frequency may be attributed to the fact that very few points (and also points which are not very close to the equilibrium point) were used to produce the curve fit for the moment and hence the behavior of the cylinder near equilibrium is not taken into account.

4.4.2 Two cylinders in tandem arrangement with initial angular separations (Θ_d) of 5 and 85 degrees

Here simulations were carried to study how two cylinders in tandem arrangement rotate if their axes are at an initial angular separation when seen from the flow direction. Simulations were

carried out for *Re* = 1 and *Re* = 20 and initial angular differences Θ_d = 5 and Θ_d = 85 degrees. Simulations at the lower *Re* take enormous amounts of time and so they were discontinued before they reached steady-state. The low *Re* simulation results are in agreement with what was found for the steady-state simulations, that is, the angular separation tends to increase for *Re*<15. At Re = 20 and for both initial angular separations, the cylinders got aligned and ceased to rotate at steady-state. Figure 88 and Figure 89 show how cylinders rotate at *Re* = 1 and Figure 90 and Figure 91 show how the cylinders rotate at *Re* = 20.

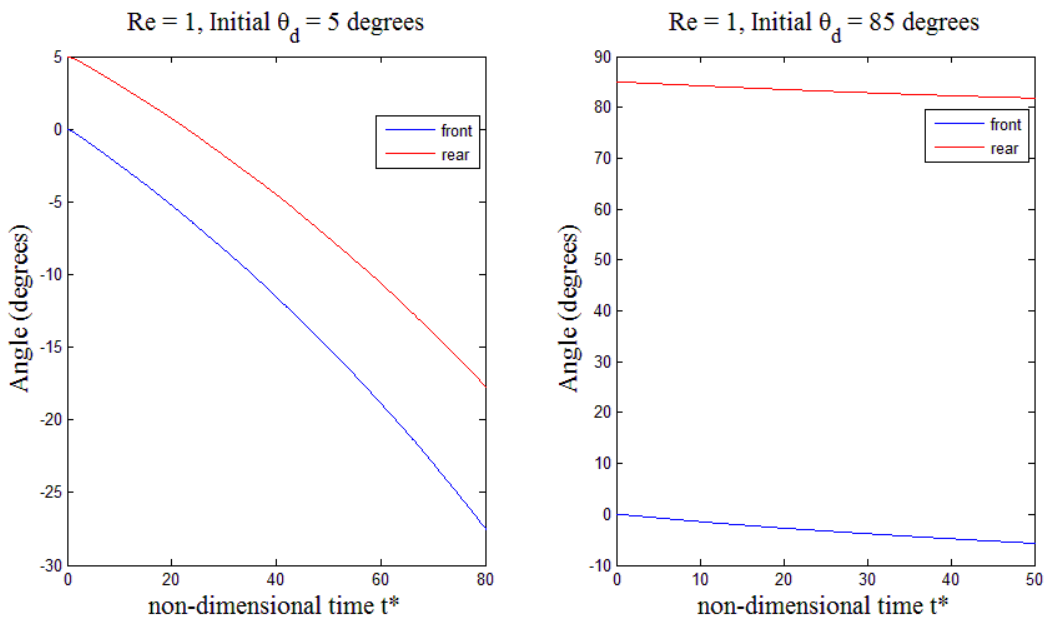

Figure 88: Rotation of front and rear cylinders in planes normal to flow direction at Re = 1 for initial angular separations of 5 and 85 degrees

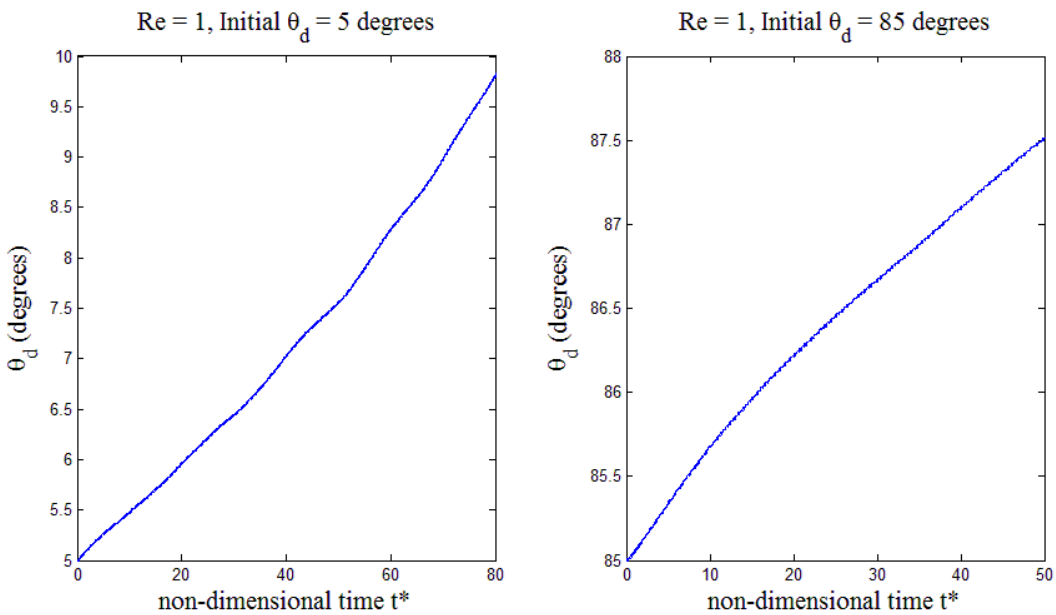

Figure 89: Angular separation between axes of front and rear cylinders at Re = 1 for initial angular separations of 5 and 85 degrees

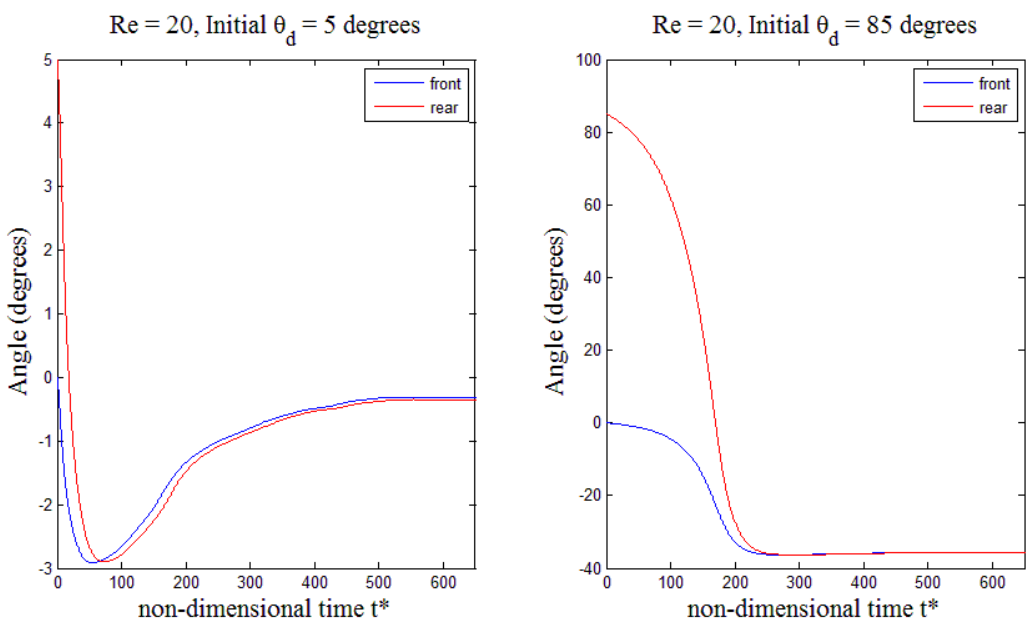

Figure 90: Rotation of front and rear cylinders in planes normal to flow direction at Re = 20 for initial angular separations of 5 and 85 degrees

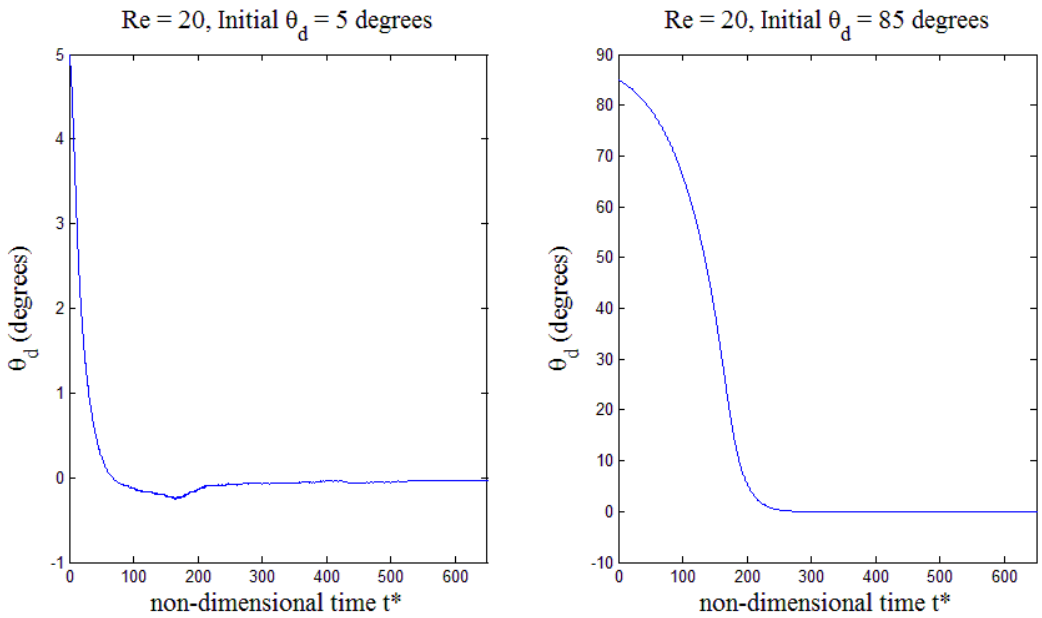

Figure 91: Angular separation between axes of front and rear cylinders at Re = 20 for initial angular separations of 5 and 85 degrees

Chapter 5 – Conclusion and recommendations for future work

1. From the two-dimensional simulations, it may be said that collapse of fibers does not significantly change their dynamics as the maximum percentage difference in drag coefficient of the front cylinder for different ellipticities is 6.4% which happens at Re = 50 and SeR = 1. The rear cylinder has a maximum percentage difference of 2.62% in drag coefficient for different ellipticities at Re = 20 and SeR = 1. Smaller the separation between the cylinders, the greater is the difference between the drag coefficients between the front and rear cylinders. Hence in high concentration pulp suspensions, as expected, there is greater likelihood of fiber-fiber collision leading to entanglement. The collision probability increases with increasing Re.

2. Pulp suspensions with different distributions of fiber-lengths are expected to show different extents of fiber-fiber entanglement and flocculation. Moment difference between non-parallel fibers in proximity may bring the fibers in alignment or cause them to rotate further to increase angular separation between them. The difference in the moments is greatest at around 45 degrees angular separation. The drag for the rear cylinder for parallel cylinders is much lower than that of the front cylinder but in many applications, where flow field varies considerably in speed and direction, it is quite likely that fibers once in close proximity and parallel, may lose their relative parallel alignment and hence the eclipsed cylinder may experience greater drag and moment leading to fluctuations in the rate in which the separation between fibers decreases.

3. It was observed that for Re<15 when the cylinders were very close, the tendency was towards attaining non-parallel orientations. Speaking of parallel and non-parallel orientations for pulp fibers in proximity, it may be said that entanglement is more likely for the latter. But again, the higher the aspect ratio of the fibers the less important may be the rotation of fibers. Simulation of two-cylinder rotation at small separation at higher Re may require a finer mesh and additional care about the time-step. This is so because as the Re is increased, since the cylinders are very close ($\sim D$), the effective Reynolds number may be near double of the value computed with a single cylinder diameter and this may lead to some unsteadiness in the solution. Also, it is believed that the mesh elements around the

cylinders should be uniform, a structured boundary-layer meshing being an apt choice. The use of mesh-interfaces makes the requirement of fine-meshing even more serious.

4. From the results of the unsteady simulations it was noticed that at both Re = 1 and Re = 40, the cylinder tends to attain an alignment in which its axis is perpendicular to the freestream. At low Re, the two cylinders in a tandem arrangement and initially parallel, tend to attain non-parallel alignments but the trend is reversed at higher Re. This again suggests that at low Re, the flow is much more complex as parallel alignment of cylinders, there is a greater possibility of flocculation and entanglement but a non-parallel alignment leads to increasing the drag on the rear cylinder thereby reducing the chance of entanglement.

Recommendations for future work:

1. Hydrodynamic interaction between parallel cylinders of different aspect ratios and more general alignment may be a next step to this research. Though extensive literature exists for cylinders in side-by-side arrangements, some research may be carried out for cases in which the line joining the fiber-centers make an angle in the range of 0 – 90 degrees with the freestream. This may be interesting because in these cases the drag for both the cylinders will begin to become equal with increasing angle with free stream.

2. The above study may be continued for non-parallel cylinders and hydrodynamic moments may be determined for different positions of the cylinder centres.

3. In real cases, fibers are highly flexible and they often move in bent shapes. Hence hydrodynamic interaction between C-shaped fibers in tandem arrangements may also be studied in similar and non-similar orientations in the flow.

Bibliography

[1] S. Yamamoto and T. Matsuoka, "Dynamic simulation of fiber suspensions in shear flow," *Journal of Chemical Physics,* vol. 102, no. 5, pp. 2254-2260, 1995.

[2] R. G. Cox, "The motion of long slender bodies in a viscous fluid Part 1. General theory," *Journal of Fluid Mechanics,* vol. 44 Part 4, pp. 791-810, 1970.

[3] H. Lamb, Hydrodynamics, New York, USA: Dover Publications, 1932.

[4] J. M. Stockie and S. I. Green, "Simulating the Motion of Flexible Pulp Fibres Using the Immersed Boundary Method," *Journal of Computational Physics,* vol. 147, pp. 147-165, 1998.

[5] L. Zhu and C. S. Peskin, "Drag of a flexible fiber in a 2D moving viscous fluid," *Computers & Fluids,* vol. 36, pp. 398-406, 2007.

[6] D. Qi, "Direct simulations of flexible cylindrical fiber suspensions in finite Reynolds number flows," *The Journal of Chemical Physics,* vol. 125, p. 114901, 2006.

[7] S. B. Lindstrom and T. Uesaka, "A model for flexible fibres in viscous and inert fluid," *Appita,* pp. 23-28, 2007.

[8] S. B. Lindstrom and T. Uesaka, "Simulation of the motion of flexible fibers in viscous fluid flow," *Physics of Fluids,* vol. 19, p. 113307, 2007.

[9] M. M. Zdravkovich, Flow around circular cylinders Vol 1: Fundamentals, Oxford Science Publications, 1997.

[10] B. Fornberg, "A numerical study of steady viscous flow past a circular cylinder," *Journal of Fluid Mechanics,* vol. 98, no. 4, pp. 819-855, 1980.

[11] S. Sen, S. Mittal and G. Biswas, "Steady separated flow past a circular cylinder at low Reynolds numbers," *Journal of Fluid Mechanics,* vol. 620, pp. 89-119, 2009.

[12] S. C. R. Dennis and P. J. S. Young, "Steady flow past an elliptic cylinder inclined to the

stream," *Journal of Engineering Mathematics,* vol. 47, pp. 101-120, 2003.

[13] S. A. Johnson, M. C. Thompson and K. Hourigan, "Flow past elliptical cylinders at low Reynolds numbers," in *14th Australasian Fluid Mechanics Conference*, Adelaide, Australia, 2001.

[14] M. Sugihara-Seki, "The motion of an elliptical cylinder in channel flow," *Journal of Fluid Mechanics,* vol. 257, pp. 575-596, 1993.

[15] I. Imai, "A new method of solving Oseen's equations and its application to the flow past an inclined elliptic cylinder," *Proceedings of the Royal Society A,* vol. 224, pp. 141-160, 1954.

[16] S. Tomotika and T. Aoi, "An expansion formula for the drag on a circular cylinder moving through a viscous fluid at small Reynolds numbers," *Quaterly Journal of Mechanics and Applied Mathematics,* Vols. IV, part 4, pp. 401-406, 1951.

[17] S. Tomotika and T. Aoi, "The steady flow of a viscous fluid past an elliptic cylinder and a flat plate at small Reynolds numbers," *Quaterly Journal of Mechanics and Applied Mathematics,* vol. VI, pp. 290-312, 1953.

[18] S. Taneda, "Experimental Investigation of the wakes behind cylinders and plates at low Reynolds number flows," *Journal of the Physical Society of Japan,* vol. 11, no. 3, pp. 302-307, 1956.

[19] S. Taneda, "Visualization of separating Stokes flows," *Journal of the Physical Society of Japan,* vol. 46, no. 6, pp. 1935-1942, 1979.

[20] R. E. Khayat and R. G. Cox, "Inertia effects on the motion of long slender bodies," *Journal of Fluid Mechanics,* vol. 209, pp. 435-462, 1989.

[21] M. M. Zdravkovich, "The effects of interference between circular cylinders in cross flow," *Journal of Fluids and Structures,* vol. 1, pp. 239-261, 1987.

[22] A. Vakil and S. I. Green, "Two-dimensional side-by-side circular cylinders at moderate Reynolds numbers," *Computers & Fluids,* vol. 51, pp. 136-144, 2011.

[23] P. W. Bearman and A. J. Wadcock, "The interaction between a pair of circular cylinders normal to a stream," *Journal of Fluid Mechanics,* Vols. 61, part 3, pp. 499-511, 1973.

[24] K. Lee and K.-S. Yang, "Flow patterns past two cylinders in proximity," *Computers & Fluids,* vol. 38, pp. 778-788, 2009.

[25] J. R. Meneghini, F. Saltara, C. L. R. Siqueira and J. A. Ferrari Jr, "Numerical simulation of flow interference between two circular cylinders in tandem and side-by-side arrangements," *Journal of Fluids and Structures,* vol. 15, pp. 327-350, 2001.

[26] H. Yuan and A. Prosperetti, "On the in-line motion of two spherical bubbles in a viscous fluid," *Journal of Fluid Mechanics,* vol. 278, pp. 325-349, 1994.

[27] M. M. Zdravkovich and D. L. Pridden, "Interference between two circular cylinders; Series of unexpected discontinuities," *Journal of Industrial Aerodynamics,* vol. 2, pp. 255-270, 1977.

[28] E. Norman and J. H. Masliyah, "Creeping flow through clusters of spheroids and elliptical cylinders," *The Chemical Engineering Journal,* vol. 3, pp. 169-175, 1972.

[29] D. Castiglia, S. Balabani, G. Papadakis and M. Yianneskis, "An experimental and numerical study of the flow past elliptical cylinder arrays," *Proceedings of the Institution of Mechanical Engineers, Part C: Journal of Mechanical Engineering Science,* vol. 215, pp. 1287-13001, 2001.

[30] A. Vakil and S. I. Green, "Drag and lift coefficients of inclined finite circular cylinders at moderate Reynolds numbers," *Computers & Fluids,* vol. 38, pp. 1771-1781, 2009.

[31] G. B. Jeffery, "The motion of ellipsoidal particles immersed in a viscous fluid," *Royal Society Publishing,* vol. 102, no. 715, pp. 161-179, 1922.

[32] S. C. R. Dennis and G.-Z. Chang, "Numerical solutions for steady flow past a circular cylinder at Reynolds numbers up to 100," *Journal of Fluid Mechanics,* vol. 42, pp. 471-489, 1970.

[33] C. A. Stover and C. Cohen, "The motion of rodlike particles in the pressure-driven flow between two flat-plates," *Rheologica Acta,* vol. 29, pp. 192-203, 1990.

[34] E. Wacholder and N. F. Sather, "The hydrodynamic interaction of two unequal spheres moving under gravity through quiescent viscous fluid," *Journal of Fluid mechanics,* Vols. 65, part 3, pp. 417-437, 1974.